UC Santa Cruz
UC Santa Cruz Electronic Theses and Dissertations

Title

Effects Of Near-Source Heterogeneity On Wave Fields Emanating From Crustal Sources Observed At Regional And Teleseismic Distances

Permalink

https://escholarship.org/uc/item/1694v6gj

Author

Avants, Megan

Publication Date

2014

Peer reviewed|Thesis/dissertation

eScholarship.org
Powered by the California Digital Library
University of California

UNIVERSITY OF CALIFORNIA
SANTA CRUZ

EFFECTS OF NEAR-SOURCE HETEROGENEITY ON WAVE FIELDS EMANATING FROM CRUSTAL SOURCES OBSERVED AT REGIONAL AND TELESEISMIC DISTANCES

A dissertation submitted in partial satisfaction
of the requirements of the degree of

DOCTOR OF PHILOSOPHY

in

EARTH SCIENCES
with an emphasis in GEOPHYSICS

by

Megan S. Avants

March 2014

The Dissertation of Megan S. Avants is approved:

Professor Thorne Lay, Chair

Professor Susan Schwartz

Professor Emily Brodsky

Tyrus Miller
Vice Provost and Dean of Graduate Studies

Copyright © by

Megan S. Avants

2014

Table of Contents **Page**

List of Figures vi

Abstract x

Dedication xii

Acknowledgments xiii

1. Effects of 2D random velocity heterogeneities in the mantle lid and Moho topography on P_n geometric spreading **1**

1.1 Abstract 1

1.2 Introduction 2

1.3 Methods 6

1.4 P_n Sensitivity to Radial Mantle Lid Velocity Gradients 9

1.5 P_n Sensitivity to Mantle P-Velocity Heterogeneity 13

1.6 P_n Sensitivity to Moho Topography 25

1.7 Discussion and Conclusions 30

1.8 Data and Resources 38

1.9 Acknowledgments 38

1.10 References 40

2. Calculating 3D teleseismic P-wave Green's functions: Capturing near-source 3D waveform complexity in synthetic teleseismic P-waves **42**

2.1 Abstract 42

2.2 Introduction 43

2.3 Theory 46

2.4 Implementation 51

2.5 Testing and Benchmarks 55

2.6 Conclusion 59

2.7 References 62

3. Using 3D teleseismic *P*-wave Green's functions to determine source characteristics of North Korean nuclear test explosions 65

3.1 Abstract 65

3.2 Introduction 65

3.3 Methods 70

3.4 Results 77

3.5 Discussion and Conclusions 80

3.6 References 87

4. Rupture model of the 2008 Wenchuan earthquake using 3D Green functions 88

4.1 Abstract 88

4.2 Introduction 88

4.3 Methods 94

4.4 Results 100

4.5 Discussion and Conclusions 101

4.6 References 109

Appendices

Appendix A: Synthetic PGFs for the 2006, 2009, and 2013 source grid regions **112**

References **123**

List of Figures **Page**

1.1 P_n path, crustal and mantle seismic velocity and density values **7**

1.2 P_n amplitude versus distance curves for various frequencies **11**

1.3 2D finite difference calculations of P_n amplitude versus distance for different mantle lid gradients **12**

1.4 Sample velocity models with random *P*-wave velocity heterogeneity and Moho depth fluctuations **14**

1.5 P_n amplitude versus distance for five realizations of random mantle lid *P*-wave velocity fluctuations, compared to the average amplitude and that predicted for a homogeneous Earth **17**

1.6 Ensemble-averaged P_n amplitudes as a function of distance for all configurations of random volumetric mantle heterogeneity simulated **19**

1.7 Synthetic P_n seismograms generated for representative volumetric mantle heterogeneity finite difference calculations **21**

1.8 Ensemble-averaged P_n amplitudes as a function of distance for all configurations of random volumetric mantle heterogeneity, grouped by percent rms fluctuation and windowing method **24**

1.9 Ensemble-averaged P_n amplitudes versus distance for all configurations of random Moho topographic heterogeneity **29**

1.10 Ensemble-averaged P_n amplitudes versus distance for all configurations of Moho topographic heterogeneity, grouped by percent rms fluctuation and windowing method **32**

1.11 Synthetic P_n seismograms generated from representative Moho depth variation calculations **34**

2.1 Schematic of the generation of 3DGFs, and the 1D teleseismic path outside of the near-source domain **47**

2.2 Snapshot of each of the 6 component time series used in the representation theorem, showing expansion of the wavefronts across the collection plane in time **56**

2.3 Radiation patterns for single-force and force-couple point sources **57**

2.4 PGFs calculated for an isotropic source to a ring of theoretical teleseismic stations at 30-degree azimuthal increments, showing consistency of timing and amplitude with azimuth **60**

2.5 Sample comparison of a 3DGF and 1DGF **61**

3.1 Google Earth image of North Korea nuclear test site with source locations and grid search locations **69**

3.2 Stacked traces from arrays recording the 10/09/2006 event **73**

3.3 Stacked traces from arrays recording the 05/25/2009 event **74**

3.4 Stacked traces from arrays recording the 02/12/2013 event **75**

3.5 Correlation between *a/b* amplitude ratios of PGFs at different source grid locations with observed *a/b* amplitude ratios for the 10/09/2006 event **78**

3.6 Correlation between *a/b* amplitude ratios of PGFs at different source grid locations with observed *a/b* amplitude ratios for the 05/25/2009 event **79**

3.7 Correlation between *a/b* amplitude ratios of PGFs at different source grid locations with observed *a/b* amplitude ratios for the 02/12/2013 event **80**

3.8 Mapped correlation results across the source grids for the 2006 and 2009 events **83**

3.9 Mapped correlation results across the source grids for the 2006 and 2013 events **84**

4.1 Regional map of the Longmen Shan thrust belt and local map with aftershock focal mechanisms **90**

4.2 Google Earth image with surface traces of Wenchuan-Maowen, Beichuan, and Pengguan faults, as well as the simplified, segmented model fault used in this study **95**

4.3 Map of earthquake region, with topography from the same topographic model used in the calculation of 3DGFs **97**

4.4 Similarities and differences between 1DGFs and 3DGFs calculated to one teleseismic station **99**

4.5 Rupture models obtained from 3DGFs and 1DGFs **100**

4.6 Waveforms from 3DGFs, compared to observed waveforms **102**

4.7 Waveforms from 1DGFs, compared to observed waveforms **103**

4.8 Results of comparable fault models **106**

List of Tables **Page**

3.1 DPRK source grid locations **68**

3.2 Average array locations **72**

Abstract

Effects of near-source heterogeneity on wave fields emanating from crustal sources observed at regional and teleseismic distances

by

Megan S. Avants

Near-source path effects imprint the wave field emanating from a seismic source and, if not well resolved, can obscure the details of source characteristics determined from observations of the seismic waves at regional and teleseismic distances ($\geq$200 km). These effects are particularly strong for crustal sources such as shallow earthquakes and underground nuclear explosions. First, I explore 2D effects of random seismic *P*-wave velocity heterogeneity resulting from volumetric heterogeneity in the upper mantle and variability of the Moho on the amplitude decay of the regional phase P_n. Results indicate that the pattern of amplitude decay due to geometric spreading for a simple Earth model is more complex than that for an Earth model containing strong heterogeneity in the mantle lid. Next, I implement the representation theorem in a method which collects displacement and strain components output from a 3D finite difference program capable of including realistic surface topography and geologic structure in a 3D velocity model, and calculates teleseismic 3D Green functions (3DGFs) to specified receiver locations. Green functions produced from a 3D source model match Green functions produced from a

1D source model for theoretical source-receiver geometries. This new method is then applied to the problem of constraining the source depth and location of the three nuclear tests conducted by North Korea, by using a realistic topography model for the mountainous test region to calculate 3DGFs for several possible locations of each event. Amplitude ratios of *P* and *pP* from 3DGFs are correlated to those in observed stacked traces. Results show a sensitivity of this method to source depth and location across the test site region with source depths slightly greater than published estimates, but relative locations consistent with other studies. Finally, I determine a rupture model of the 2008 Wenchuan earthquake using 3DGFs calculated in a velocity model containing the dramatic topographic contrast in the fault area, and compare results with a rupture model produced using 1DGFs. Rupture models derived from 1D and 3D synthetic source regions are very similar to each other, and both are consistent with other studies.

Dedication

This work is dedicated to the many people who supported me, both professionally and personally, throughout my time at UCSC. Thanks to the friends I have made over the years. I have many fun, funny, delicious, musical, sun-filled memories that I hope to continue making with you. I have made many friends for life here. I would like to also thank my family, most notably my mother, who was instrumental in making sure my refrigerator was stocked over the last 6 months, but who was always a tireless cheerleader. Finally, to my advisor, Thorne Lay, and the rest of my committee, Susan Schwartz and Emily Brodsky, thank you. Your patience and advice gave me access to career options that would not have been available to me otherwise. Your support and that of my personal network, helped me overcome many obstacles in the course of my Ph.D. work, and I am so thankful and humbled upon reaching this milestone.

Acknowledgement

Chapter 1 of this thesis includes a reprint of the following published material:

Avants, M., T. Lay, X-B. Xie, and X. Yang (2011). Effects of 2D random velocity heterogeneities in the mantle lid and Moho topography on P_n geometric spreading, *Bull. Seismol. Soc. Am.* **101**, 126-140, doi 10.1785/0120100113.

T. Lay and X-B. Xie directed and supervised the research that forms the basis for this chapter. X. Yang performed the calculations for the velocity gradient in the mantle lid.

Chapter 1

Effects of 2D random velocity heterogenities in the mantle lid and Moho topography on P_n geometric spreading

Megan Avants[1], Thorne Lay[1], Xiao-Bi Xie[2], and Xiaoning Yang[3]

[1]Department of Earth and Planetary Sciences, University of California Santa Cruz
[2]Institute of Geophysics and Planetary Physics, University of California Santa Cruz
[3]Geophysics Group, Earth and Environmental Sciences Division, Los Alamos National Laboratory

1.1 Abstract

P_n-wave energy refracts through the uppermost mantle, producing the first seismic wave arrival at distances of ~200 to ~1500 km from crustal sources. The P_n phase provides important constraints on source type, location, and magnitude, but its propagation is complicated by frequency-dependent sensitivity to the Earth's sphericity and lithospheric velocity structure. Converging on an acceptable P_n geometric spreading correction and specifying its uncertainties, a requirement for accurately determining frequency-dependent attenuation models for P_n, depends on improved understanding of the behavior of P_n geometric spreading for various heterogeneous models. We investigate the effects of radial mantle lid velocity gradients, mantle lid random volumetric velocity heterogeneities, and Moho topography on P_n geometric spreading using reflectivity and two-dimensional (2D) finite-difference 1-Hz wave propagation calculations for elastic Earth models. Mantle lid velocity gradients systematically modify the frequency-dependent geometric spreading from that found for models with constant velocity but retain the same overall functional form. P_n amplitudes are also sensitive to the presence of modest 2D random lateral velocity heterogeneities within the uppermost mantle, with geometric spreading approaching a power-law behavior as the root mean square strength

of heterogeneity increases. Two-dimensional Moho topography introduces scatter into the amplitude of P_n, but the overall behavior remains compatible with that for a laterally homogeneous model. Given the lack of knowledge of specific small-scale structure for any particular P_n path, the preferred geometric spreading parameterization is the frequency-dependent model for a constant mantle lid velocty structure unless P_n travel-time branch curvature can constrain the radial gradient in the mantle lid.

1.2 Introduction

Distinguishing small earthquakes from low-yield underground nuclear explosions (given a typical dearth of teleseismic oservations) requires that regionally detected seismic phases (P_n,S_n,P_g,L_g) be understood in detail. Several source discrimination techniques have been developed that measure the relative amount of *P/S* energy in regional signals (e.g., Walter *et al.*, 1995; Hartse *et al.*, 1997), with regional travel-time tomography and attenuation models being used to suppress the effects of wave propagation in the heterogeneous crust. The contribution of geometric spreading to the regional seismic signals must also be quantified and accounted for, particularly for use in developing attenuation models. Geometric spreading can be very difficult to distinguish from anelastic attenuation, especially for P_n and S_n phases, which are known to have frequency-dependent sensitivity to the Earth's sphericity, upper-mantle velocity heterogeneity, and lower-crustal structure (Buldyrev and Lanin, 1965; Hill, 1973; Sereno and Given, 1990; Taylor *et al.*, 2002). Morozov (2010) gives a detailed discussion on the definition of geometric spreading, in which he explains that geometric spreading can be defined as amplitude decay due to the expansion of a single wavefront, or that geometric spreading can be considered in such a way as to include the elastic effects of the Earth's structure on amplitude decay. The single-wavefront definition requires that any amplitude variations from this simple model be attributed to scattering attenuation. On the other hand, the fully inclusive definition of geometric spreading would consider "scattering attenuation" merely as geometric spreading in a heterogeneous Earth. Our modeling efforts assume the latter definition of geometric spreading and seek to characterize the contribution of scattering to observed P_n amplitudes in a purely elastic medium. Yang *et al.* (2007) developed frequency-dependent geometric spreading relations for P_n and S_n for simple reference velocity structures with constant velocities in the uppermost mantle lid (the high-velocity layer underlyng the Moho and above any upper-mantle low-velocity zone) that differ significantly from commonly used frequency-independent power-law geometric spreading corrections (e.g., Walter and Taylor, 2001).

P_n and S_n are generated by crustal sources and have paths that refract through the uppermost mantle with some secondary energy multiply reflecting from the underside of the Moho discontinuity as long as the radial velocity gradient is above the critical negative gradient (e.g., Yang *et al.*, 2007). The distances at which P_n and S_n are observed as first *P*-wave and *S*-wave arrivals ranges fom their crossover with P_g and L_g near 200 km to where *P*-wave and *S*-wave energy that has dived down to the vicinity of the transition zone overtakes them near 1500 km. The direct ray paths for P_n and S_n as far out as 1500 km distance bottom in the upper 50 km of the mantle lid for typical seismic velocity models, and the multiple underside Moho reflections bottom even shallower in the mantle lid. These shallow trajectories make P_n and S_n phases particularly sensitive to Earth's sphericity and to details of the velocity structure of the lower crust and upper mantle through which they propagate nearly horizontally. Theoretical calculations of P_n propagation through a spherical body (Buldyrev and Lanin, 1965; Hill, 1973), as well as one-dimensional (1D) reflectivity simulations of P_n propagation (Yang *et al.*, 2007) through laterally homogeneous layered models, provide ample documentation of P_n sensitivity to the Earth's sphericity.

An analysis of variance (ANOVA) study conducted by Fisk *et al.* (2008) shows that P_n amplitude observations have the highest total path variance of the regional phases (P_n,S_n,P_g,L_g) typically used for regional source discriminants. This reflects the pronounced sensitivity of P_n to heterogeneous lithospheric structure and the fact that the P_n phase is not comprised of a suite of arrivals sampling a wide range of ray parameters that intrinsicaly average out the path effects, as is the case for the other phases (particularly P_g and L_g). The basic wave propagation characteristics of S_n are similar to those for P_n, but the additional *P*-to-*S* conversions in the high frequency S_n signals appear to somewhat stabilize rms amplitude measures relative to those for P_n, so we will focus on P_n in this study.

Geometric spreading corrections are typically defined for simple reference Earth models, motivated by seismic waveform modeling procedures; while it is clear that a 1D seismic model is not precisely correct for any path, our lack of knowledge of the actual 3D structure justifies using a simplified reference model about which there is expected to be a normally distributed variation of observations. For many phases this is reasonable; teleseismic body waves with turning points in the relatively homogeneous lower mantle appear to have minor scatter relative to 1D frequency-independent geometric spreading assumptions, while the behavior of complex multiple arrivals like L_g at regional distances can largely be accounted for by simple frequency-independent power-law amplitude decays by virtue of their intrinsic strong wave interference (e.g., Yang, 2002). In this regard, P_n and S_n are important exceptions; even for a very simple spherical reference model involving a constant-velocity crustal layer over a constant-velocity upper-mantle layer, the computed geometric spreading is frequency-dependent, nonuniform with distance, and nonlinearly sensitive to perturbations of the structure (Yang *et al.*, 2007). While observed P_n amplitude decay with distance may be well characterized by a simple power-law function, separating geometric spreading from attenuation effects that control the amplitude decay is very difficult when one cannot justify assuming a frequency-independent geometric spreading correction. Ignoring the frequency dependence of geometric spreading will inject artificial frequency dependence directly into attenuation estimates, undermining the latter's use for path corrections or geophysical interpretations.

These considerations motivate using as realistic of a P_n geometric spreading relation as possible; however, the very sensitivity of P_n to spherical structure which produces complexity in the geometric spreading is also likely to yield sensitivity to small structural perturbations, with non-self-evident behavior. Full waveform calculations are made here to evaluate the sensitivity of P_n geometric spreading to deviations from a very simple reference model. We consider 1D gradients in the mantle lid velocity structure, 2D lateral volumetric heterogeneities in the mantle lid structure, and 2D topographic heterogeneity of the Moho, with the goals of assessing what practical choice of P_n geometric spreading is most reasonable and assessing the attendant uncertainties. We find that modest, geologically reasonable structural heterogeneity produces strong P_n amplitude variability with distance, which ensures that considerable errors are associated with any P_n geometric-spreading parameterization. These errors will be manifested in, for example, incorrect attenuation models for P_n. Adhering to the seismic modeling paradigm, our pragmatic recommendation is to use the complex frequency-dependent geometric spreading for a very simple basic Earth model (Yang *et al.*, 2007) rather than an arbitrarily parameterized model such as a power-law for which there is no known associated 1D reference structure, allowing for large uncertainties on any derived attenuation model that accompanies it. The geometric spreading approximation for a laterally homogeneous (1D) Earth model from Yang *et al*. (2007) has the advantages of being consistent with theoretically predicted P_n propagation and corresponding to a specific parameterized velocity model. However, it does have multiple parameters, each nonlinearly dependent on changes in the velocity model, which makes applying this approximation slightly more complicated than selecting a single decay coefficient, as is the case for a power-law approximation. We argue the minor added complexity is necessary, as our models show that P_n does indeed have a nonlinear response to changes in mantle velocity gradient or small-scale structure. Empirically constraining the average mantle lid velocity gradient by first-arrival travel-time curvature can significantly improve the choice of reference model, but there will still be significant uncertainties associated with unresolved small-scale heterogeneities in the mantle lid structure.

1.3 Methods

Synthetic calculations in this study employ the 1D reflectivity method (Müller, 1977; Randall, 1994), as implemented by Yang *et al*. (2007), and the 2D *P-SV* finite-difference code of Xie and Lay (1994). We add linear radial mantle lid velocity gradients, randomly varying volumetric mantle lid P-wave velocity (V_p) heterogeneity, or Moho depth heterogeneity to the homogeneous basic Earth model (BEM) from Yang *et al*. (2007) and Sereno and Given (1990). This simple spherical reference model contains a 40-km-thick crust and a constant-velocity mantle (Fig. 1.1a). For both the reflectivity and finite-difference methods, we apply an Earth flattening transform (EFT) (Chapman, 1973) to the BEM, which yields 1D structures having positive velocity gradients with depth (Fig. 1.1b). All models are purely elastic (or asymptotically approximated as such for the reflectivity calculations as described by Yang *et al*., 2007), allowing us to isolate the effects of structural heterogeneity on P_n geometric spreading. Perturbations to the BEM are herein discussed in detail for each class of heterogeneity that we investigate.

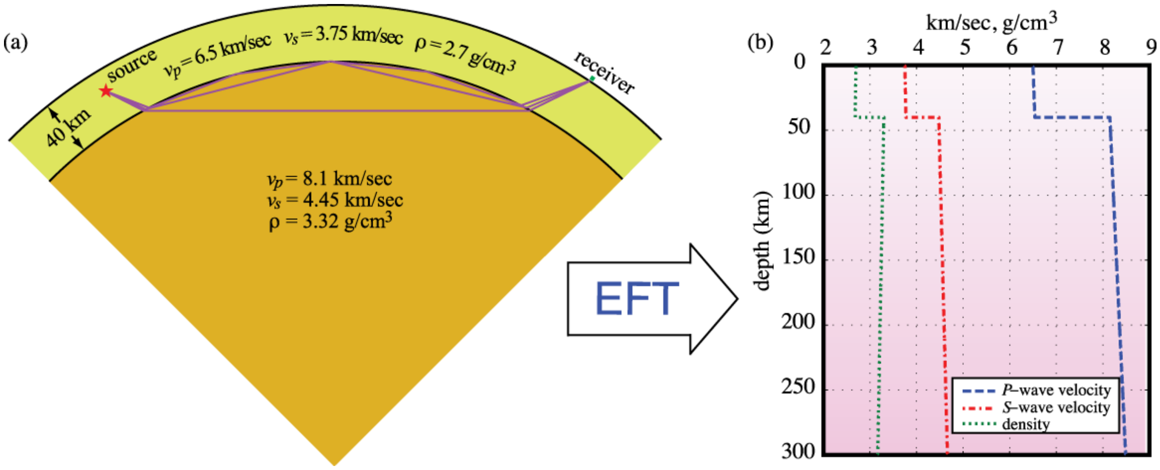

Figure 1.1 (a) Crustal and mantle seismic velocity and density values, layer thickness, and conceptual P_n path for the homogeneous spherical basic Earth model (BEM) used by Yang *et al*. (2007). (b) The associated 1D flat-Earth model, with slight density and seismic velocity gradients resulting from Earth flattening transform (EFT).

The source model is an isotropic point source located at a depth of 15 km. The source-time function for the reflectivity method is a delta function and is a Gaussian derivative source-time function with amplitude normalized to 1 for the finite-difference method. For the 1D velocity models with linear velocity gradients in the mantle lid, we compute both high-frequency reflectivity and lower-frequency finite-difference synthetics. The reflectivity synthetics span the range 0.75-12 Hz, with spectral estimation following the procedures described in Yang *et al.* (2007). The dominant frequency of our finite-difference synthetics is approximately 0.8-1 Hz. The 2D finite-difference modeling approach cannot achieve the very high frequencies of the 1D wavenumber integration method of Yang *et al.* (2007), and full exploration of frequency-dependent effects of the 2D models is beyond our computational limits. However, comparisons of the methods for simple 1D models indicate that the basic behavior of P_n geometric spreading is accurately reproduced by the finite-difference computations for 1-Hz signals. We align the synthetic seismograms with respect to the mantle P-wave velocity (8.1 km/s) and use a fixed-window width of 9 s. The P_n phase onset for the BEM case is approximately 3 s into the fixed window. This window effectively isolates the P_n coda from contamination by the P_g phase following it and allows for arrival time perturbations that result from heterogeneous path structure. The fixed window is only one of several windowing options common in studies of P_n, so we also calculate amplitudes of P_n with a group velocity window (8.2-7.6 km/s) and with a very short fixed window based on P_n onset that approximately captures the first period of the P_n arrival. These three windowing methods span the range of measurement procedures typically used and allow us to consider the nature of geometric spreading for an isolated part of the wavefront versus a coda-dominated signal. Amplitudes are calculated as the rms amplitude of the windowed P_n energy. Corrections are applied to the calculated rms amplitude to approximate a spherical wavefront ($A_f = A_o$ x (1/sqrt(x)), where A_f is the amplitude calculated on a spherical wavefront, A_o is the initial amplitude, and x is distance (in kilometers), and to transform the amplitude (A_f) into that of a wave traveling within a spherical Earth (unflattening transform - see equation 3 in Yang *et al.*, 2007). The P_n amplitude calculations are made in the distance range from 350 to 1500 km to ensure the P_g does not bias the rms amplitude calculation, although the fixed window is still contaminated by P_g for the closest distance.

1.4 P_n Sensitivity to Radial Mantle Lid Velocity Gradients

The radial *P*-wave velocity structure of the uppermost mantle is seldom well-constrained by observations. The most direct constraint is usually provided by curvature of the P_n travel-time branch as a function of distance (e.g., Morozova *et al.*, 1999; Myers *et al.*, 2010) if reliable measurements are available over a wide enough distance range. Even when there is apparent travel-time branch curvature, it is difficult to distinguish between a smooth gradient with depth versus a layered structure with a few or many small velocity increases. Receiver function methods and surface wave dispersion inversions sometimes indicate mantle lid structure, but resolution tends to be poor, especially for *P* velocity, and layered structures are commonly assumed so that any radial gradients are only approximated. When lacking direct constraints, reference velocity structures often assume constant or near-constant velocity in the mantle lid by default, so the BEM model of Yang *et al.* (2007) and Sereno and Given (1990) is representative of many choices. However, there are regions in the Earth where the mantle lid-velocity does appear to increase with depth, with velocity gradients of up to 0.004 s^{-1} according to some studies (e.g., Zhao and Xie, 1993; Morozova *et al.*, 1999), and areas of North

Africa and Eurasia, for example, which evidence suggests have high lateral variations in mantle gradient (Myers *et al.*, 2010). This raises the question of how useful the geometric spreading relations for the BEM are in such regions.

The effect of velocity gradient on P_n geometric spreading is illustrated in Figure 1.2. Using the procedure described in Yang *et al.* (2007), we computed synthetic P_n seismograms for the frequency band of 0.75-12 Hz, using the reflectivity method for models with positive velocity gradients in the mantle lid. The EFT further increases these gradients, causing P_n ray paths to turn even more shallowly in the mantle lid than those for the BEM model. The amplitude-distance behavior is shown for multiple narrow frequency bands for the BEM (red curves) and for models with mantle velocity gradients of 0.002 s^{-1} (blue curves) and 0.004 s^{-1} (black curves). The BEM amplitude curves correspond directly to those for which the geometric spreading formulas of Yang *et al.* (2007) were derived. The systematic variation of P_n-amplitude frequency dependence, with increasing amplitudes and a decrease in the distance at which the minima of the amplitude curves occur, is apparent. The overall shapes of amplitude curves for the different models are similar, with it being apparent that the effect of positive gradient is essentially to shift the curves toward higher frequencies relative to the BEM case. The 0.002 s^{-1} gradient model produces 0.75-Hz amplitudes very similar to the 12-Hz amplitudes for the BEM. This is problematic in that failure to constrain the lid-velocity gradient *a priori* can clearly lead to erroneous frequency dependence of any derived P_n attenuation model in basically the same way that using a frequency-independent geometric spreading assumption does.

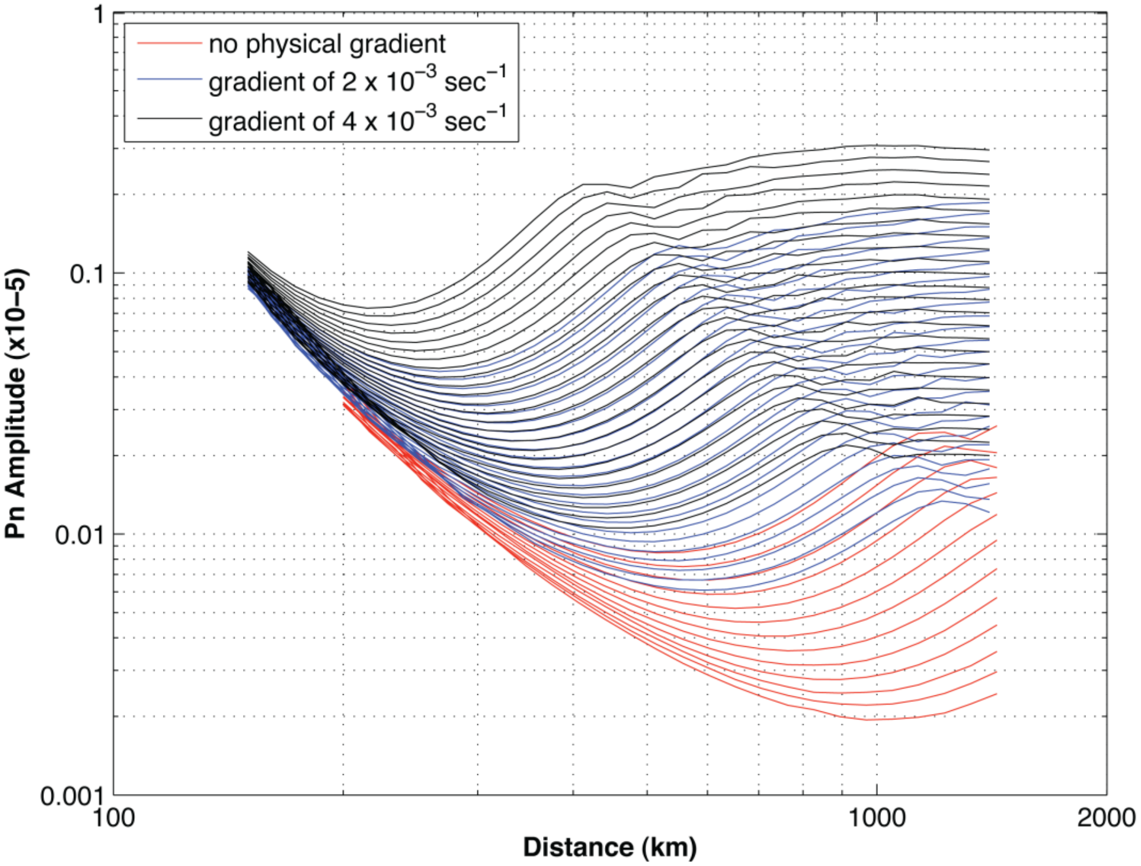

Figure 1.2 P_n amplitude versus distance curves for the BEM (red curves, for no physical gradient in the lid) and for two models with positive gradients in the mantle lid. The suite of curves for each case corresponds to frequencies ranging from 0.75 Hz (lowest curve) to 12 Hz (highest curve). The calculations were done with the reflectivity method, following the procedures of Yang *et al*. (2007).

We made finite-difference calculations of ~1-Hz P_n amplitudes for models with radial *P*-velocity gradients in the mantle lid of 0.001 s^{-1}, 0 s^{-1} (BEM), and -0.001 s^{-1}. The rms amplitudes are shown in Figure 1.3. The BEM case (diamonds) corresponds well with the 1-Hz BEM amplitudes in Figure 1.2, and the positive gradient case (triangles) gives the same shift of the amplitude curve as seen for the corresponding model 1-Hz reflectivity synthetics in Figure 1.2. The -0.001 s^{-1} case almost cancels out the EFT effect

(0.0013 s^{-1}), so this approaches the critical negative gradient that would yield a flat-Earth model with constant half-space velocity and true head-wave behavior of P_n (see discussion in Yang *et al.*, 2007). As expected, the amplitude decay approaches a linear trend in log-amplitude versus log-distance for that situation.

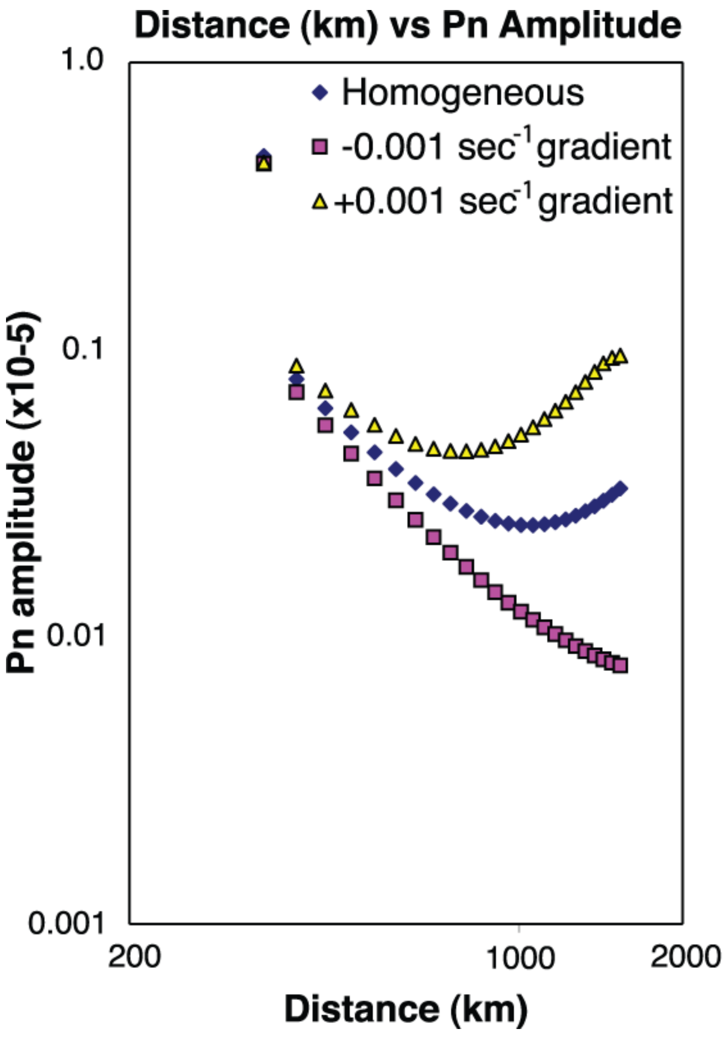

Figure 1.3 P_n amplitude versus distance for the BEM (diamonds), 0.001 s^{-1} positive mantle gradient (triangles), and a -0.001 s^{-1} negative mantle gradient (squares).

Figure 1.2 indicates that it may be possible to use the P_n geometric spreading representation of Yang *et al.* (2007) for the BEM model and determine appropriate coefficients for any specific mantle lid velocity gradient that is larger than the critical negative gradient (-0.0013 s^{-1}), but this is only warranted if there are sufficiently tight *a priori* constraints on the specific model in the region for which the spreading is to be utilized. As this would need to be done on a case-by-case basis, we do not attempt to give generalized spreading corrections for varying mantle lid gradients here; the main result is recognizing the complex nature of the frequency-dependent shift that can result from the presence of small mantle lid velocity gradients comparable to those observed in various regions.

1.5 P_n Sensitivity to Mantle *P*-Velocity Heterogeneity

Given the acute sensitivity of P_n geometric spreading to a usually poorly constrained attribute of the reference velocity model (the radial velocity gradient in the uppermost mantle lid), the stability of the complex behavior of P_n geometric spreading for the BEM in the presence of modest lateral heterogeneity is called into question. Most standard seismological practices assume rather simple reference models, known to be gross approximations of the real structure, under the assumption that errors in the reference model produce only mild biases in other estimated properties such as attenuation. This is simply not the case here, given the nonlinear sensitivity of the P_n whispering gallery arrival to small changes in 1D structures. Clearly, Earth's actual mantle lid has multiscale lateral heterogeneities as well. Does their presence modify the accute sensitivity of P_n spreading relative to the reference BEM structure?

We explore the effects of 2D lateral heterogeneity in the mantle lid velocity structure by adding random lateral velocity heterogeneity characterized by rms velocity fluctuations of a particular strength distribution with random length-scale fluctuations exponentially distributed about prescribed horizontal (Ax) and vertical (Ay) length scales. This allows us to consider 2D random heterogeneity models like that shown in Figure 1.4a, where the heterogeneities are superimposed on the Earth-flattened BEM.

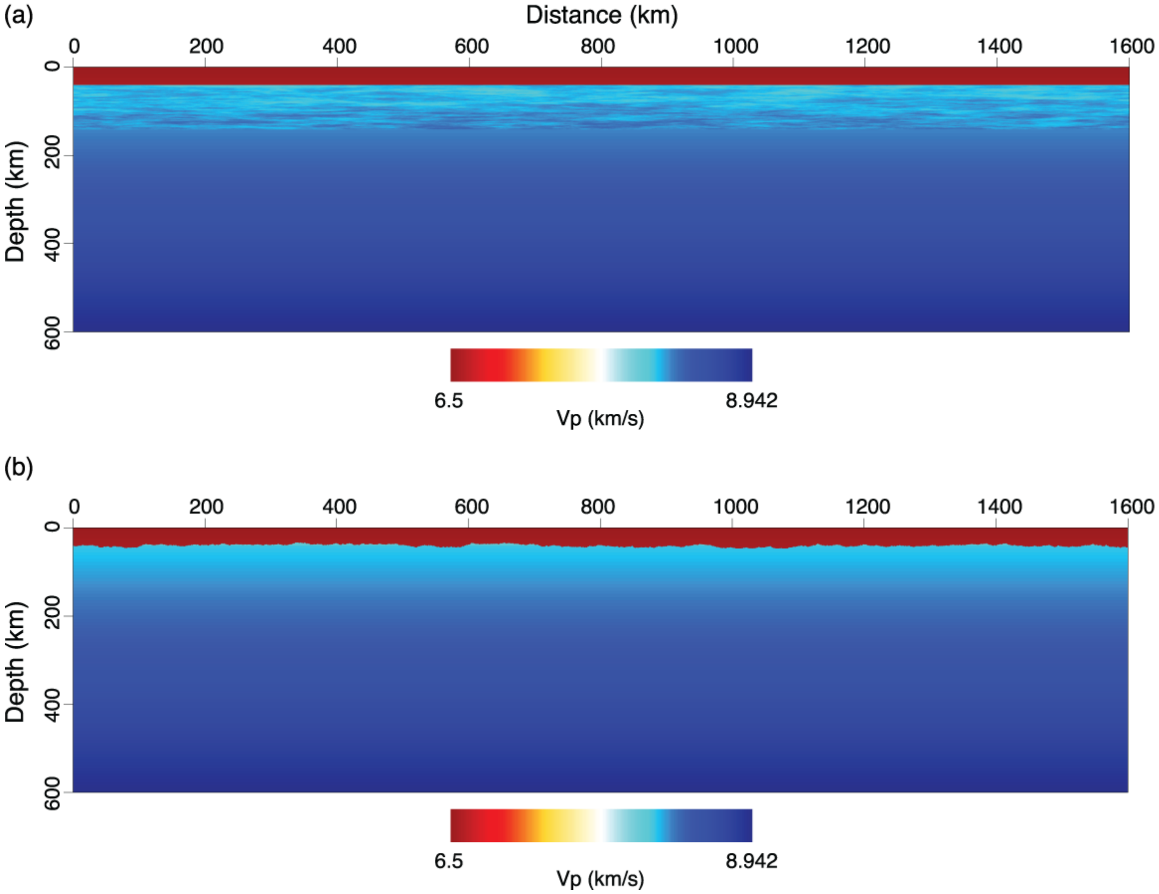

Figure 1.4 (a) Example realization of a velocity model with random *P*-wave velocity (V_p) heterogeneity in the mantle lid. This model has 0.5% rms random volumetric heterogeneities, exponentially distributed about a horizontal length scale of 40 km and a vertical length scale of 3 km. (b) Example realization of a velocity model with random Moho depth fluctuations. This model has 3% rms random Moho depth variations exponentially distributed about a horizontal length scale of 40 km.

Because our finite-difference simulations approximate a purely elastic system, random volumetric heterogeneities include rms perturbations of *P*-wave velocity (V_p), shear-wave velocity (V_s), and density. For each set of random model parameters, V_s varies by the same percent rms as V_p, while density has half the percent rms fluctuation as V_s and V_p. Analysis of the effects of random heterogeneity requires a statistical sampling of the effects associated with different realizations of the random velocity parameters. For each set of random parameters (Ax, Ay, % rms variability), we generate five velocity realizations, and calculate synthetic seismograms for individual realizations. The ensemble average from all five simulations is calculated to represent the result for a given set of random parameters. This modest number of intensive calculations appears to be sufficient to avoid significant bias in behavior associated with any single random configuration (Fig. 1.5). As is always the case with random model parameters, the possibility of outlier behavior and bias of the ensemble still exists, and we do observe significant fluctuation in model P_n amplitudes, so our focus will be on gross attributes of the calculated P_n behavior, not on individual measurements.

Figure 1.5 shows the synthetic P_n amplitudes (~1-Hz rms amplitude in each 9-s-long P_n window) for five realizations of structures with statistical properties corresponding to those in Figure 1.4a, along with averages of the ensemble, and the finite-difference result for the BEM of Yang *et al.* (2007). An interesting behavior in Figure 1.5 is that the presence of volumetric velocity fluctuations with large horizontal aspect ratios systematically affects the basic shape of the geometric spreading, reducing the minimum and allowing better representation by a linear log-log (power-law) type behavior at this frequency. This suggests that the 1D geometric spreading behavior is rather delicate, with modest heterogeneity disrupting the specific interference that gives rise to the complex shape of the amplitude curve with distance. It would be prohibitively expensive (and numerically challenging) to explore the full frequency dependence of this behavior with current computers, but it is likely that at higher frequencies the delicate energy partitioning of the direct P_n and the coupled whispering gallery (as discussed by Yang *et al.*, 2007) would be at least comparably disrupted. Figure 1.6 compares the effect on P_n amplitude of variable percent rms V_p variation in the mantle lid for each of four random heterogeneity configurations with aspect ratios ranging from isotropic (Fig. 1.6a: Ax = 10 km, Ay = 10 km) to large aspect ratio lenslike (Fig. 1.6d: Ax = 40 km, Ay = 3 km). As the aspect ratio increases, the deviations from the BEM solutions tend to increase for weaker heterogeneities. The overall amplitude of P_n also increases with increased rms strength of V_p variation. This is not surprising - heterogeneities with stronger velocity contrasts are expected to disrupt the wave fields more effectively than more subtle velocity fluctuations, expanding the portion of the wavefront that can be scattered into the P_n arrival window. This is illustrated in Figure 1.7 by seismic profiles of synthetic P_n waveforms for the BEM, and for Earth models with large aspect ratio V_p heterogeneity scale parameters corresponding to those in Figure 1.6d, with 1% and 2% rms V_p fluctuations. Note the distortion of the P_n waveform and the presence of significant early coda, indicating a high level of forward scattering of P_n energy within the mantle lid. While the initial motion amplitudes are reduced relative to the homogeneous model, the overall rms values of the full window increase, indicating that signals with a wider range of ray parameters are being scattered into the window.

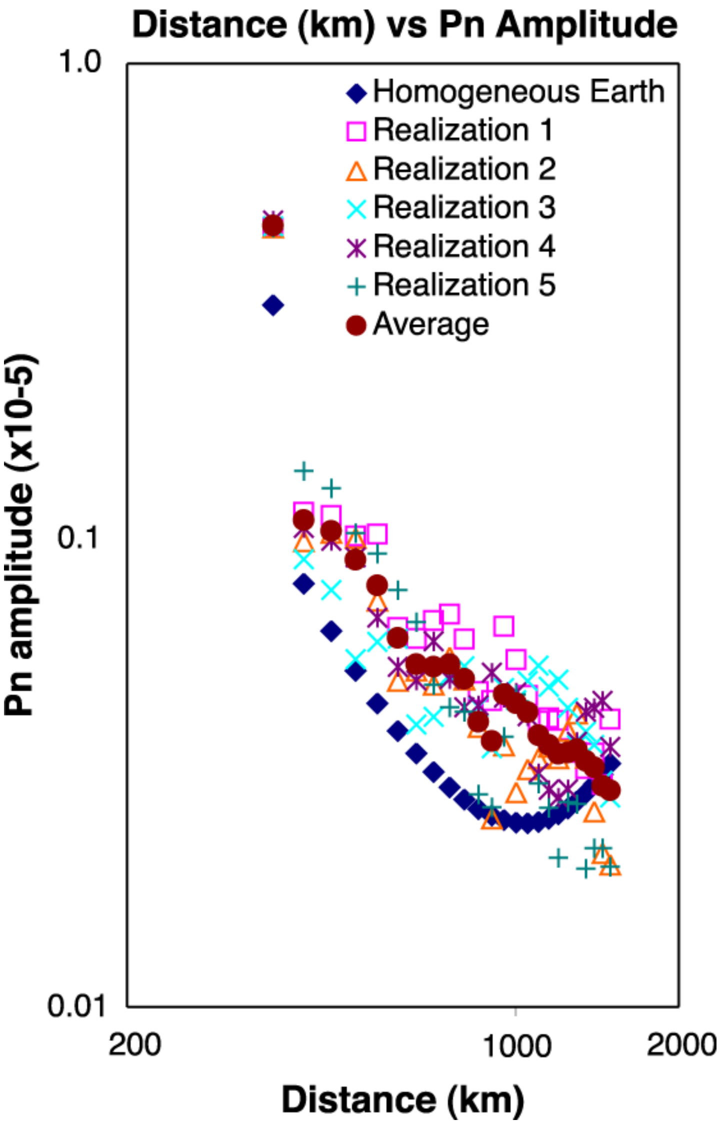

Figure 1.5 P_n amplitude at ~1 Hz plotted with distance for five realizations of random mantle lid volumetric V_p heterogeneity with the same averaging length scales and rms strength distribution shown in Figure 1.4a (Ax = 40 km, Ay = 3 km, RMS = 0.5%). The averages (circles) of these five random realizations are shown, as well as the P_n amplitudes for the BEM (diamonds).

Figure 1.6 (next page) Ensemble-averaged P_n amplitudes as a function of distance for all configurations of random volumetric mantle heterogeneity simulated. P_n amplitude for the BEM (diamonds) are compared to models with 0.5% rms (squares), 1.0% rms (triangles), and 2% rms (xs) V_p fluctuation for horizontal (Ax) and vertical (Ay) averaging lengths of (a) Ax = 10 km, Ay = 10 km (isotropic); (b) Ax = 20 km, Ay = 10 km; (c) Ax = 20 km, Ay = 6 km; and (d) Ax = 40 km, Ay = 3 km. Each value is the average of five realizations with different seed kernels.

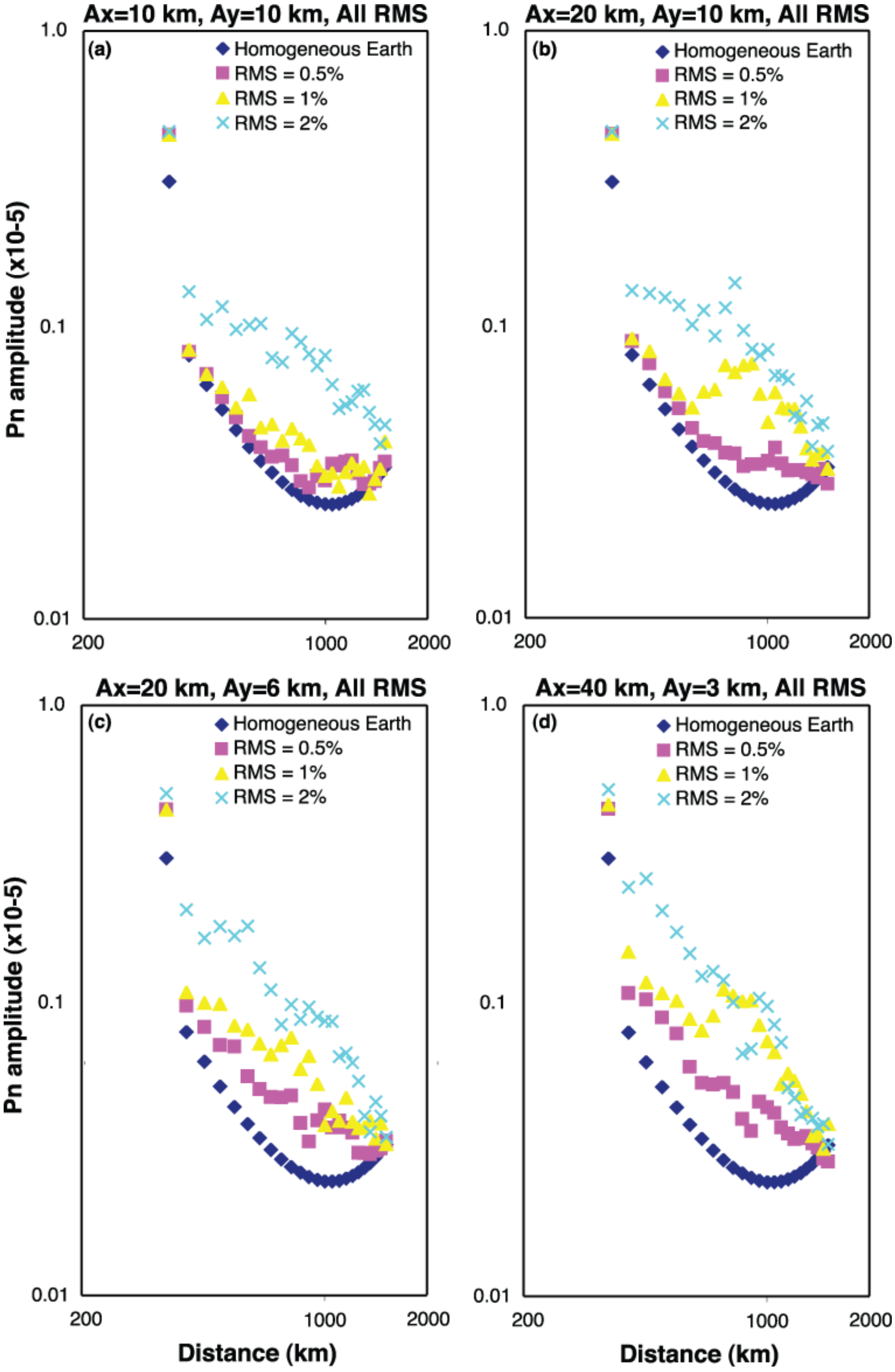
Ax=10 km, Ay=10 km, All RMS
(a)
Ax=20 km, Ay=10 km, All RMS
(b)
Ax=20 km, Ay=6 km, All RMS
(c)
Ax=40 km, Ay=3 km, All RMS
(d)
◆ Homogeneous Earth
■ RMS = 0.5%
▲ RMS = 1%
× RMS = 2%
Pn amplitude (x10-5)
1.0
0.1
0.01
200
1000
2000
Distance (km)

It is also interesting to note the difference in the shape of the amplitude curves in Figure 1.6 as the strength of heterogeneity increases. The same measurements are regrouped in Figure 1.8 by the windowing method, where the averaging lengths vary for models with common levels of 0.5% (Fig. 1.8a,d,g), 1% (Fig. 1.8b,e,h), and 2% rms (Fig 1.8c,f,i) V_p fluctuation. In the 0.5% case, the curve is concave-up for the more isotropic heterogeneities and approximately linear for the more lenslike heterogeneities. When the rms V_p fluctuation is 1%, there is a stronger increase in P_n amplitue as the averaging lengths increase in aspect ratio, with the appearance of a peak around 900 km distance. In the 2% rms V_p variation cases, there is less variation with aspect ratio, and the amplitudes at distances from approximately 400-900 km increase, effectively smoothing out the local amplitude peak at 900 km, as is apparent in the 1% cases. The calculations for 2% rms V_p heterogeneity approach a linear (power-law) trend in log-amplitude versus log-distance, with the slope becoming more steeply negative with increasing aspect ratio of the mantle lid heterogeneity. It might be tempting to view these results as confirmation of the validity of the power-law geometric spreading approximation, but these modeling results correspond to a specific Earth model, as would any linear power-law fit to them. Furthermore, if a log-linear fit to any specific model case was specified, it would not work for most other cases - it would be specific to a single Earth structure or a narrow suite of structural configurations, the fine-scale of which is unconstrained in the actual Earth.

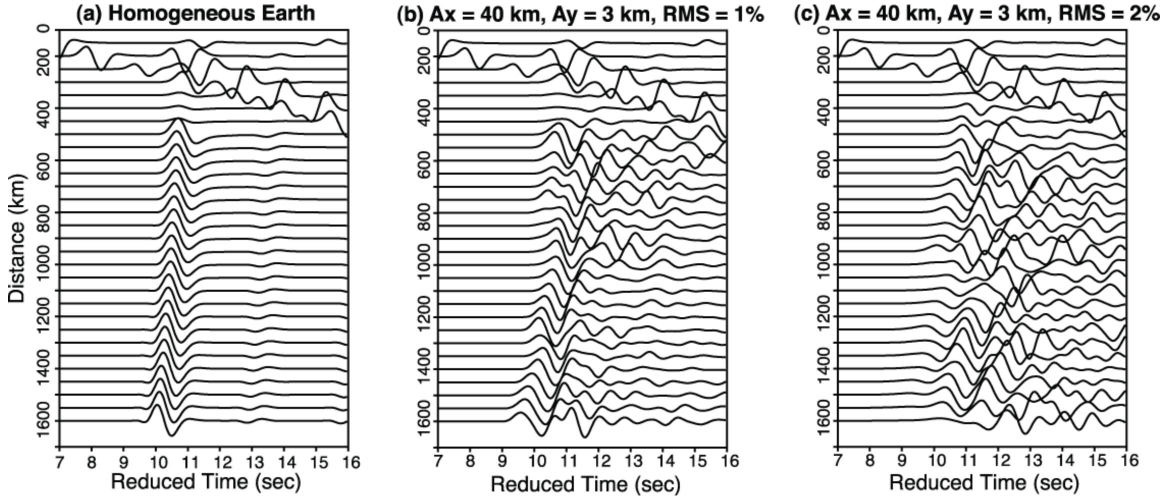

Figure 1.7 Synthetic P_n seismograms generated in (a) the BEM; (b) a velocity model with 1% rms random V_p fluctuations with horizontal averaging length scale of 40 km and a vertical averaging length scale of 3 km; and (c) a velocity model with 2% rms random V_p fluctuations on the same averaging length scales as (b). Each trace is normalized on the largest amplitude.

As Figure 1.6 and Figure 1.8 clearly demonstrate, P_n amplitudes in most model cases increase in response to a heterogeneous mantle lid. The degree to which the amplitudes increase and approach a log-linear trend varies from case to case and by windowing method, as does the rate of amplitude decay. If P_n scattering attenuation were to be included in an apparent attenuation model instead of being inadvertently removed by the geometric spreading approximation, it might be possible in some regions of strong scattering to produce models with negative apparent attenuation. However, Yang *et al.* (2007) applied their BEM geometric spreading correction to a large data set for Eurasia and obtained very reasonable (nonnegative) values, so it seems likely that this would only be the case for very extreme cases.

Each of the amplitude values shown in Figure 1.6 and Figure 1.8 are the average of five individual simulations with random configurations for a given set of parameters, thus the overall behavior is not the effect of any specific structural configuration. For example, the peak in P_n amplitude near 900 km for V_p fluctuations of 1% (Fig 1.8b,e,h) is likely the result of a complex relationship between the strength of the V_p heterogeneities and the angle at which P_n energy penetrates into the uppermost mantle. Mantle lid V_p heterogeneities of ~1% are favorable for concentrating horizontally refracted energy, particularly when higher aspect ratio heterogeneities are present. Stronger heterogeneities do this effectively with little dependence on the shapes of the heterogeneities.

Energy that penetrates into the lid with higher angles of incidence is unlikely to be trapped by these random heterogeneities unless very strong features are immediately encountered. The heterogeneous structures thus capture a limited range of ray parameters, and the increase in amplitude at 900 km represents a tuning of the refractions captured for a specific level of heterogeneity for 1-Hz waves. This interaction between angle of incidence and strength of velocity fluctuation likely underlies why only the strongest V_p heterogeneities have strong effect on P_n amplitudes at all ranges (Fig. 1.8c,f,i) and why the higher aspect ratio heterogeneities (Fig 1.6c,d) have the highest P_n amplitude levels for all distances. The case of P_n amplitude calculated in the short fixed time window (Fig. 1.8g,h,i) is an exception to this pattern, as P_n has the lowest amplitudes at distances greater than 1000 km for 2% V_p fluctuations of all aspect ratios, which become increasingly lowered with heterogeneities of increasing aspect ratio. This is the result of the short window excluding all of the P_n coda following the initial P_n arrival, and reflects the shift in energy distribution resulting from increased mantle heterogeneity.

Figure 1.8 (next page) Ensemble-averaged P_n amplitudes as a function of distance for all configurations of random volumetric mantle heterogeneity (Fig. 1.6), grouped by percent rms fluctuation and windowing method. (a-c) Amplitudes calculated with a 9-s fixed time window; (d-f) amplitudes calculated with a group velocity window (8.2-7.6 km/s); and (g-i) amplitudes calculated with a short (3-s) fixed window positioned based on the onset of P_n. P_n amplitude for the BEM is shown (diamonds) for comparison to heterogeneity with horizontal and vertical averaging lengths of: 10 x 10 km (squares), 20 x 10 km (triangles), 20 x 6 km (xs), and 40 x 3 km (asterisks) for (a,d,g) 0.5% rms V_p fluctuations; (b,e,h) 1% rms V_p fluctuations, and (c,f,i) 2% rms V_p fluctuations.

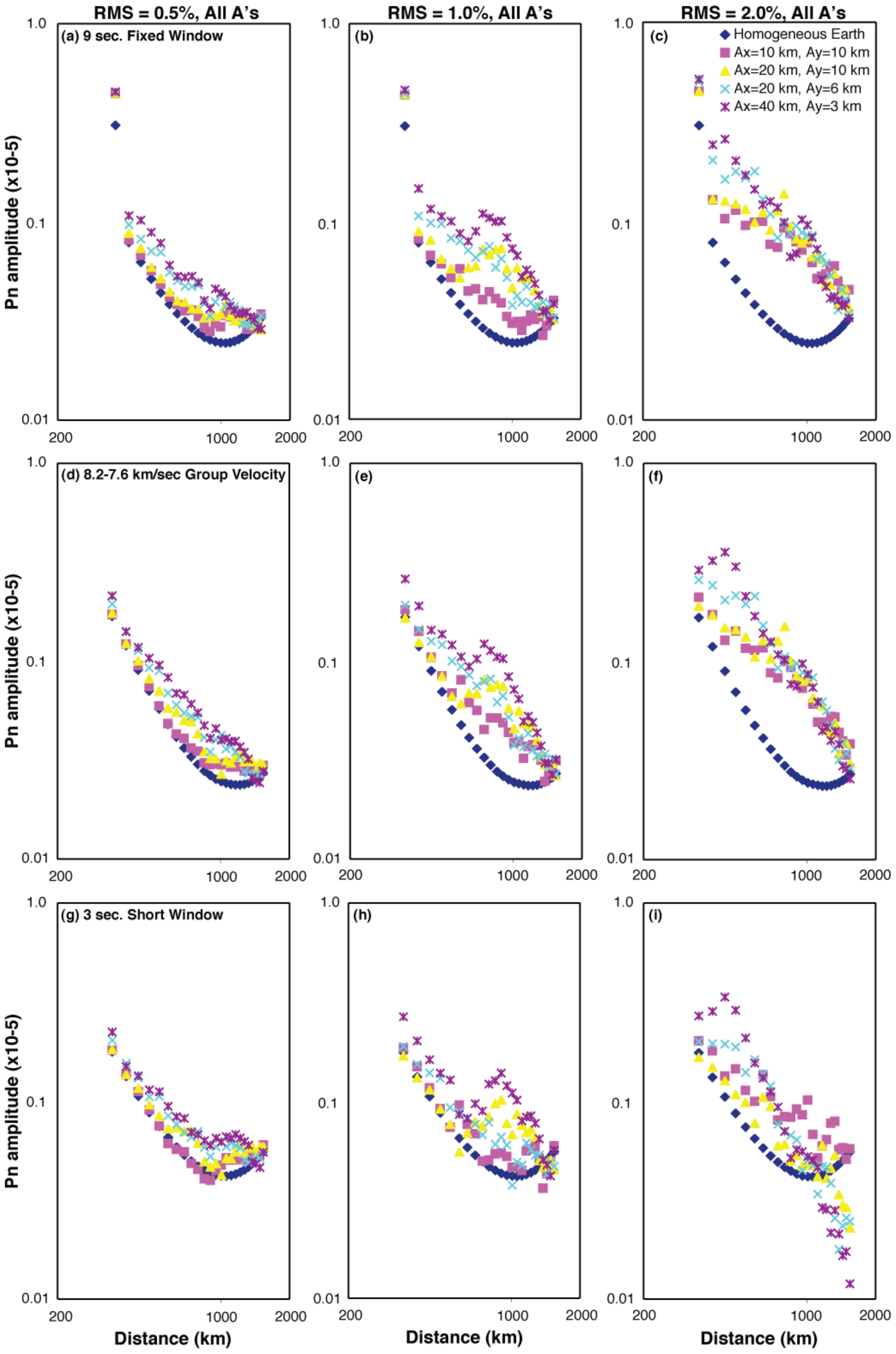

RMS = 0.5%, All A's
RMS = 1.0%, All A's
RMS = 2.0%, All A's
(a) 9 sec. Fixed Window
(b)
(c)
(d) 8.2-7.6 km/sec Group Velocity
(e)
(f)
(g) 3 sec. Short Window
(h)
(i)
◆ Homogeneous Earth
■ Ax=10 km, Ay=10 km
▲ Ax=20 km, Ay=10 km
× Ax=20 km, Ay=6 km
✱ Ax=40 km, Ay=3 km
Pn amplitude (x10-5)
1.0
0.1
0.01
200
1000
2000
Distance (km)

The longer time windows (group velocity and fixed window) show increased amplitude with higher aspect ratio because they are dominated at greater distances by the scattered P_n energy that is captured and returned to the surface by the heterogeneous velocity structure, whereas the short window shows greatly decreased amplitude of the initial P_n arrival at greater distances. Regardless of the windowing scheme used, the strongest heterogeneities with the highest aspect ratios have the most dramatic effects on P_n amplitude. The specific geometric spreading behavior of the BEM or the 1D gradient models is clearly a result of rather delicate energy partitioning between diving energy and the suite of multiply reflected underside Moho reflections that is corrupted by the presence of small velocity fluctuations and associated multipathing. We now examine whether a rough Moho boundary has comparable effects.

1.6 P_n Sensitivity to Moho Topography

Volumetric heterogeneity in the mantle lid is expected to result from geological processes during crustal formation and evolution, and the same is true for Moho boundary irregularities on multiple scales. P_n interactions with the Moho near the source and the receiver, as well as throughout the mantle lid propagation and whispering gallery development, should yield P_n sensitivity to the Moho roughness. Models with large-scale variations in crustal thickness are available, and one can make geometric spreading calculations for a specific deterministic model if the structure is known; however, relatively little constraint exists on the spectrum of small-scale Moho irregularities likely to affect any specific P_n phase or average behavior within a given region. We have parameterized 2D exponential-distribution statistical irregularities in the Moho depth (a realization of which is shown in Fig. 1.4b) in otherwise homogeneous (BEM) velocity layering to explore the effects of random Moho topographic irregularities on P_n geometric spreading. We conducted simulations with Gaussian-distributed random Moho irregularity as well, finding comparable overall simulation results for a 1-s dominant period. The main difference between the distributions is that the exponential model is much richer in small-scale structure and produces longer persisting coda than the smoother Gaussian model.

We created velocity models with Moho irregularity having four different averaging length scales, with random horizontal length scale exponentially distributed about distances ranging from 20 to 160 km. Topography of the Moho boundary is modeled with 1% (±0.4 km), 3% (±1.2 km), or 5% (±2.0 km) rms fluctuations for each of the distance scales. There are few observational constraints on the appropriate statistics for Moho irregularities in general, but these values are representative of fluctuations in reflection seismology imaging. The average Moho depth always remains 40 km, as in the BEM. Results of these simulations are shown in Figure 1.9, grouped by horizontal averaging length, and in Figure 1.10, grouped by rms height of Moho topography and windowing scheme. These are again ensemble average values from five different model realizations for each set of random parameters. In Figure 1.9a, for 20-km averaging length, the 3% height variation actually reduces the average P_n amplitudes to below those for the BEM. The strongest positive perturbations to P_n amplitudes relative to the BEM result from Moho variations distributed around the 40-km averaging length scale (Fig. 1.9b). For this horizontal averaging scale, the amplitude scatter becomes significant for

5% rms heterogeneity in the Moho topography. There is only minor sensitivity to the choice of horizontal averaging function for values larger than 40 km.

Figure 1.10 displays the effects of percent topography fluctuation more clearly, with 1% rms variability having little effect on P_n amplitude for any of the horizontal length scales simulated and 5% height fluctuation clearly disrupting the P_n geometric spreading pattern relative to the BEM. The disruption mainly involves increased amplitude scatter without a systematic shift in the pattern, as was found in the volumetric heterogeneity simulations. Moho topographic variability of 3%-5% is required for all horizontal averaging scales in order to produce significant scatter in P_n amplitudes. We attribute most of this amplitude variability to the sensitivity of the ray paths for P_n as it first encounters and refracts at the Moho, although progressive scattering along the horizontal path contributes overall. The consistency of the P_n amplitude calculations (relative to the homogeneous model case) across all windowing methods confirms that fluctuations in amplitude are mostly controlled by the first refraction of P_n at the Moho, and the effect of forward-scattered wave energy along the Moho on P_n amplitudes is relatively minor, as compared to the amplitudes calculated in the model cases of mantle heterogeneity, which are dominated by scattered P_n energy. The amoung of forward-scattered P_n energy depends on the direction that the boundary is dipping below the source, as well as how steeply it is dipping, and even with five realizations being averaged, there is rapid fluctuation in amplitudes that emerge at various distances.

Figure 1.9 (next page) Ensemble-averaged P_n amplitudes plotted as a function of distance for all configurations of random Moho topography heterogeneity, grouped by horizontal averaging length scale, Ax. P_n amplitude for the BEM (diamonds) are compared to amplitudes for simulations with 1% rms (squares), 3% rms (triangles), and 5% rms (xs) Moho depth variations for horizontal averaging length scales of (a) 20 km, (b) 40 km, (c) 80 km, and (d) 160 km.

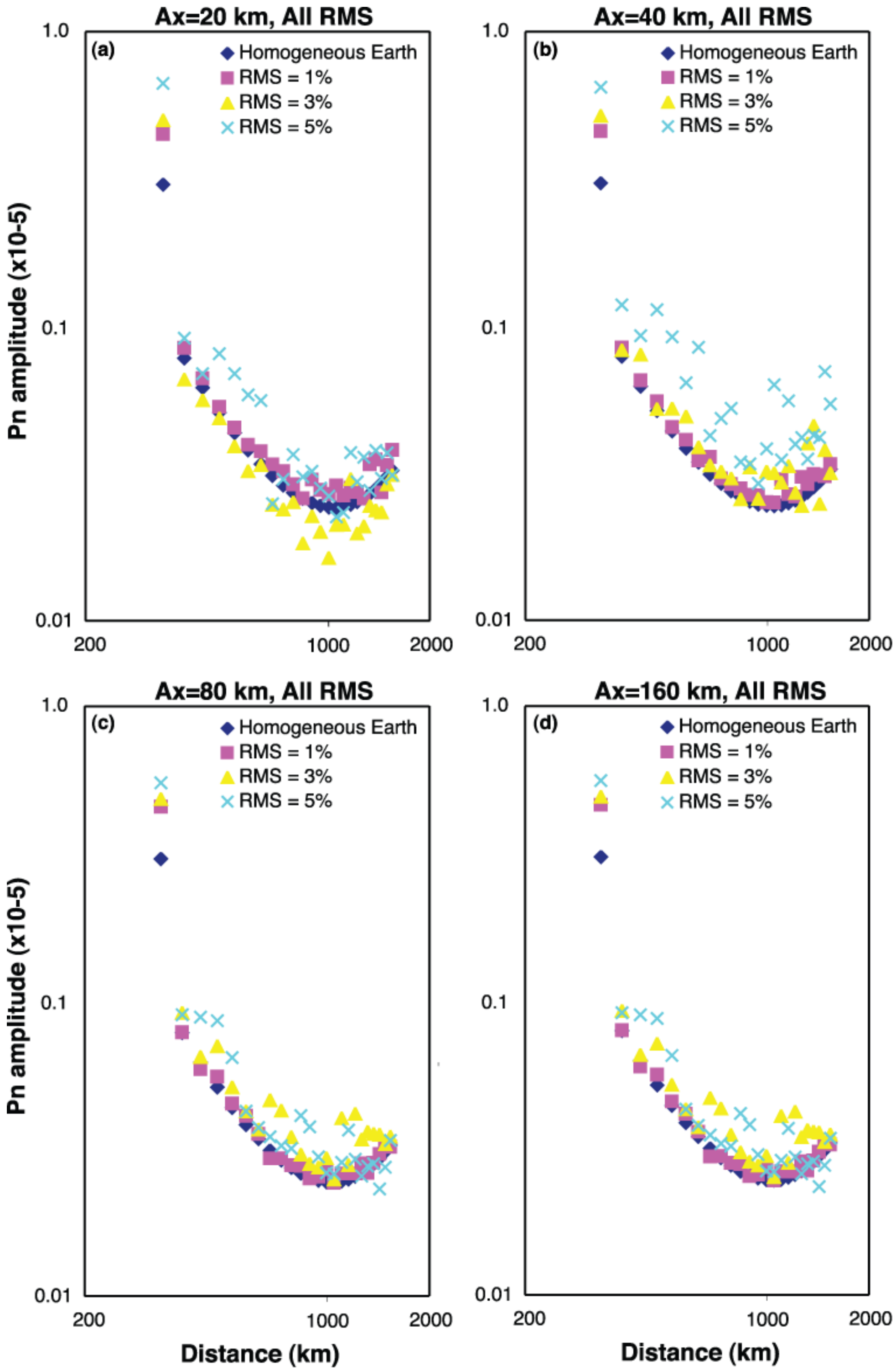
Ax=20 km, All RMS
Ax=40 km, All RMS
Ax=80 km, All RMS
Ax=160 km, All RMS
(a)
(b)
(c)
(d)
◆ Homogeneous Earth
■ RMS = 1%
▲ RMS = 3%
× RMS = 5%
Pn amplitude (x10-5)
1.0
0.1
0.01
200
1000
2000
Distance (km)

When the synthetic waveforms are examined (Fig. 1.11), one can see that Moho variability strongly affect P_n arrival time (mainly because the crustal thickness is locally thicker or thinner near the source and receiver, depending on the specific Moho topography) but also results in moderate scattering of P_n energy, as evidenced by the enhanced P_n coda following the first arrival. Given that all of the scattering in these models must originate at the Moho, the coda levels are influenced by both near-source and near-receiver scattering along with scattering of energy out of the whispering gallery of underside Moho reflections.

1.7 Discussion and Conclusions

The behavior of P_n geometric spreading is subtle and complex, even for simple 1D structures (e.g., Menke and Richards, 1980; Sereno and Given, 1990; Yang *et al.*, 2007). The calculations in this study provide a basic explanation for the high variance observed in P_n rms amplitudes from the ANOVA analysis (Fisk *et al.*, 2008) mentioned in the Introduction. Variable 1D and 2D structures readily produce nonlinear, frequency-dependent variations superimposed on the already complex behavior for the simple BEM. This variability is somewhat analogous to the higher variance found for m_b measurements for teleseismic *P* waves versus the less-variable $m_b(L_g)$ for complex, but heavily path-averaging regional L_g phases; the energy in the P_n window is comprised of a fairly narrow range of ray parameter arrivals that are very sensitive to the structure along any specific path.

Figure 1.10 (next page) Ensemble-averaged P_n amplitudes plotted as a function of distance for all configurations of random Moho topography heterogeneity, grouped by percent rms depth fluctuation and windowing method. (a-c) Amplitudes calculated with a 9-s fixed time window; (d-f) amplitudes calculated with a group velocity window (8.2-7.6 km/s); and (g-i) amplitudes calculated with a short (3-sec) fixed window positioned based on the onset of P_n. P_n amplitude for the BEM (diamonds) are compared to horizontal averaging length scales of 20 km (squares), 40 km (triangles), 80 km (xs), and 160 km (asterisks), for percent rms depth fluctuations of 1% for (a, d, g); 3% for (b, e, h), and 5% for (c, f, i).

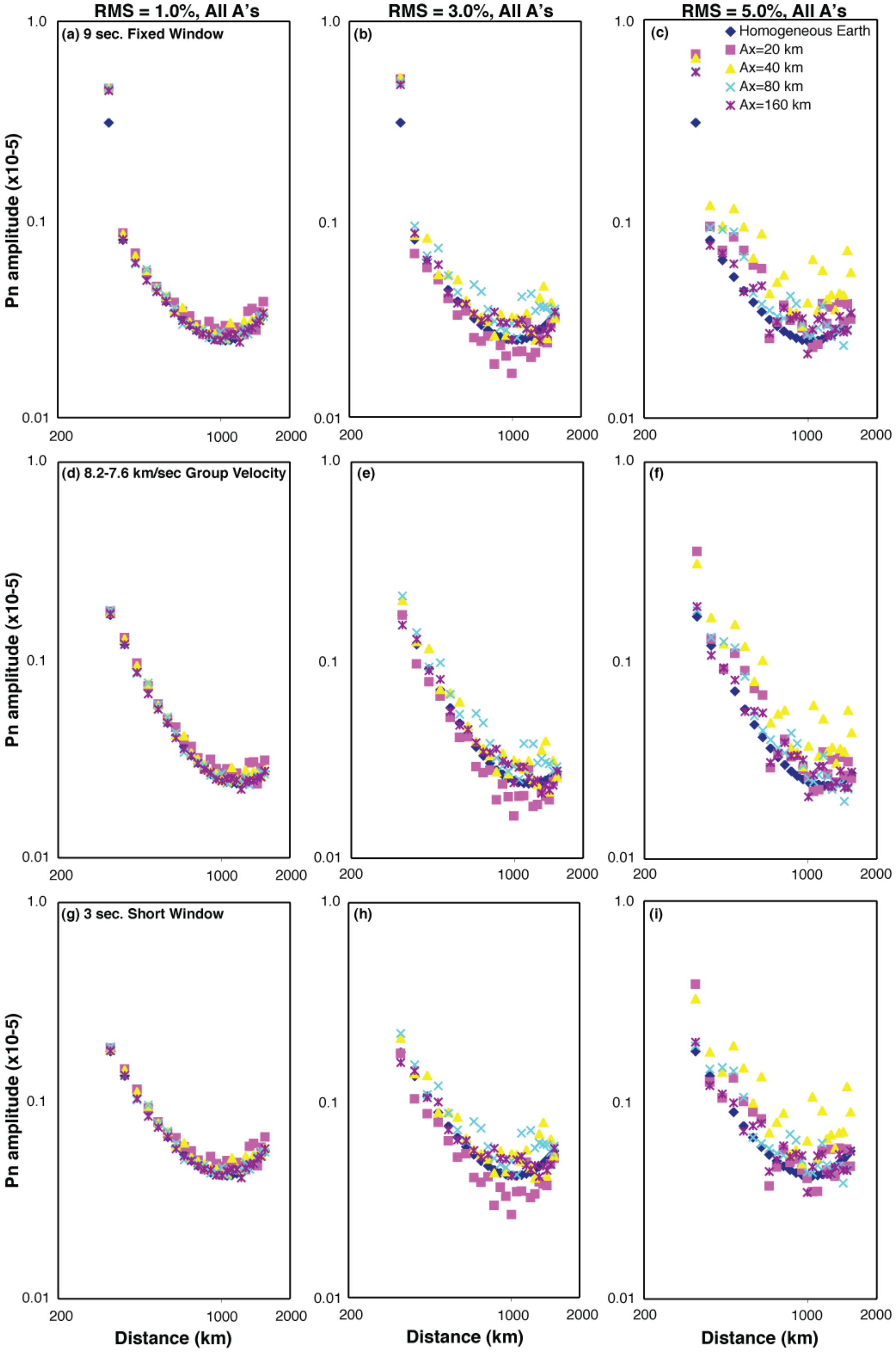
RMS = 1.0%, All A's
RMS = 3.0%, All A's
RMS = 5.0%, All A's
(a) 9 sec. Fixed Window
(b)
(c)
Homogeneous Earth
Ax=20 km
Ax=40 km
Ax=80 km
Ax=160 km
(d) 8.2-7.6 km/sec Group Velocity
(e)
(f)
(g) 3 sec. Short Window
(h)
(i)
Pn amplitude (x10-5)
1.0
0.1
0.01
200
1000
2000
Distance (km)

This study demonstrates that the effects of variable 1D mantle lid *P* velocity gradients preserve the basic functional form of the frequency-dependent complexity of the constant-velocity mantle lid model, with positive gradients causing a shift of amplitude curves toward higher frequencies relative to the zero-gradient BEM. The effects are so strong that specific frequency-dependent coefficients would need to be determined for the spreading model for any specific gradient. The nonlinear sensitivity rases questions about the choice of spreading model given typical situations where there is little or no information on the local mantle lid velocity gradients. Of course, if the data for a given region are sufficient to constrain the mantle lid velocity gradient (as may be the case across the Russian platform; e.g., Morozova *et al.*, 1999), specific spreading computations can provide a local reference behavior relative to which attenuation estimates can more reliably be determined. In practice, this is still challenging, given the degenerate nature of layered versus gradient model fits to first-arrival times.

Computations with lateral volumetric heterogeneities in the mantle lid and statistical irregularities in Moho topography add significant complexity to the general problem of approximating P_n geometric spreading. Our 2D finite-difference simulations indicate that the precise shape of the geometric spreading behavior for 1D models can be disrupted by even moderate levels of lateral heterogeneity, and the behavior for 1-s period waves moves toward a power-law representation as the level of volumetric heterogeneity increases and as the horizontal-to-vertical aspect ratio of the heterogeneities increases. This behavior may provide a rationale for using a conventional power-law type geometric spreading correction, but how closely such a model approximates actual P_n behavior depends critically on the level and type of heterogeneity present in the real Earth. For example, simulations with subtle mantle heterogeneity (0.5% rms V_p fluctuations; Fig. 1.8a,d,g) indicate that P_n geometric spreading can be more closely approximated by the 1D homogeneous BEM relations determined by Yang *et al.* (2007), while simulations with stronger mantle heterogeneity (Fig 1.8c,f,i) can be better approximated by a power-law type correction, at least for 1 Hz, although a single linear decay rate would not fit all cases approching a log-linear decay. The P_n amplitudes of simulations through velocity models between these two end members cannot be particularly well fit by either type of geometric spreading correction.

For rough Moho topography heterogeneity, departures from the 1D P_n geometric spreading pattern prove much less significant. Models with 3%-5% topographic fluctuations over scale lengths of approximately 80 km seem to have the greatest effect on P_n amplitude near 1 Hz, but, for nearly all simulations, the BEM geometric spreading correction of Yang *et al.* (2007) would be an acceptable reference model.

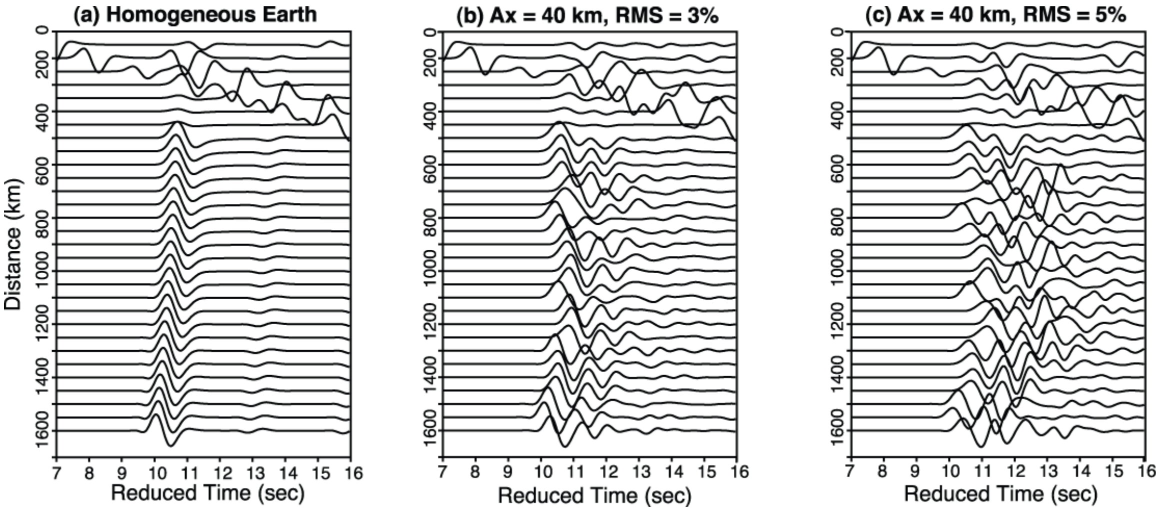

Figure 1.11 Finite-difference synthetic P_n seismograms generated in (a) BEM; (b) a velocity model containing 3% rms random Moho depth variation with horizontal averaging scale length of 40 km; and (c) a velocity model with 5% rms random Moho depth variation along horizontal averaging scale length of 40 km. Each trace is normalized on the largest amplitude.

These results present something of a conundrum: the 1D BEM structure considered by Yang *et al.* (2007) is very simple but produces complex, frequency-dependent, geometric spreading behavior. Our results show that the behavior is nonlinearly sensitive to the model parameters, and the 1D gradient models indicate that this extends to the frequency dependence. However, our 2D models with the strongest, but still geologically plausible, mantle heterogeneities produce relatively simple patterns of geometric spreading, at least for 1 Hz. It is likely that P_n simulations over a broader frequency band and for 3D structures would also have high sensitivities to different scale lengths and velocity contrasts as a function of frequency. The effects of 2D or 3D V_p heterogeneity on shorter period signal have not been quantitatively assessed for the long propagation distances considered here; doing so presents formidable computational challenges. We speculate that eventually simulations in heterogeneous 3D structures will enhance the tendencies manifested in our 2D calculations.

Prior studies of P_n attenuation efforts have usually assumed simple frequency-independent power-law geometric spreading behavior for P_n (e.g., Sereno *et al.*, 1988, Pasyanos *et al.*, 2009), which is not a realistic form of spreading for any known 1D (i.e., laterally homogeneous) velocity model. This assumption may actually yield reasonable results to the extent that the specific power-law corresponds to a fairly high degree of uppermost mantle velocity heterogeneity in the real 3D Earth, which may be evidenced in the data by the amount of coda following the initial P_n arrival (Fig. 1.7 and Fig. 1.11). Of course, the precise spectrum and statistical distribution of real mantle lid heterogeneities are not known for any specific path, just as the precise best 1D lid velocity gradient is not reliably known, so it would be difficult to estimate a particular small-scale structural configuration with a power-law geometric spreading approximation that has an appropriate decay rate. That situation is unlikely to change in general. Conventionally, seismic reference models used for computing geometric spreading of seismic signals with a limited ray parameter range are selected to be very simple structures rather than such complex (and unspecified) structures that the wave field is scattered to the point of allowing an energy flux power-law assumption to be made (as is quite reasonably done for the multi-ray parameter phases like L_g). It should be recognized that if one assumes (arbitrarily) a power-law form of geometric spreading for P_n, the underlying reference Earth model is explicitly not a conventional 2D constant-velocity mantle model or even a constant lid-gradient model, but is intrinsically a statistically heterogeneous model with unspecified properties. It is rather uncomfortable to invoke such a model. In addition, we recognize that even though scattering due to velocity heterogeneities is an elastic effect, the single-wavefront definition of geometric spreading is often assumed, and elastic scattering effects are considered part of the apparent attenuation.

Our recommendation is that, in the absence of specific regional constraints on the mantle lid velocity gradient and on small-scale heterogeneity in the lid and in Moho topography, the best choice for P_n geometric spreading is the frequency-dependent version found for the BEM by Yang *et al.* (2007). This has the primary merit of having a known, simple 1D Earth model associated with the geometric spreading behavior and a parameterization that can accommodate the nonlinear response of P_n to large-scale changes in the Earth velocity model (e.g., mantle gradient), which is consistent with standard seismological modeling practices. If this model is used in determining an apparent attenuation structure, the attenuation model will very likely have explicit frequency dependence. As is always the case, deficiencies in the spreading corrections will likely project into the attenuation model, but, as long as the resulting attenuation model is viewed as a colletive parameterization of intrinsic *P* wave attenuation, correction for scattering attenuation (which could involve negative *Q*s), and frequency-dependent errors in the geometric spreading relations (which, based on our modeling results, could approach a factor of 10 for any relation chosen), at least the attenuation model is defined relative to a known elastic Earth model. With most applications involving a convolution of the geometric spreading and attenuation models, the trade-offs will not bias source strength estimates; but one must exercise care in specific interpretation of attenuation parameters in terms of Earth properties. Decoupling geometric spreading and attenuation can only occur with *a priori* constraint on the structure (e.g., using travel-time curves to constrain the upper-mantle velocity gradient), but small-scale structure of the type modeled here is largely unconstrained. Investigators should be aware that by adopting a specific geometric spreading approximation, they are also adopting assumptions about Earth structure. It is therefore imperative that investigators document the assumptions inherent in any geometric spreading approximation chosen in attenuation modeling studies to prevent assumptions specific to a given study region from being erroneously applied to other regions. It could be argued that, with amplitude variations between a heterogeneous Earth model and a homogeneous Earth model as large as they are, an approximation of P_n geometric spreading should in some way account for scattering due to small-scale heterogeneity. This is problematic, as the small-scale heterogeneity is not known. The data can serve as somewhat of a guide, with observed P_n-P_n coda variations indicating a strong or weak scattering domain, but quantitatively linking the data to a specific heterogeneous model remains beyond our scope as a community. By continuing efforts to constrain the mantle lid velocity gradient empirically, or to use independent knowledge of the Moho topography, calculations of geometric spreading for corresponding models can be performed to enable better resolution of true attenuation effects.

It is clear from these simulations that either the 1D BEM geometric spreading corrections of Yang *et al*. (2007) or any power-law correction will have significant uncertainty in approximating the actual geometric spreading of P_n for specific data sets; neither is ideal for all cases. The extent of this uncertainty is difficult to quantify, given the lack of constraints on the small-scale seismic velocity heterogeneity spectrum within the real Earth. Thus, propagating realistic uncertainties in the geometric spreading model into formal uncertainties in attenuation model estimates remains very difficult. We seek to perform future calculations for 3D structures with greater bandwidth, with the goal of providing useful quantification of the uncertainties in attenuation modeling due to geometric spreading approximation.

1.8 Data and Resources

All data used in this paper came from published sources listed in the references.

1.9 Acknowledgments

We thank George Randall of Los Alamos National Laboratory for assisting us with his reflectivity code. We thank Yaofeng He, for helpful discussion and advice on the two-dimensional finite-difference calculations. Many thanks also to Bill Walter and Igor

Morozov for their insightful reviews. This work was performed under the auspices of the U.S. Department of Energy by Los Alamos National Laboratory and University of California Santa Cruz under contracts DE-AC52-06NA25396 and DE-FC52-05NA26606.

1.10 References

Buldyrev, V.S., and A.I. Lanin (1965). Interfering waves at the surface of an elastic inhomogeneous sphere, *Rev. Geophys.* **3,** 49-54.

Chapman, C.H. (1973). The Earth flattening transformation in body wave theory, *Geophys. J. R. Astr. Soc.* **35,** 55-70.

Fisk, M.D., S.R. Taylor, T. Lay, and X. Xie (2008). Analysis and modeling of regional seismic phases at nuclear test sites: Implications for *P/S* discrimination, *NNSA Report MRC/WDC-R-560*, 99 pp.

Hartse, H.E., S.R. Taylor, W.S. Phillips, and G.E. Randall (1997). A preliminary study of regional seismic discrimination in central Asia with emphasis in western China, *Bull. Seismol. Soc. Am.* **87,** 551-568.

Hill, D.P. (1973). Critically refracted waves in a spherically symmetric radially heterogeneous Earth model, *Geophys. J. R. Astr. Soc.* **34,** 149-177.

Menke, W.H., and P.G. Richards (1980). Crust-mantle whispering gallery phases: A deterministic model of teleseismic P_n wave propagation, *J. Geophys. Res.* **85,** 5416-5422.

Morozov, I. (2010). On the causes of frequency-dependent apparent seismological *Q*, *Pure Appl. Geophys.* **167,** 1131-1146, doi 10.1007/s00024-010-0100-6.

Morozova, E.A., I.B. Morozov, and S.B. Smithson (1999). Heterogeneity of the uppermost mantle beneath Russian Eurasia from the ultra-long-range profile QUARTZ, *J. Geophys. Res.* **104,** 20,329-20,348.

Müller, G. (1977). Earth-flattening approximation for body waves derived from geometric ray theory - Improvements, corrections and range of applicability, *J. Geophys.* **42,** 429-436.

Myers, S.C., M.L. Begnaud, S. Ballard, M.E. Pasyanos, W.S. Phillips, A.L. Ramirez, M.S. Antolik, K.D. Hutchenson, J.J. Dwyer, C.A. Rowe, and G.S. Wagner (2010). A crust and upper-mantle model of Eurasia and North Africa for P_n travel-time calculation, *Bull. Seismol. Soc. Am.* **100,** 640-656, doi 10.1785/0120090198.

Pasyanos, M.E., W.R. Walter, and E.M. Matzel (2009). A simultaneous multiphase approach to determine *P*-wave and *S*-wave attenuation of the crust and upper mantle, *Bull. Seismol. Soc. Am.* **99,** 3314-3325, doi 10.1785/0120090061.

Randall, E.G. (1994). Efficient calculations of complete differential seismograms for laterally homogeneous Earth models, *Geophys. J. Int.* **118,** 245-254.

Sereno, T.J., and J.W. Given (1990). P_n attenuation for a spherically symmetric Earth model, *Geophys. Res. Lett.* **17,** 1141-1144.

Sereno, T.J., S.R. Bratt, and T.C. Bache (1988). Simultaneous inversion of regional wave spetra for attenuation and seismic moment in Scandinavia, *J. Geophys. Res.* **93,** 2019-2036.

Taylor, S.R. A.A. Velasco, H.E. Hartse, W.S. Phillips, W.R. Walter, and A.J. Rodgers (2002). Amplitude corrections for regional seismic discriminants, *Pure Appl. Geophys.* **159,** 623-650.

Walter, W.R., and S.R. Taylor (2001). A revised magnitude and distance amplitude correction (MDAC2) procedure for regional seismic discriminants: Theory and testing at NTS, *Lawrence Livermore National Laboratory Report UCRL-ID-146882*, 13 pp.

Walter, W.R., K.M. Mayeda, and H. Patton (1995). Phase and spectral ratio discrimination between NTS earthquakes and explosions, Part I: Empirical observations, *Bull. Seismol. Soc. Am.* **85,** 1050-1067.

Xie, X., and T. Lay (1994). The excitation of L_g waves by explosions: A finite-difference investigation, *Bull. Seismol. Soc. Am.* **84,** 324-342.

Yang, X. (2002). A numerical investigation of L_g geometric spreading, *Bull. Seismol. Soc. Am.* **92,** 3067-3079.

Yang, X., T. Lay, X. Xie, M.S. Thorne (2007). Geometric spreading of P_n and S_n in a spherical Earth model, *Bull. Seismol. Soc. Am.* **97,** 2053-2065.

Zhao, L.S., and J. Xie (1993). Lateral variations in compressional velocities beneath the Tibetan Plateau fom P_n travel time tomography, *Geophys. J. Int.* **115,** 1070-1084.

Chapter 2

Calculating 3D teleseismic *P*-wave Green's functions: Capturing near-source 3D waveform complexity in synthetic teleseismic *P*-waves

Megan Avants[1], Thorne Lay[1], and Arthur Rodgers[2]

[1] *University of California Santa Cruz, Department of Earth and Planetary Sciences*
[2] *Lawrence Livermore National Laboratory, Geophysical Monitoring Program*

2.1 Abstract

Regional and teleseismic recordings of seismic events are used to determine source location, depth, and timing of a seismic event, as well as to discriminate between naturally occurring seismic events and nuclear test explosions. Observations of the trio of underground nuclear tests conducted in North Korea illustrate the dramatic effect of surface topography on regional interference phases and teleseismic depth phases. These signals demonstrate the difficulty in accurately determining source characteristics from seismic waves strongly affected by scattering structure, in this case, dramatic surface topography in the mountainous test site region of North Korea. Given the geopolitical limitations on the availabity of seismic data near any given nuclear test region and the extreme azimuthal, distance, and frequency dependence of scattering attenuation effects on regional phases in strongly heterogeneous regions, we have developed a hybrid method of simulating teleseismic *P*-waves that originate in a 3D near-source region, but are propagated to teleseismic distances through a 1D Earth structure. This is accomplished by first capturing *P*-wave energy propagated through a 3D near-source model region, and then employing the representation theorem to calculate 3D teleseismic *P*-wave Green's functions for 1D propagation of the signal through the relatively simple

structure of the Earth's mantle, to teleseismic distances. We present the development of this method and results of benchmark test calculations here.

2.2 Introduction

Recordings of seismic waves are used to locate, identify, and estimate the yield of nuclear explosions, in addition to locating, characterizing, and determining the magnitude of naturally-occurring seismic events (earthquakes, volcanic eruptions, etc.). Near-source heterogeneities, whether layered media, small-scale lateral crustal / upper-mantle heterogeneity resulting from tectonic processes (e.g., McLaughlin et al., 1992; Okamoto, 1993; Pitarka et al., 2007; Rodgers et al., 2010; Stevens and Xu, 2010; Taylor and App, 2010; Avants et al., 2011), or boundary / surface topography (e.g., Stead and Helmberger, 1988, He et al., 2008), imprint the seismic wave field by refracting, reflecting, or severely disrupting raypaths through multiple reflections (scattering). These effects on the seismic waves persist throughout their path, potentially obscuring source characteristics such as location, depth, source type, and magnitude in the recorded signal. Observations of the trio of underground nuclear tests in North Korea illustrate that surface topography can strongly scatter seismic energy from a shallow source, affecting relative amplitudes of discriminant phases by preferentially partitioning scattered seismic energy into regional phases that travel within the crustal waveguide (e.g., Rodgers et al., 2010). This also results in multiple *P-S* phase conversions at reflecting interfaces, further affecting discriminant *P/S* phase amplitude ratios, generating artificially large surface waves due to propagation of trapped seismic energy in the crust (Xie and Lay, 1994; He et al., 2008; Rodgers et al., 2010). Furthermore, timing of depth phases (*pP, pS*) relative to direct phases from shallow sources in regions of dramatic surface topography can vary greatly based on azimuth and distance, strongly influencing source depth estimates, and in the case of nuclear test explosions, yield estimates. We present a method for calculating teleseismic 3D Green's functions (3D GFs) for seismic *P*-wave signals carrying the 3D effects of near-source topographic structure to teleseismic locations. This involves implementing the representation theorem (Aki and Richards, 2002) to predict far-field displacement using near-source 3D displacements and stresses. This method will be used to improve the accuracy of source location and depth by comparing synthetic *P* and *pP* waveforms from isotropic sources with observations, consequently providing more confident source depth (depth-of-burial) estimates on which nuclear explosion yield estimates are based. It will also be used to invert 3D GFs to create fault rupture models to compare to those created from 1D Green's functions (1D GFs) for a specific earthquake test case.

The effects of path heterogeneities on seismic wave propagation have long been studied, with many methodologies for reproducing those effects being developed. 1D modeling methods (e.g., Helmberger, 1968; Fuchs and Müller, 1971; Chapman, 1974; Chapman, 1976) focused on simulating wave propagation in a spherical Earth to study interference phases and their interaction with the free surface, layered media (Bache and Harkrider, 1976), velocity gradients approximated by finely layered media (Helmberger, 1968; Fuchs and Müller, 1971; Chapman, 1974; Chapman, 1976), and the development of body force equivalents for seismic dislocations (representation theorem) (Burridge and Knopoff, 1964; Bache and Harkrider, 1976; Regan and Harkrider, 1989; Regan and Harkrider, 1991; Aki and Richards, 2002). As computational technology progressed, finite difference and finite element methods were developed for 2D wave propagation (Ge et al., 2005; He et al., 2008; Wen and Helmberger, 1998; and Wu et al., 2010) with several methods for capturing and propagating waves to regional or teleseismic distances (Okamoto, 1994; Wen and Helmberger, 1988), or characterizing effects of heterogeneity on regional or teleseismic phases (Okamoto, 1993; Okamoto, 1994; He et al., 2008). Eventually, 3D synthetic waveform propagation could be calculated, utilizing 2D velocity models repeated in the 3rd dimension (known as 2.5D) to characterize out-of-plane scattering in a heterogeneous 3D volume (e.g., Takenaka and Kennett, 1996; Takenaka et al., 1996; Sun et al., 2008) and to calculate 3D Green's functions for more accurate source inversions (e.g., Okamoto, 1994; Miksat et al., 2008; Okamoto and Takenaka, 2009), as well as to isolate the 3D effects of topography on the seismic wavefield (Takenaka et al., 1996; Rodgers et al., 2010).

Several studies have previously implemented the representation theorem, to capture non-linear near-source effects (Taylor and App, 2010), or to capture near-source scattering effects (e.g., Regan and Harkrider, 1989; Regan and Harkrider, 1991; Vasconcelos et al., 2009; Stevens and Xu, 2010). Our method seeks to do this as well, by combining the 3D effects of detailed topography with the general method of Bache and Harkrider (1976), to produce 3D Green's functions with which to predict seismic *P*-waves at teleseismic receiver locations. The 3D near-source scattering effects of topography on the seismic wave field are calculated by WPP, a 2nd-order 3D finite difference wave propagation program developed at Lawrence Livermore National Laboratory (Appelo and Petersson, 2008; Nilsson et al., 2007; Petersson and Sjögreen, 2011), with scattering effects recorded in displacement and strain time series, which are used in the representation theorem implementation. WPP calculates 3D wave propagation in displacement on a Cartesian grid, allowing for realistic surface topography in simulations. I present the development of this method and basic test examples to demonstrate its functionality here. Specific applications will be explored in Chapters 3 and 4 of this thesis.

2.3 Theory

This 3D GF calculation begins by collecting displacement and strain time series output by the 3D FD WPP calculations. Since teleseismic 3D GFs are being calculated, takeoff angles from the source will be relatively steep, so the time series data are collected across a plane near the bottom boundary of the 3D computational domain (Fig. 2.1). Stress components acting on this plane are calculated from the strain data by employing Hooke's Law (e.g. Lay and Wallace, 1995):

$$\sigma_{zx} = 2\mu \frac{\partial u_x}{\partial z} \tag{1}$$

$$\sigma_{zy} = 2\mu \frac{\partial u_y}{\partial z} \tag{2}$$

$$\sigma_{zz} = \lambda \left(\frac{\partial u_x}{\partial x} + \frac{\partial u_y}{\partial y} + \frac{\partial u_z}{\partial z} \right) + 2\mu \frac{\partial u_z}{\partial z} \tag{3}$$

or generally:

$$\sigma_{ij} = \lambda \left(\varepsilon_{kk} \right) \delta_{ij} + 2\mu \, \varepsilon_{ij} \tag{4}$$

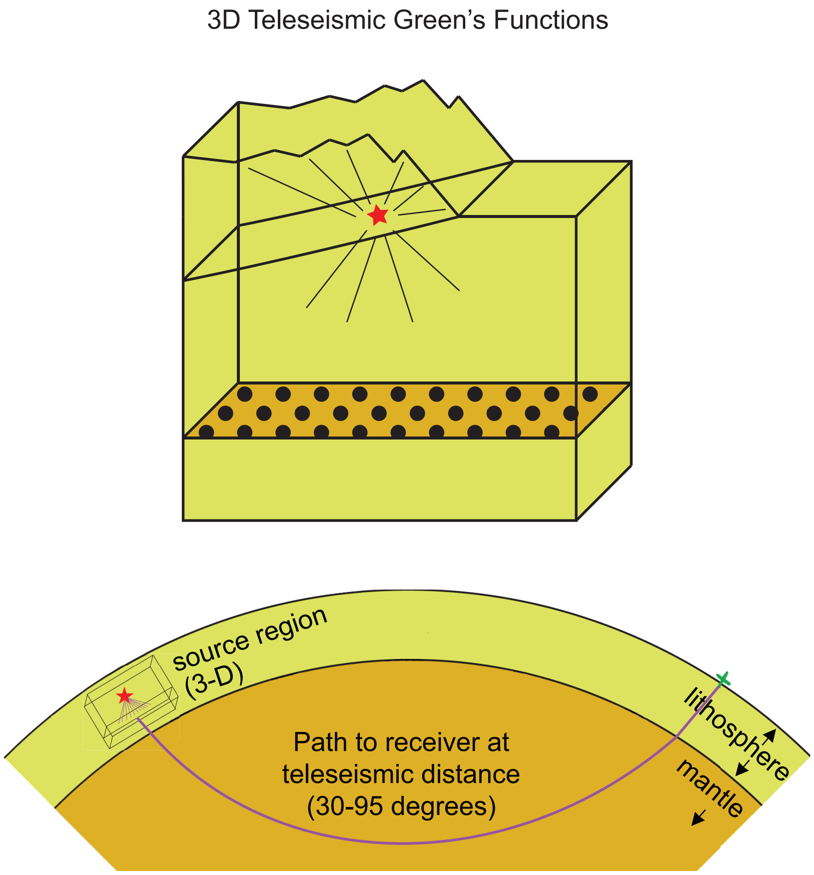

Figure 2.1 Schematic of the generation of 3D GFs, showing near-source 3D domain with the collection plane recording 3D scattering effects, and the 1D teleseismic path outside of the near-source domain.

The representation theorem is then used to calculate displacement at a specified teleseismic location resulting from contributions of stress and displacement components across the collection plane within the near-source 3D domain (Aki and Richards, 2002):

$$u_n(\boldsymbol{x},t) = \int_{-\infty}^{\infty} d\tau \iiint_V f_i(\boldsymbol{\xi},\tau)\, G_{in}(\boldsymbol{\xi},t-\tau;\boldsymbol{x},0) dV(\boldsymbol{\xi}) \\ + \int_{-\infty}^{\infty} d\tau \iint_S \{G_{in}(\boldsymbol{\xi},t-\tau;\boldsymbol{x},0)\, T_i(\boldsymbol{u}(\boldsymbol{\xi},\tau),\boldsymbol{n}) \\ - u_i(\boldsymbol{\xi},\tau)\, c_{ijkl}\, n_j\, G_{kn,l}(\boldsymbol{\xi},t-\tau;\boldsymbol{x},0)\}\ dS(\boldsymbol{\xi}) \tag{5}$$

As in *Regan and Harkrider* (1989), it is assumed that no body forces exist within the 3D volume V, and that the medium is isotropic, which results in the representation theorem for *P*-wave displacement being simplified to (Regan and Harkrider, 1989):

$$u_p(\boldsymbol{x},t) = \int_{-\infty}^{\infty} d\tau \iint_S \{G_{pi}\tau_{ij} + \lambda G_{pl,l}u_j + \mu\big(G_{pi,j} + G_{pj,i}\big)u_i\} n_j dS(\boldsymbol{\xi}) \tag{6}$$

In this case, stress and displacement components already contain the source-time function and any path effects from near-source propagation. The Green's function term in equation (6) contains information about the receiver function, radiation pattern to the teleseismic destination specified ($\boldsymbol{x}$), attenuation, and geometrical spreading. For our purposes, we ignore the receiver function, attenuation, and geometrical spreading effects outside the 3D near-source domain for now. Therefore, *G* symbolizes the radiation pattern coefficient of each point force (stress component) or force couple (displacement component) from the collection grid location to the teleseismic destination location. The resulting current implementation of the representation theorem then looks like this:

$$u_p(\boldsymbol{x},t) = \int_{-\infty}^{\infty} d\tau \left[H_{pi} \iint_S \{R_{pi}\tau_{ij} + \lambda R_{pl,l}u_j + \mu(R_{pi,j} + R_{pj,i})u_i\} n_j dS(\boldsymbol{\xi}) \right] \tag{7}$$

where a radiation pattern coefficient *R* is applied to each stress and displacement component based on the location of the teleseismic destination location relative to the near-source collection plane. The stress and displacement component contributions to teleseismic displacement are then summed to create a primitive Green's function (PGF), to which attenuation, geometrical spreading, and receiver function corrections (H_{pi}) are applied.

From the representation theorem (7), we see the integration of stress and displacement components is simply the summation of forces that result in a far-field *P*-wave displacement, as in the Haskell 1D source model (Lay and Wallace, 2005), for which each of the displacement traces recorded across the collection plane are treated as point sources across a fault, except our 'fault' is the 2-dimensional collection plane (see Fig. 2.1). *Lay and Wallace* (2005) show that the displacement for a far-field *P*-wave is the summation of each displacement point across a 1D fault, by the principle of linear superposition:

$$u_{ri} = R_i^P (\frac{1}{4\pi\rho\alpha^3})(\frac{\dot{M}_i}{r_i}) \tag{8}$$

and we know that moment rate, $\dot{M}$, is defined as:

$$\dot{M}_i = \mu A \dot{D}_i(t) \tag{9}$$

which, for a 1D fault is:

$$\dot{M}_i = \mu w dx \dot{D}_i(t) \tag{10}$$

where *w* is fault width, and *dx* is the length of each fault segment. We can then write the far-field displacement from rupture on a 1D fault as:

$$u_r(r,t) = \frac{\mu}{4\pi\rho\alpha^3} w \sum_{i=1}^{N} \frac{R_i^P \dot{D}_i}{r_i}(t - \Delta t_i) dx \tag{11}$$

where Δt_i is the travel time difference between fault point-source locations, *i* (Lay and Wallace, 2005).

Since we are considering teleseismic distances, r_i can be assumed to be constant; this is the geometrical spreading term that is applied once the PGF has been calculated. The radiation pattern term, R^P, is allowed to vary with position on the collecton plane. Summing displacements along the width of the collection plane as well as the length, and taking the limit of the sum as *dx* and *dy* approach 0, far-field *P*-wave displacement resulting from displacement along a 2-dimensional plane can be written as:

$$u_r(r,t) = \frac{\mu}{4\pi\rho\alpha^3}\frac{1}{r}\int_0^x \int_0^y R^P(x,y)\dot{D}\big(t - \Delta t(x,y)\big)dydx \tag{12}$$

Similarly, Stoke's solution demonstrates how to predict far-field *P*-wave displacement from single point forces (Lay and Wallace, 2005), which for our purposes are stress time series on the collection plane:

$$u_{ri}^P = \frac{1}{4\pi\rho\alpha^2}\gamma_i\gamma_j\frac{1}{r_i}F_i(t - \frac{r_i}{\alpha}) \tag{13}$$

where the $\frac{1}{r}$ term represents attenuation due to geometrical spreading, $\frac{r}{\alpha}$ is the time shift due to the propagation of the wave over distance *r*, and $\gamma_i\gamma_j$ are direction cosines that project the force onto the displacement raypath, which is the radiation pattern of a single point force. If we treat this similarly to the displacement case and sum the stress terms across the collection plane by principle of linear superposition, far-field *P*-wave displacement due to stresses acting on a plane can be calculated as:

$$u_r(r,t) = \frac{1}{4\pi\rho\alpha^2}\frac{1}{r}\int_0^x \int_0^y R^P(x,y)\tau\big(t - \Delta t(x,y)\big)dydx \tag{14}$$

where r_i is assumed to be constant, and the radiation pattern term and time shifts are dependent on the position on the plane.

To summarize, equations (12) and (14) are how displacement and stress components are treated in this implementation of the representation theorem. Since the attenuation term $\frac{1}{r}$ in each of these equations is ignored until later, the values resulting from applying (12) and (14) to each of the displacement and stress components on the collection plane are summed to calculate the PGF from the 3D near-source domain to a specific teleseismic location. After the 3D PGFs are calculated by use of the representation theorem, corrections for geometrical spreading, attenuation, and receiver function are applied assuming a 1D Earth structure for the remainder of the *P*-wave path to the receiver location. These corrections are calculated by using the 3D PGFs as impulse response / source-time function convolved input into a modified version of Kikuchi and Kanamori's method of calculating 1D Green's functions for teleseismic body waveform inversion (Kikuchi and Kanamori, 2003). In its original form, the Kikuchi and Kanamori method calculates 1D Green's functions by iteratively deconvolving source pulses from observed waveforms and then convolving the pulses with a source-time function and applying corrections for geometric spreading, attenuation, and receiver function.

2.4 Implementation

Implementation of the theory outlined previously begins with the calculation of the stress components acting on the collection plane near the bottom of the 3D FD volume at each gridpoint 'receiver' location along this plane (equations 1-3). Near-field receivers are spaced regularly across the collection plane, with at least 10 receivers per *P*-wavelength. Since the collection plane is located within the 3D domain such that it is removed from any heterogeneities or boundaries in seismic velocity or density, displacements and strains recorded across this plane should be smoothly varying. We maintain relatively dense sampling however, to ensure that any wave energy scattered by shallow structure is well resolved on the plane.

Once the three stress components acting on the collection plane have been determined for each gridpoint receiver location, the time series are prepared for subsequent calculations by being trimmed to within 1 second of the earliest predicted *P*-wave arrival time. The corners of the collection plane are then geographically oriented relative to the source in the 3D FD calculation, and the distance and azimuth from the collection plane corners to each teleseismic station location is calculated, assuming spherical Earth geometry. Using the distance and azimuth values for each corner, the distance and azimuth from each gridpoint receiver on the plane to each teleseismic station are determined using a bilinear interpolation algorithm. Takeoff angles and travel times from each gridpoint receiver to each teleseismic station are selected, based on distance, from tabulated values output from TauP (Crotwell et al., 1999), which relates distance to takeoff angles and travel times for specified phases, in this case, direct *P* waves.

The takeoff angle for each gridpoint to each of the teleseismic station locations is used to calculate an amplitude coefficient ranging in value from -1 to 1, which is applied to each data component, treating each gridpoint location as a mini-source, with a radiation pattern which projects the amplitude of each stress or displacement component at each location onto the teleseismic raypath. This radiation pattern amplitude coefficient is calculated using the takeoff angle and azimuth of the raypath from each near-source gridpoint location to each teleseismic station. Each stress component has the radiation pattern of a single point force (Lay and Wallace, 2005):

$$Rx = \sin\theta \cos\varphi \tag{15}$$

$$Ry = \sin\theta \sin\varphi \tag{16}$$

$$Rz = \cos\theta \tag{17}$$

Similarly, each displacement component is treated as a force couple point source (Kasahara, 1981; Shi and Ben-Zion, 2009):

$$Rxz = (\cos 2\theta \cos\varphi)/2 \tag{18}$$

$$Ryz = (\sin 2\theta \sin\varphi)/2 \tag{19}$$

$$Rzz = (\cos\theta)^2 \tag{20}$$

where θ is the takeoff angle and φ is the azimuth of the raypath from a specific gridpoint receiver to a teleseismic receiver location.

Next, the *P*-wave travel time from the gridpoint corresponding to the optical path of a direct *P*-wave from the seismic source to each teleseismic station is determined. Using TauP, the takeoff angle for a direct *P*-wave from the seismic source to each teleseismic station is determined, and the raypath is geometrically traced through the 3D volume to the collection plane depth. The closest gridpoint receiver to the piercepoint location of the raypath on the collection plane is the optical path reference point to each teleseismic station location. The difference between the direct *P*-wave travel time from each gridpoint location to the teleseismic station relative to that of the optical raypath (the minimum travel time path) is determined, and each time series is shifted by this amount just before integration.

Before integration, the time-derivative of each displacement time series is taken, since far-field displacement is a function of near-field velocity history. Each time series is then multiplied by the appropriate radiation pattern coefficient for each displacement component and location on the plane, and the time shift relative to the optical path is applied. Finally, each displacement component (now velocity) is integrated across the collection plane separately (see equation 12), resulting in three time series representing the summed contributions of the three displacement components (u_x, u_y, u_z) at each gridpoint location projected onto the raypath to the teleseismic station location. Each stress component is treated similarly: time shifts and radiation pattern coefficients appropriate for each grid location are applied, and the resulting time series are integrated across the plane, as shown in equation (14).

Finally, the six time series resulting from the integration of each of the three displacement components and three stress components are added together to form the primitive Green's function (PGF) for a single teleseismic station location. Once a PGF has been calculated for each teleseismic station, the PGF time series is windowed, resampled, and padded with zeros after the sP phase arrival, in preparation for input into a version of Kikuchi and Kanamori's teleseismic inversion code (Kikuchi and Kanamori, 2003) modified to accept the 3D PGFs as input that already incorporates the near-source impulse response / source-time function convolution, so assuming a 1D Earth structure for the reminder of the path to the teleseismic receiver, the GFs calculated from the modified Kikuchi and Kanamori method only apply amplitude corrections to account for attenuation, geometrical spreading, and the receiver function beneath the teleseismic station. The result is a 3D Green's function.

2.5 Testing and Benchmarks

The first verification of this method checks that the seismic energy incident on the collection plane is well-behaved and signs change appropriately with respect to the coordinate system on the plane. Figure 2.2 is a snapshot from a movie of each displacement and stress component time series mapped across the collection plane, so the waves incident on the plane can be seen and tracked through time. The stress component calculations are then checked by calculating them from finite-differencing of the displacement components across the collection plane, and then from the strain components output from WPP (eqns 1-3). The results are indistinguishable between the two methods, so we calculate stress components from the strain time series output from WPP.

Next, the radiation patterns for all single force and force-couple point source types are plotted onto a sphere to ensure the coefficient values are between -1 and 1, and they are correctly oriented with respect to the coordinate system on the collection plane (Fig. 2.3).

PGFs are then calculated for an isotropic source to theoretical teleseismic locations at a constant distance (36 degrees) from the source, at 30-degree azimuthal increments. This design tests the signs of the integrated displacement and stress components, as well as the amplitudes and timing of the PGF traces (Fig. 2.4a). The results of this test give an estimate of errors resulting from the geometry of the collection

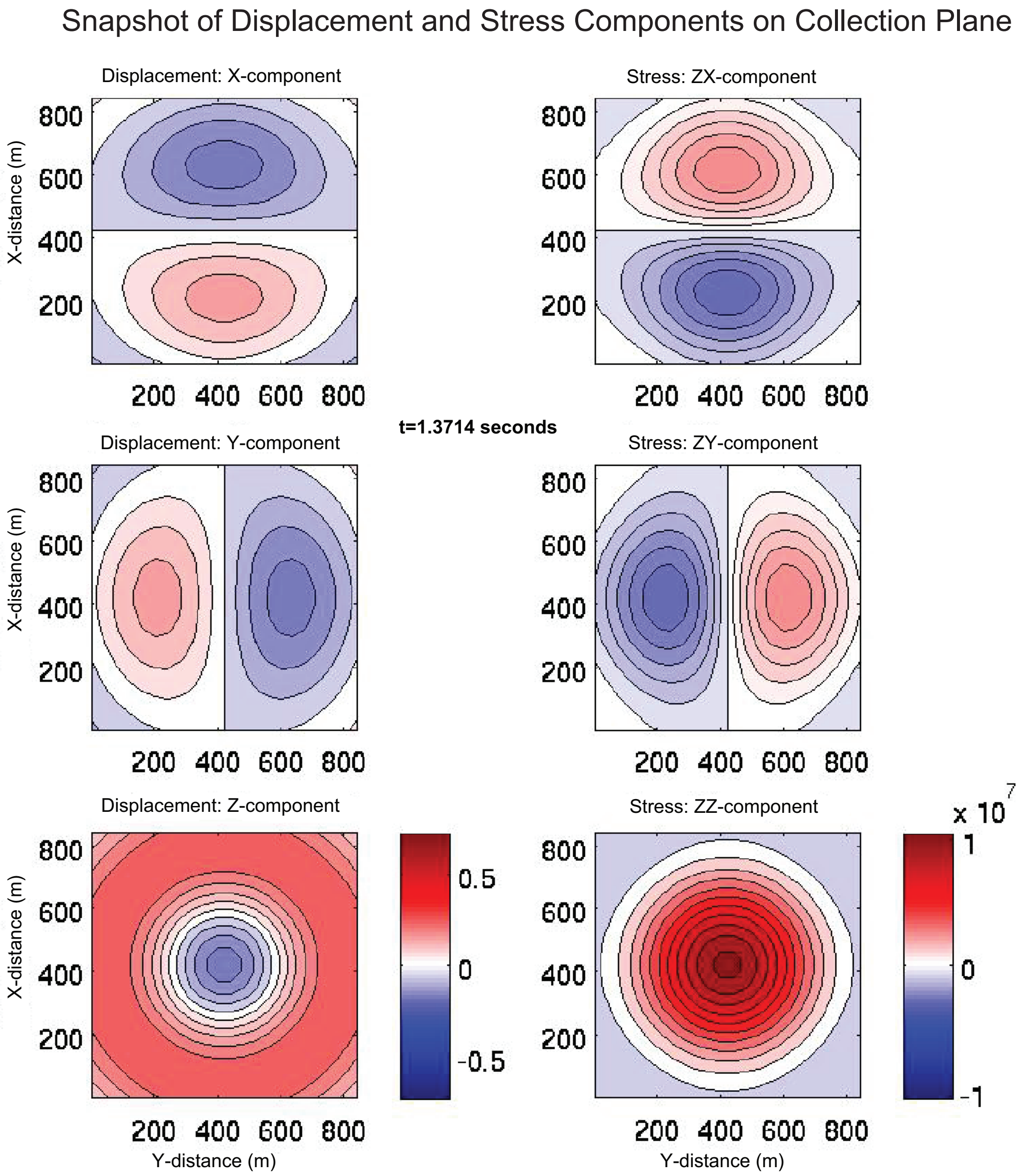

Figure 2.2 Snapshot of each of the 6 time series at a single time sample, mapped across the collection plane to show incidence and expansion of the wavefronts across the plane in time.

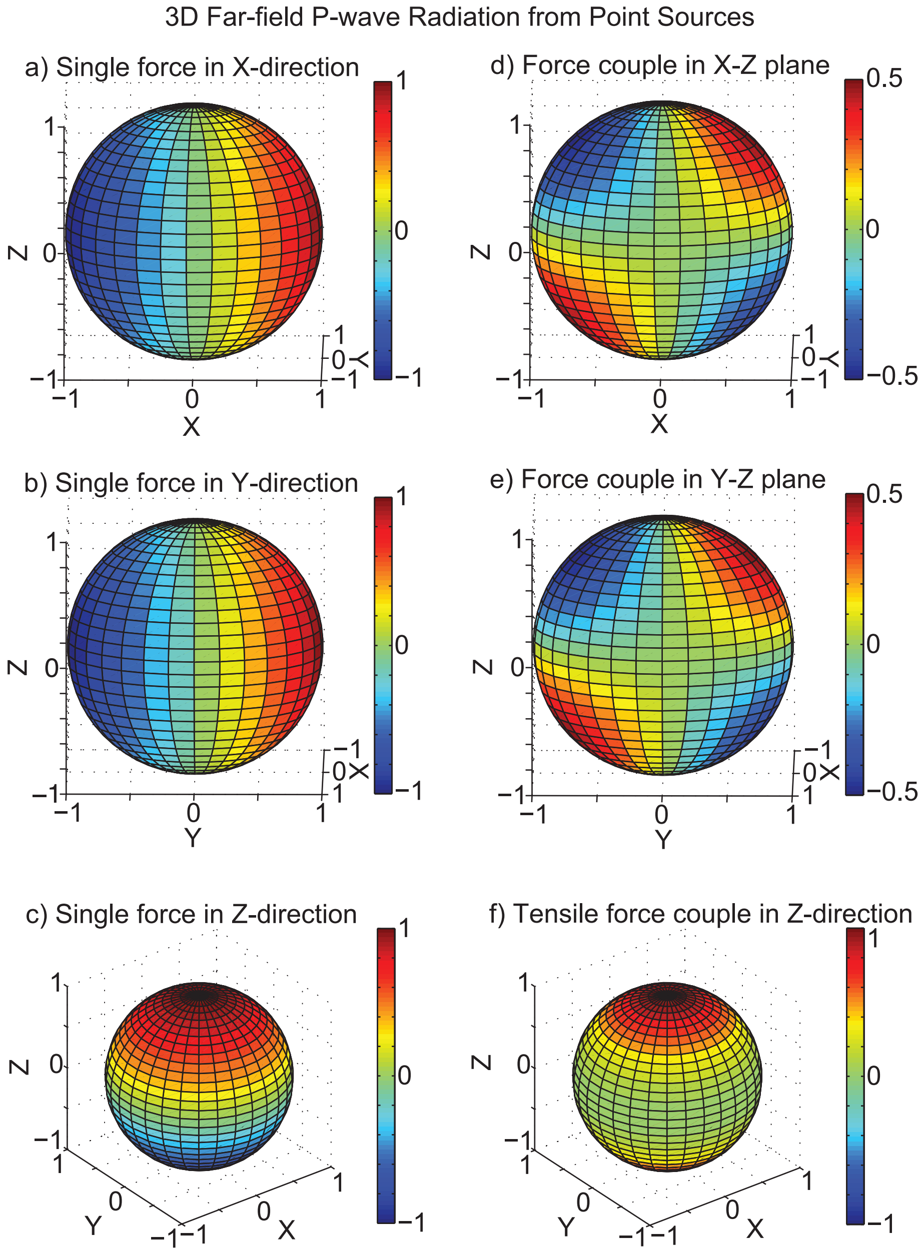

Figure 2.3 Radiation patterns for all single-force (left) and force-couple (right) point sources corresponding to the displacement and stress components acting on the collection plane.

plane, as well as spatial and temporal discretization. The errors in this test should represent the upper bound, as the distance to the theoretical teleseismic locations require the most shallow takeoff angle from the source, so the optical raypath will be located closest to the bounds of the collection plane for this case than any other distances considered. Therefore, possible errors due to imbalanced wave field sampling due to the finiteness of the integration plane will be most evident in this test. The *P*-wave timing and amplitudes from an isotropic source are shown in Figure 2.4. Variations in timing are as much as +/- 0.022 seconds. The relative timing of the depth phases is consistent however, and agrees with timing predictions based on source depth and location of raypath piercepoint relative to the source. Absolute timing of the *P*-wave is less important, as the time windows will be trimmed to begin at *P*-wave onset for using the modified Kikuchi and Kanamori method for applying amplitude corrections for the rest of the raypath outside the near-source 3D domain. Large variations in direct *P* arrival times would indicate a problem in estimating the optical raypath location and / or time shifting relative to the optical travel time. Variations in amplitude are within +/- 3.24% about the mean *P*-wave amplitude. These errors are greatest for PGFs calculated for azimuths 0, 90, 180, and 270 (Fig. 2.4b), which indicates that the variations in amplitude are likely due to the geometry of a cartesian coordinate system on the collection plane. as these azimuths have amplitudes that diverge the most from those of PGFs calculated for other azimuths (Fig. 2.4c: variations are within +/- 1.47% of the mean for this subset), likely because the distance from one grid point to another, and therefore from the source to the lateral edges of the FD domain is shortest in these directions (the x-axis of the 3D domain is aligned with 0-degrees azimuth).

Finally, 3D GFs are calculated for a strike-slip source to theoretical stations at distances of 36, 54, and 73 degrees at regular azimuthal intervals, and the results are compared to 1D GFs calculated for the same source type and theoretical teleseismic stations. Figure 2.5 shows this comparison for two of the GFs at 36 degrees distance (black is 1D, red is 3D). The 1D and 3D GFs agree well, but there is a mis-match in absolute amplitudes, so the 3DGF *P*-wave amplitudes are normalized to that of corresponding 1DGFs. The relative amplitudes of the 3DGFs are correct, as seen in Figure 2.5.

2.6 Conclusion

A method for calculating 3D GFs is developed by implementation of the representation theorem to sum forces resulting from stresses and displacements acting on a plane within a 3D volume, which contribute to the displacement observed at a specific teleseismic location. This method captures the 3D scattering effects of any near-source boundaries or surface topography, as well as seismic velocity or density heterogeneities due to geologic structure near the seismic source, and incorporates them into the resulting Green's function.

Testing this method for an isotropic seismic source reveals that after integration to calculate the PGF to specific destinations at regular azimuthal intervals, *P*-wave onset varies by less than +/- 0.022 seconds, and amplitude varies within +/- 3.24% about the mean value. Final 3D GFs resulting from applying amplitude corrections for geometrical spreading, attenuation, and receiver functions through the 1D Earth outside the near-source 3D domain agree well with 1D GFs calculated from Kikuchi and Kanamori for teleseismic source inversion. Applications of this method to two different seismological problems is explored in the following chapters.

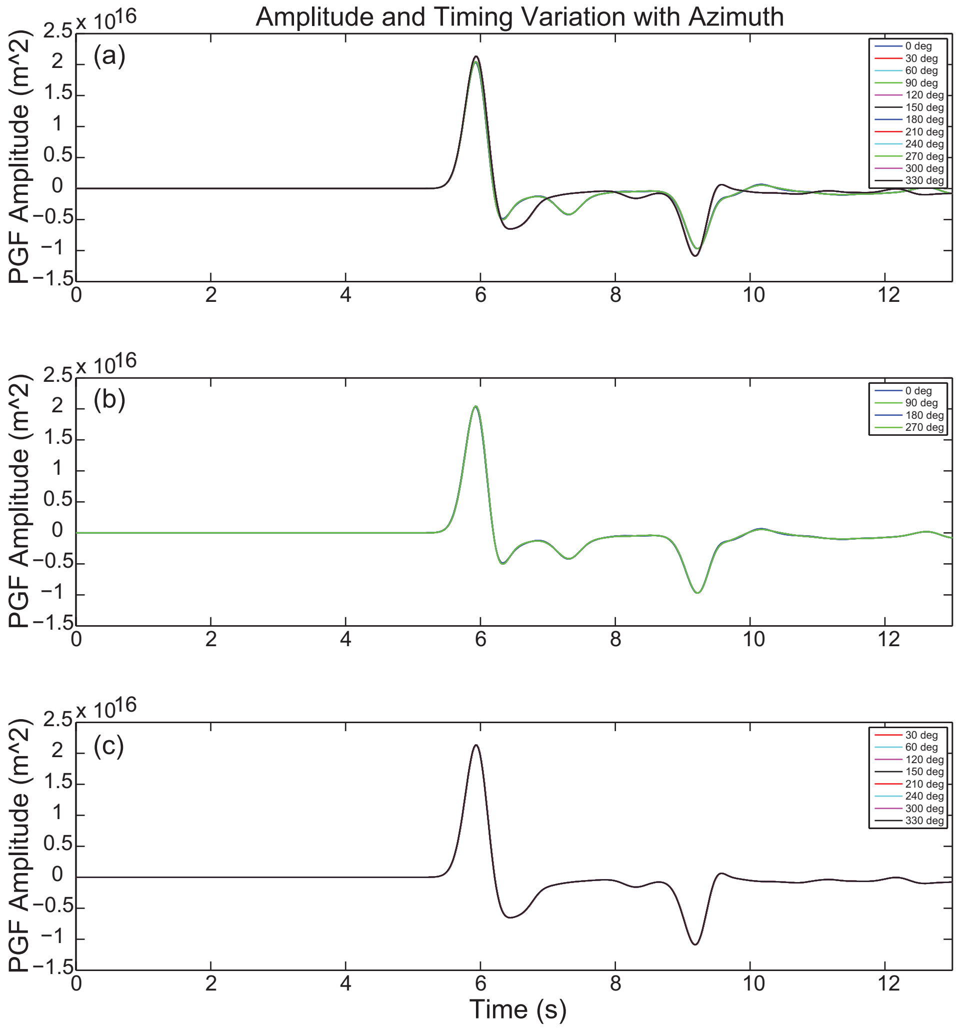

Figure 2.4 PGFs calculated for an isotropic source to a ring of theoretical teleseismic stations 36 degrees away, at 30-degree azimuthal intervals. (a) Stacked PGFs of all 12 stations; (b) Stacked PGFs of stations at 0, 90, 180, and 270 degrees azimuth; (c) Stacked PGFs of the rest of the stations not at azimuthal multiples of 90 degrees.

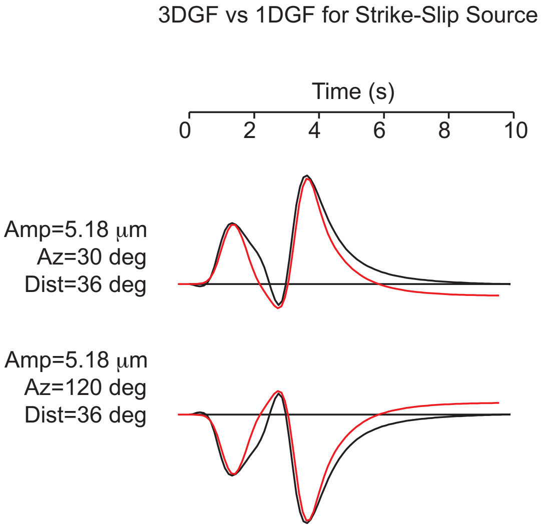

Figure 2.5 Sample comparison of 3D GF (red) to 1D GF (black) from a 5-km deep strike-slip source to teleseismic stations at 36 degrees distance.

2.7 References

Aki, K. and P.G. Richards (2002), *Quantitative Seismology*, 2nd ed., Univ. Sci., Sausalito, California.

Appelo, D. and N.A. Petersson (2008), A stable finite difference method for the elastic wave equation on complex geomtries with free surfaces, *Commun. Comp. Phys.*, **5**, 84-107.

Avants, M., T. Lay, X-B. Xie, and X. Yang (2011), Effects of 2D random velocity heterogeneities in the mantle lid and Moho topography on *Pn*, geometric spreading, *Bull. Seismol. Soc. Am.*, **101**, 126-140.

Bache, T.C. and D.G. Harkrider (1976), The body waves due to a general seismic source in a layered Earth model: 1. Formulation of the theory, *Bull. Seismol. Soc. Am.*, **66**, 1805-1819.

Burridge, R. and L. Knopoff (1964), Body force equivalents for seismic dislocations, *Bull. Seismol. Soc. Am.*, **54**, 1875-1888.

Chapman, C.H. (1974), Generalized ray theory for an inhomogeneous medium, *Geophys. J. R. Astr. Soc.*, **36**, 673-704.

Chapman, C.H. (1976), Exact and approximate generalized ray theory in vertically inhomogeneous media, *Geophys. J. R. Astr. Soc.*, **46**, 201-233.

Crotwell, H.P., T.J. Owens, and J. Ritsema (1999), The TauP Toolkit: Flexible seismic travel-time and ray-path utilities, *Seismol. Res. Lett.*, **70**, 154-160.

Fuchs, K. and G. Müller (1971), Computation of synthetic seismograms with the reflectivity method and comparison with observations, *Geophys. J. Int.*, **23**, 417-433.

Ge, Z., L-Y. Fu, and R-S. Wu (2005), *P-SV* Wave-field connection technique for regional wave propagation simulation, *Bull. Seismol. Soc. Am.*, **95**, 1375-1386.

He, Y., X-B. Xie, and T. Lay (2008), Explosion-source energy partitioning and *Lg*-wave excitation: contributions of free-surface scattering, *Bull. Seismol. Soc. Am.*, **98**, 778-792.

Helmberger, D.V. (1968), The crust-mantle transition in the Bering Sea, *Bull. Seismol. Soc. Am.*, **58**, 179-214.

Kasahara, K. (1981), *Earthquake Mechanics*, Cambridge University Press, New York, New York.

Kikuchi, M. and H. Kanamori (2003), Note on teleseismic body-wave inversion program, *Earthquake Research Institute, Tokyo University, Japan*, Online at http://www.eri.u-tokyo.ac.jp/ETAL/KIKUCHI

Lay, T. and T.C. Wallace (2005), *Modern Global Seismology*, Academic Press, San Diego, California.

McLaughlin, K.L., T.G. Barker, S.M. Day, B. Shkoller, and J.L. Stevens (1992), Effects of subduction zone structure on explosion-generated Rayleigh waves: 3-D numerical simulations, *Geophys. J. Int.*, **111**, 291-308.

Miksat, J. T.M. Müller, and F. Wenzel (2008), Simulating three-dimensional seismograms in 2.5-dimensional structures by combining two-dimensional finite difference modelling and ray tracing, *Geophys. J. Int.*, **174**, 309-315.

Nilsson, S., N.A. Petersson, B. Sjögreen, and H-O. Kreiss (2007), Stable difference approximations for the elastic wave equation in second order formultion, *SIAM J. Numer. Anal.*, **45**, 1902-1936.

Okamoto, T. (1993), Effects of sedimentary structure and bathymetry near the source on teleseismic *P* waveforms from shallow subduction zone earthquakes, *Geophys. J. Int.*, **112**, 471-480.

Okamoto, T. (1994), Teleseismic synthetics obtained from 3-D calculations in 2-D media, *Geophys. J. Int.*, **118**, 613-622.

Okamoto, T. and H. Takenaka (2009), Waveform inversion for slip distribution of the 2006 Java tsunami earthquake by using 2.5D finite-difference Green's function, *Earth Planets Space*, **61**, e17-e20.

Petersson, N.A. and B. Sjögreen (2011), User's guide to WPP version 2.1.5, *Tech. Rep. LLNL-SM-487431*, Lawrence Livermore Natl. Lab. Livermore, California.

Pitarka, A., D.V. Helmberger, and S. Ni (2007), Analysis and simulation of three-dimensional scattering due to heterogeneous crustal structure and surface topography on regional phases; magnitude and discrimination, *Proceedings of the 29th Seismic Research Review: Ground-Based Nuclear Explosion Monitoring Technologies*, FA8718-07-C-0003, Vol. 1, 205-213.

Regan, J. and D.G. Harkrider (1989), Seismic representation theorem coupling: synthetic SH mode sum seismograms for non-homogeneous paths, *Geophys. J. Int.*, **98**, 429-446.

Regan, J. and D.G. Harkrider (1991), Seismic representation theorem coupling: P-SV mode sum seismograms for non-homogeneous paths, *Geophys. J. Int.*, **106**, 587-609.

Rodgers, A.J., N.A. Petersson, and B. Sjögreen (2010), Simulation of topographic effects on seismic waves from shallow explosions near the North Korean nuclear test site with emphasis on shear wave generation, *J. Geophys. Res.*, **115**, B11309, doi:10.1029/2010JB007707.

Shi, Z. and Y. Ben-Zion (2009), Seismic radiation from tensile and hear point dislocations between similar and dissimilar solids, *Geophys. J. Int.*, **179**, 444-458.

Stead, R.J. and D.V. Helmberger (1988), Numerical-analytical interfaceing in two-dimensions with applications to modeling NTS seismograms, *PAGEOPH*, **128**, 157-193.

Stevens, J.L. and H. Xu (2010), Wave propagation from complex 3D sources using the representation theorem, *2010 Monitoring Research Review: Ground-Based Nuclear Explosion Monitoring Technologies*, FA8718-08-C-0010, Vol. 1, 519-528.

Sun, W. L-Y. Fu, and R-S. Wu (2008), 2.5D *SH* wave propagation in heterogeneous crustal waveguides using the phase screen method, *Bull. Seismol. Soc. Am.*, **98**, 2391-2401.

Takenaka, H. and B.L.N. Kennett (1996), A 2.5-D time-domain elastodynamic equation for plane-wave incidence, *Geophys. J. Int.*, **125**, F5-F9.

Takenaka, H., B.L.N. Kennett, and H. Fujiwara (1996), Effect of 2-D topography on the 3-D seismic wavefield using a 2.5-D discrete wavenumber-boundary integral equation method, *Geophys. J. Int.*, **124**, 741-755.

Taylor, S.R., and F.N. App (2010), Representation theorem coupling of numerical and wave propagation codes for the generation of synthetic seismograms, *Los Alamos National Laboratory, NM*, LAUR-94-2194.

Vasconcelos, I., R. Snieder, and H. Douma (2009), Representation theorems and Green's function retrieval for scattering in acoustic media, *Phys. Rev. E*, **80**, 036605.

Wen, L. and D.V. Helmberger (1998), A two-dimensional *P-SV* hybrid method and its application to modeling localized structures near the core-mantle boundary, *J. Geophys. Res.*, **103**, 17901-17918.

Wu, R-S., S. Jin, and X-B. Xie (2000), Seismic wave propagation and scattering in heterogeneous crustal waveguides using screen propagators: I SH waves, *Bull. Seismol. Soc. Am.*, **90**, 401-413.

Xie, X-B. and T. Lay (1994), The excitation of *Lg* waves by explosions: A finite-difference investigation, *Bull. Seismol. Soc. Am.*, **84**, 324-342.

Chapter 3

Using 3D teleseismic *P*-wave Green's functions to determine source characteristics of North Korean nuclear test explosions

Megan Avants[1], Thorne Lay[1], and Arthur Rodgers[2]

[1] *University of California Santa Cruz, Department of Earth and Planetary Sciences*
[2] *Lawrence Livermore National Laboratory, Geophysical Monitoring Program*

3.1 Abstract

We test the use of teleseismic *P*-wave Green's functions calculated from the application of the representation theorem to constrain source location and depth of the three North Korean nuclear test explosions. We employ realistic topographic models of the region to capture the scattering effects of the free surface on the reflected *pP* phase. We measure the relative amplitudes of *P* and *pP* to compare the effects of source depth and topography on various source locations in the test site region and compare synthetic *P* and *pP* amplitudes from the Green's functions to those recorded by teleseismic arrays around the world. Results indicate a source depth for the 2006 event of 478 m. Source depths for the 2009 and 2013 events are 434 m and 641 m, respectively, demonstrating the potential of detailed waveform modeling within the topographic heterogeneity for resolving absolute emplacement position.

3.2 Introduction

Recordings of seismic waves are used to locate, identify, and estimate the size (yield) of nuclear explosions. Near-source heterogeneities such as boundary or surface topography imprint the seismic wave field by refracting and reflecting waves at boundaries, with the potential of severely disrupting ray paths through multiple reflections (scattering) (e.g., Stead and Helmberger, 1988; He et al., 2008; Rodgers et al., 2010; Avants et al., 2011). These effects on the seismic signal persist throughout its path and can obscure source characteristics such as location, depth, source type, and magnitude in the recorded signal. The trio of underground nuclear tests conducted in North Korea occurred in a region of dramatic surface topography. This location, combined with a dearth of local seismic data and historic observational data with which to characterize path effects, demonstrate the challenges in accurately determining source characteristics of these events. The timing and relative amplitude of teleseismic *P* and *pP*, which are sensitive to source depth and have a limited sensitivity to topographic scattering, may provide useful constraints on source depth, and possibly source location, within the test site region. Yield estimates, based on source depth determined from seismic observations, are a fundamental factor in determining international response to a nuclear test, so it is difficult to overstate the importance of accurate event locations for nuclear monitoring applications. With this powerful motivation, we estimate refined locations of the 2006, 2009, and 2013 North Korea nuclear tests, by applying the method of calculating 3D Green's functions for teleseismic *P*-waves developed in Chapter 2.

Studies to date have relied on travel times for locating these explosion events relative to each other, given the challenges involved in determining accurate absolute locations in this source region: no available local data, limited regional data coverage and intensely path-dependent scattering effects in regional phases and surface waves, and relatively small source magnitudes limiting usefulness of teleseismic signals. The 2006 event location from Murphy et al. (2010), 41.2867 N / 129.0902 E, was determined by using topographic information to limit possible source locations from a relative location computation for the 2006 and 2009 events to those with adequate overburden for the reported yields. The location of the 2009 event (41.2925 N/ 129.0657 E), 2.5 km west-northwest of the 2006 location, was determined using arrival time measurements at stations common to both the 2006 and 2009 events. Other relative location techniques explored by the authors produced similar results. Likewise, Wen and Long (2010) performed a relative location of the 2006 and 2009 events using Pn arrival time differences, locating the 2009 event approximately 2.35 km northwest of the 2006 event, which is in good agreement with Murphy et al. (2010).

Using broadband *P*-wave spectral ratios of the two events at common regional stations, Murphy et al. (2010) estimated the depth of the 2006 event to be 200 m (100-300 m) and the 2009 event to be 550 m (350-750 m), which is in agreement with Zhang and Wen's (2013) 2009 depth of burial estimate of 610 m. Depths are measured as the meters of overburden at the source location relative to the elevations of tunnel entrances observed from satellite images. Yield estimates for the 2006 and 2009 events are more variable, with Murphy et al. (2010) using Pn spectral ratio analysis to estimate the yield of the 2006 event to be 0.9 kt, and the 2009 event to be approximately 5 times larger, at 4.6 kt (yield errors +/- 30%, Murphy et al. (2011)). Zhang and Wen (2013) estimated the yield of the 2009 event to be 7.0 +/- 1.9 kt, which is significantly larger than the upper bound of 5.98 kt estimated from Murphy et al. (2010), considering the close agreement of the depth estimates for this event. This yield estimate, based on Lg amplitude ratios, is likely biased by larger-than-normal Lg amplitudes due to topographic scattering trapping seismic energy into the surface wave phases (Murphy et al., 2010; Rodgers et al., 2010).

Table 3.1a: DPRK Source Grid Search Locations for 10/09/2006 Event (200 m grid spacing)

Grid Location (m,n)	Latitude (N)	Longitude (E)	Surface Elevation (m) *	Source Depth (m)
2006(1,1)	41.2892	129.1059	1757	384
2006(1,2)	41.2892	129.1083	1747	374
2006(1,3)	41.2892	129.1107	1851	478
2006(2,1)	41.2874	129.1059	1649	276
2006(2,2)**	41.2874	129.1083	1723	350
2006(2,3)	41.2874	129.1107	1808	435
2006(3,1)	41.2856	129.1059	1607	234
2006(3,2)	41.2856	129.1083	1709	336
2006(3,3)	41.2856	129.1107	1743	370
Estimated Tunnel Access:	**41.2796**	**129.0988**	**1373**	

Table 3.1b: DPRK Source Grid Search Locations for 05/25/2009 and 02/12/2013 Events (300 m grid spacing)

Grid Location (m,n)	Latitude (N)	Longitude (E)	Surface Elevation (m) *	Source Depth (m)
2009-13(1,1)	41.2939	129.0745	1950	572
2009-13(1,2)	41.2939	129.0781	1991	613
2009-13(1,3)**	41.2939	129.0817	2019	641
2009-13(1,4)	41.2939	129.0853	1954	576
2009-13(2,1)***	41.2912	129.0745	1799	421
2009-13(2,2)***	41.2912	129.0781	1815	437
2009-13(2,3)	41.2912	129.0817	1895	517
2009-13(2,4)	41.2912	129.0853	1812	434
2009-13(3,1)	41.2885	129.0745	1673	295
2009-13(3,2)	41.2885	129.0781	1690	312
2009-13(3,3)	41.2885	129.0817	1787	409
2009-13(3,4)	41.2885	129.0853	1693	315
2009-13(4,1)	41.2858	129.0745	1612	234
2009-13(4,2)	41.2858	129.0781	1588	210
2009-13(4,3)	41.2858	129.0817	1663	285
2009-13(4,4)	41.2858	129.0853	1622	244
Estimated Tunnel Access:	**41.2799**	**129.0857**	**1378**	

* Surface Elevation values obtained from topocoding.com

** Lat/Lon is that from Wen and Long (2010)

*** Closest grid locations to Zhang and Wen (2013) event location: 41.2908 N / 129.0763 E

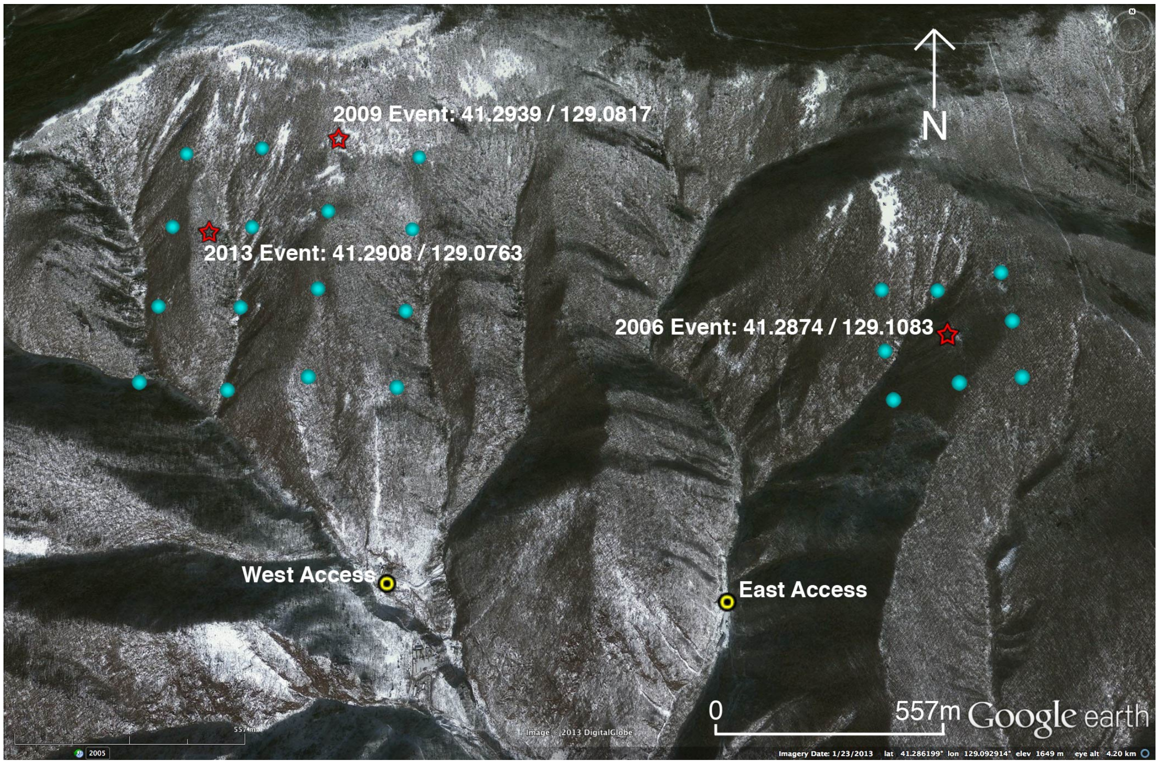

Figure 3.1 Google Earth image (image date: 01/23/2013) of North Korea nuclear test site with source locations (Wen and Long, 2010; Zhang and Wen, 2013) and grid search locations.

Zhang and Wen (2013) located the most recent (2013) nuclear test explosion relative to the 2009 event using the same method as Wen and Long (2010). The resulting location is 41.2908 / 129.0763, which is approximately 570 m west-southwest of the 2009 event location of Wen and Long (2010). The depth-of-burial estimate for the 2013 event, based on satellite imagery, is 430 m (Zhang and Wen, 2013). The estimated yield of this event based on Lg amplitude ratios is 12.2 +/- 3.8 kt, which should be considered an upper bound estimate due to enhanced Lg amplitudes resulting from intense topographic scattering in the source region (Murphy et al., 2010; Rodgers et al., 2010).

Stephens and Xu (2010) implemented the representation theorem for far-field body waves, performing calculations for explosive sources at various depths in the presence of topographic heterogeneity, as well as elastic and non-elastic velocity heterogeneities. This study focused on using the representation theorem to capture the seismic signature of nonlinear source phenomenon, whereas ours seeks to isolate the purely elastic effects of topography on the wave field. Keeping in mind the strong scattering effects of the dramatic topography in the DPRK nuclear test region, we apply our implementation of the representation theorem described in Chapter 2 to compare relative amplitudes of teleseismic *P*-waves for a range of possible source locations in an attempt to further constrain the depth estimates for each explosion, as well as to perhaps refine their respective locations using the limited effects of topographic scattering on the *pP* phase as a tool to improve source location. We use the locations of the 2006 and 2009 events from Wen and Long (2010) as the basis for our source location grid search, which also includes the 2013 event location from Zhang and Wen (2013) (Table 3.1, Figure 3.1).

3.3 Methods

We begin by first defining our grid search locations for each of the three sources in the test site region. We used Google Earth to locate the 2006 and 2009 explosion locations from Wen and Long (2010), and to locate the tunnel entrance locations, and then defined a 3x3 grid surrounding the 2006 location, with 200 m spacing. For the 2009 and 2013 locations, we defined a single 4x4 grid with 300 m spacing that surrounds both published locations (Figure 3.1, Table 3.1). The source depth at each of these locations is determined relative to the elevation of the tunnel entrances, in the same way as Murphy et al. (2010) and Zhang and Wen (2013).

Next we obtained recordings of these events from teleseismic arrays so we can stack signals to enhance SNR for all events, but especially the 2006 explosion, which has the smallest magnitude and is particularly difficult to detect above the noise level in teleseismic recordings. The array locations are averaged to a single location (Table 3.2), to which 3D Green's functions will be calculated from each source grid location. The instrument responses are removed from each trace, and a light high-pass filter (0.3-0.5 Hz) is applied to stabilize the baseline and pick the *P* arrival on each trace. All stations in each array are aligned on *P*, normalized to *P* amplitude, and stacked to create a single 'average' trace for that array. Array stacks for each event are shown in Figures 3.2-3.4. Synthetic PGFs, filtered in the same way as the corresponding observed traces, are shown in Appendix A.

Based on the range of source depths present in the grid locations, we define a 3D volume with a collection grid deep enough to separate *S* in time from the *P*-phases (*P*, *pP*), and with lateral dimensions large enough to capture the *pP* piercepoint to a station at a minimum distance of 35 degrees from the source (all takeoff angles considered will be less than that for a raypath traveling only 35 degrees), and at a distance greater than 5 km from the edge of the collection grid in all directions. With these considerations in mind, we define a volume with dimensions 30,000 m x 30,000 m x 18,000 m with a collection grid at depth 15,000 m for all source locations synthesized in this study.

Topography for the test site region was obtained from colleagues at Lawrence Livermore National Laboratory (LLNL), with resolution of 90 m. WPP, the 3D finite difference wave propagation program developed by LLNL (Petersson and Sjögreen, 2011), fits a polynomial to the topography, effectively smoothing it based on the frequency resolution of the seismic waves being calculated. This topography grid file (lat / lon / elevation) is specified in the input to WPP, and source depth is specified as depth below the topographic surface.

Table 3.2: Average Array Locations

Abbreviated Name	Location	Average Latitude (N)	Average Longitude (E)	Distance from DPRK source region (degrees)	Azimuth from DPRK to array (degrees)
ASAR	Alice Spring, Australia	-23.6668	133.9394	65.1109	175
BUR	Bucovina Array, Romania	47.6233	25.2167	68.5144	315
NVAR	NVAR Array, Mina, NV, USA	38.4286	-118.3043	79.4101	47
PSAR	Pilbara Array, Australia	-21.5717	119.8483	63.4417	190
WRA	Warramunga Array, Australia	-19.9428	134.3523	61.4579	174
YKA	Yellowknife Array, NT, Canada	62.4994	-114.6783	64.4094	27

An explosive source with seismic moment 3.55e15 Nm is synthesized in WPP for each of the grid locations in the 2006 source grid region, and an explosive source with seismic moment 1.41e16 Nm is synthesized for each grid location in the 2009 and 2013 source grid region. A separate set of synthetic events is not calculated for the 2013 event, because we are only concerned with the relative amplitude of the first arrivals and not their absolute amplitudes. The synthetic waveforms have a fundamental frequency of 2 Hz, and a maximum frequency of 5 Hz, an appropriate frequency band to match that of the stacked teleseismic *P* wave array data. The volume is a half-space, with constant seismic velocity and density ($V_p = 5570$ m/s; $V_s = 3360$ m/s; $\rho = 2650$ kg/m^3).

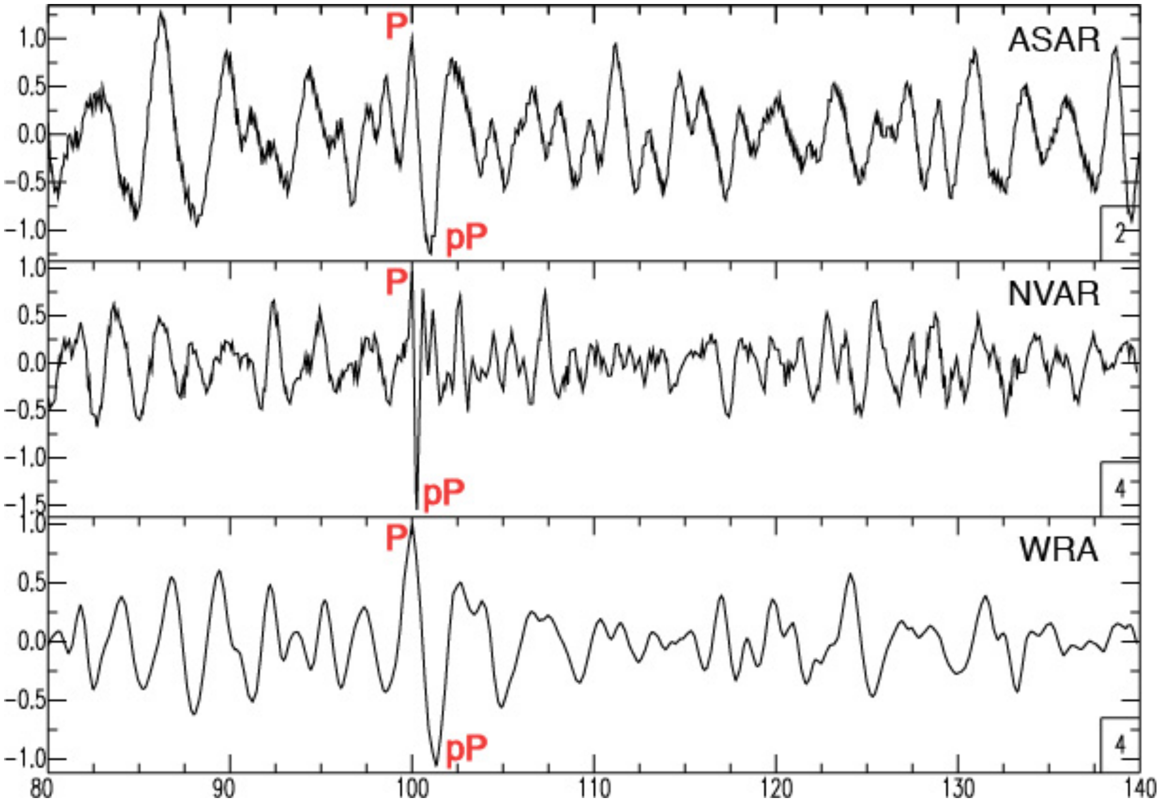

Figure 3.2 Stacked traces from arrays recording the 10/09/2006 event. Traces are aligned on *P* at 100 s, normalized to *P* amplitude, filtered with a highpass filter (ASAR: 0.5 Hz, NVAR: 0.5 Hz, WRA: 0.4 Hz), and stacked.

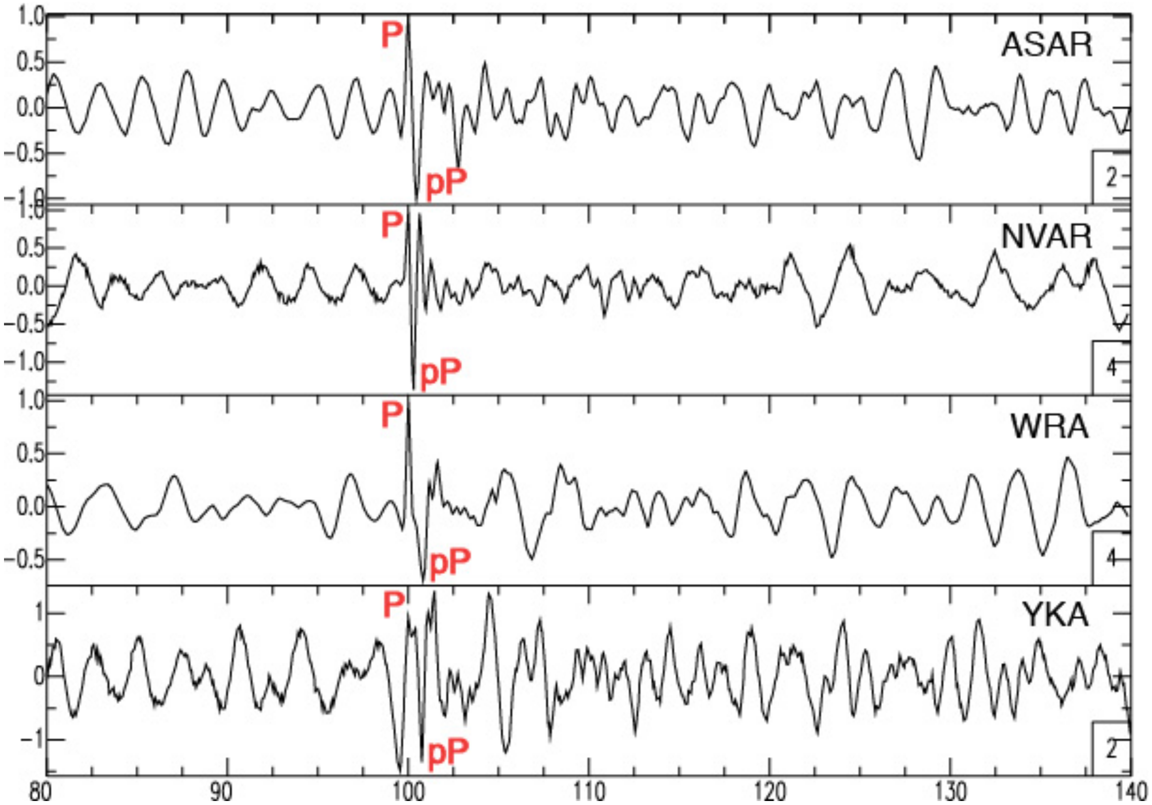

Figure 3.3 Stacked traces from arrays recording the 05/25/2009 event. Traces are aligned on *P* at 100 s, normalized to *P* amplitude, filtered with a highpass filter (ASAR: 0.5 Hz, NVAR: 0.3 Hz, WRA: 0.4 Hz, YKA: 0.5 Hz), and stacked.

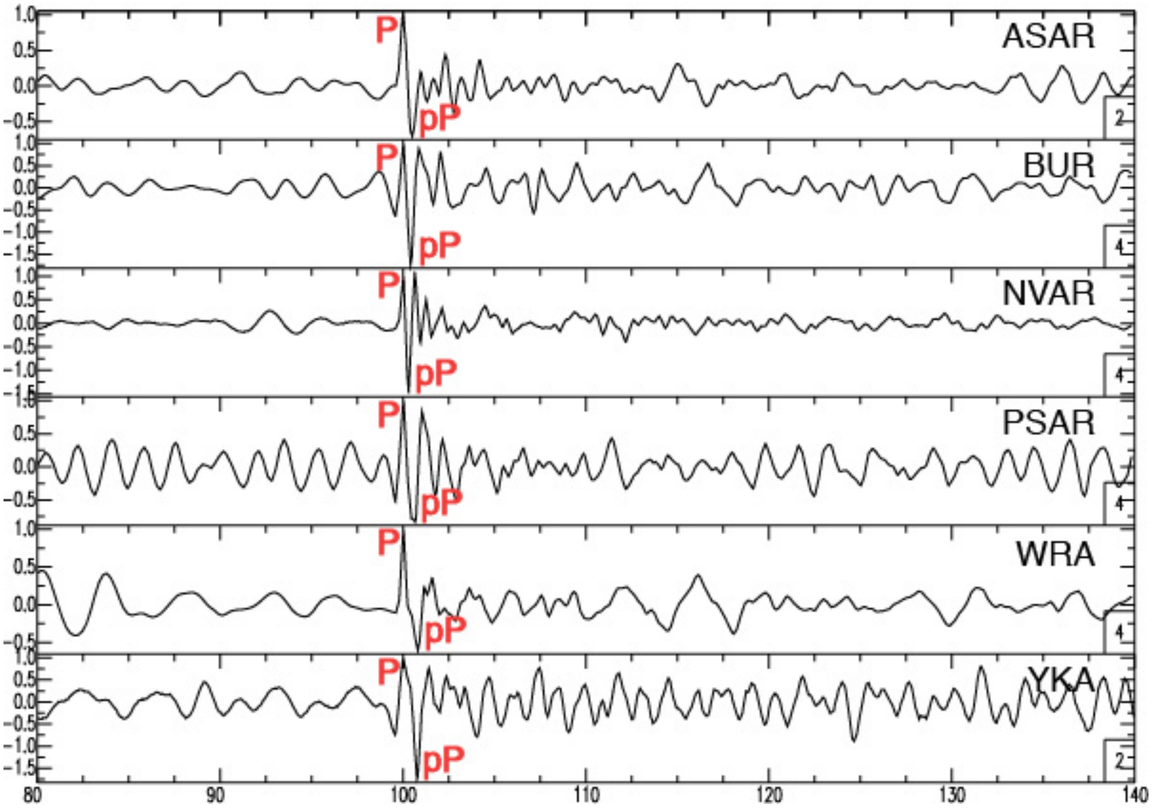

Figure 3.4 Stacked traces from arrays recording the 02/12/2013 event. Traces are aligned on *P* at 100 s, normalized to *P* amplitude, filtered with a highpass filter (ASAR: 0.4 Hz, BUR: 0.4 Hz, NVAR: 0.3 Hz, PSAR: 0.5 Hz, WRA: 0.3 Hz, YKA: 0.5 Hz), and stacked.

The time series output by WPP are specified to be 10 seconds long, which is long enough to capture the *P* and *pP* arrivals at the collection plane after the initiation of the source, as well as accommodate variations in arrival time of *P* and *pP* due to variable distance between the source and collection plane due to changes in source depth between different source locations. The time series are written out every 200 m along the collection plane, which is at least 13 receivers per *P* wavelength.

Once the time series from the 3D waveform propagation have been output by WPP, they are windowed to start just before the *P*-wave arrival to make Green's function calculations more efficient. The strain outputs are used to calculate the stresses on the collection plane as described in Chapter 2. The representation theorem is implemented to calculate primitive Green's functions (PGFs – refer to Chapter 2 for details) to each average array location for a given event. No geometric spreading or attenuation corrections are applied to the synthetic PGFs in this case because these corrections would affect the amplitudes of *P* and *pP* uniformly; the relative amplitudes of these phases would not be affected by these corrections because they have the same frequency content.

Now there is an observed dataset for each explosion of one stacked trace per teleseismic array, and a synthetic dataset of one PGF per teleseismic array for each source grid search location. In each trace, we measure the ratio of the first up-swing to the first down-swing in the explosion signal. Since the sources are so shallow and there is a high degree of interference between *P* and *pP*, we refer to these arrivals merely as *a* and *b* since they are so closely associated in space and time that they cannot truly be referred to as distinct phases (Figures 3.2-3.4). These *a/b* ratios are input into a data matrix, with columns corresponding to the ratios calculated from observed data in column 1, and ratios calculated from synthetic data sets for each grid location in the other columns. Each row corresponds to a particular teleseismic array. Using this data matrix, each of the synthetic datasets are correlated to the observed dataset to determine which source location(s) best match(es) the observed pattern of *a/b* ratio changes due to the azimuth / distance of each array relative to the source location, and therefore due to the particular scattering effects of the topography sampled by each particular ray path.

3.4 Results

The correlation coefficients for each source grid location are plotted in Figures 3.5-3.7. On average, the correlation of the *a/b* amplitude ratios of the grid locations to those of the observed data for the 2006 event is very high, at 0.9953. There is a clear pattern of decreasing correlation from the northeast to the southwest of the source grid (Figure 3.5). The correlation coefficients vary between 0.9891 and 0.9988. The source location with the highest correlation to the 2006 observations corresponds to a depth of 478 m (Table 3.1a).

The correlation plots of the 2009 and 2013 event area (Figures 3.6 and 3.7) bear a strong similarity, with only subtle differences in relative correlation of locations within the source grid to *a/b* ratios in the observed event data. The average *a/b* correlation of source locations to the 2009 event data is 0.7193, with values ranging from 0.5177 to 0.8057. The source locations with the highest correlation coefficients are r2c4 (0.8057), r1c3 (0.8024), and r1c2 (0.7988) (Figure 3.6), with source depths of 434 m, 641 m, and 613 m, respectively (Table 3.1b). The 2013 *a/b* correlations range from 0.7324 to 0.8987, with an average value of 0.8401. The source locations with the highest correlation to the observed *a/b* ratios are r1c3 (0.8987), r1c4 (0.8876), r1c2 (0.8839), and r2c4 (0.8825) (Figure 3.7), with source depths 641 m, 576 m, 613 m, and 434 m, respectively (Table 3.1b). The northeast-to-southwest pattern of decreasing correlations is consistent between the 2009 and 2013 events, with the highest correlations for the 2013 event corresponding to generally deeper source locations than for the 2009 event.

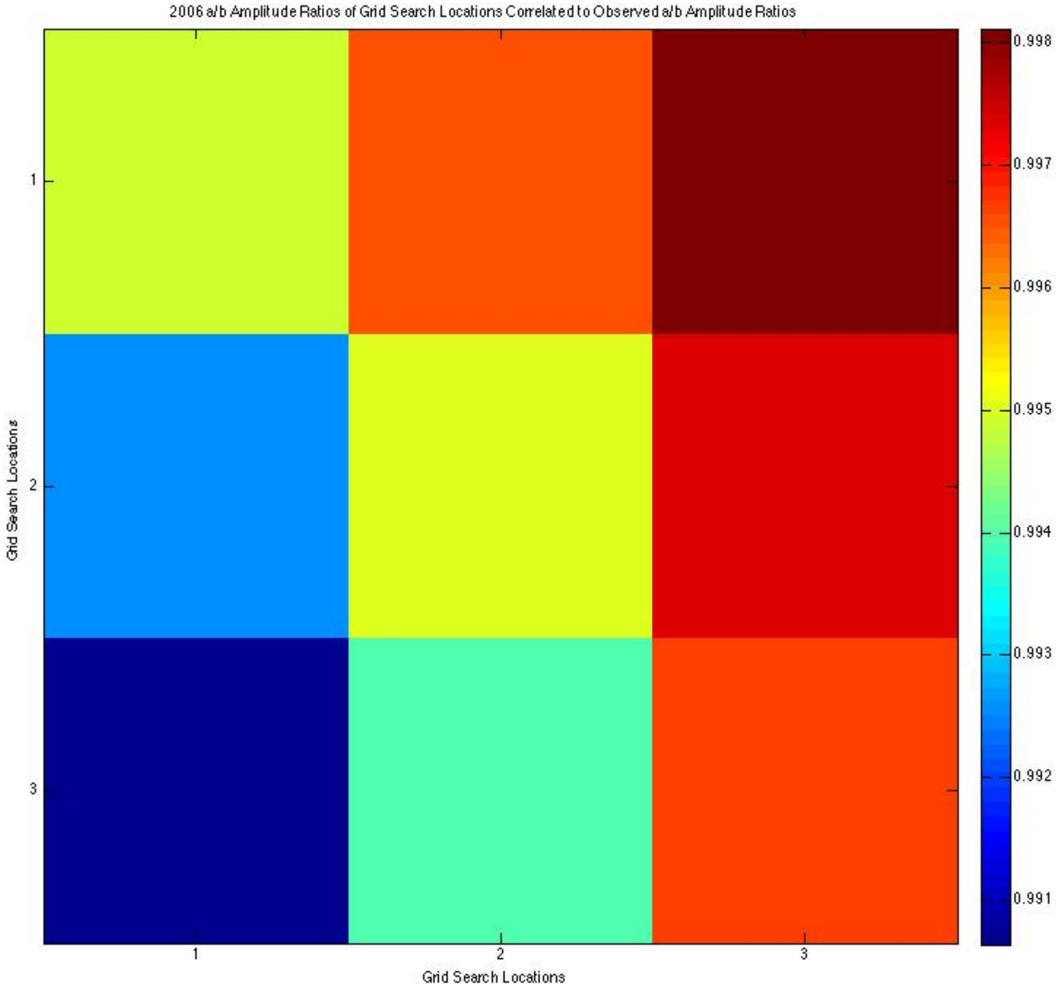

Figure 3.5 Correlation between different source grid locations and observed *a/b* amplitude ratios for the 10/09/2006 event. Locations shown correspond do those in the Figure 3.1 map.

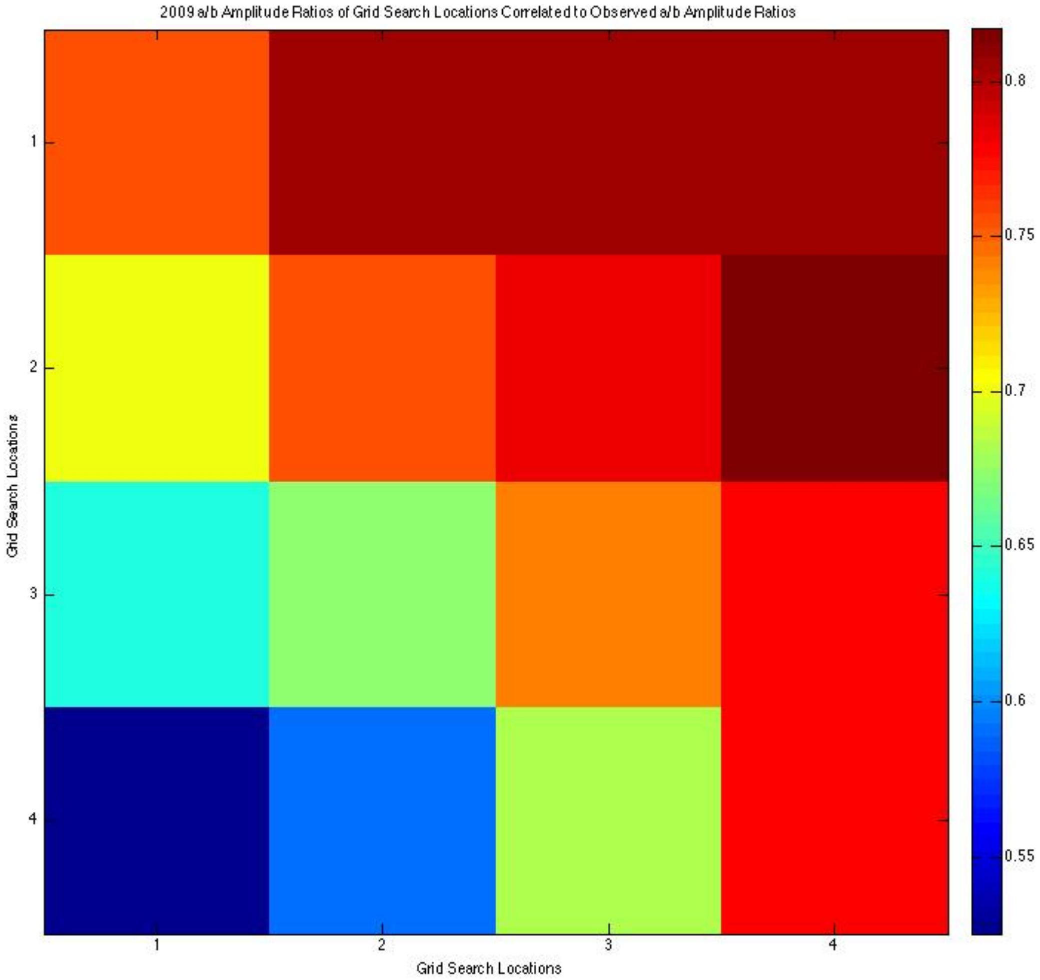

Figure 3.6 Correlation between different source grid locations and observed *a/b* amplitude ratios for the 05/25/2009 event. Locations shown correspond to those in the Figure 3.1 map.

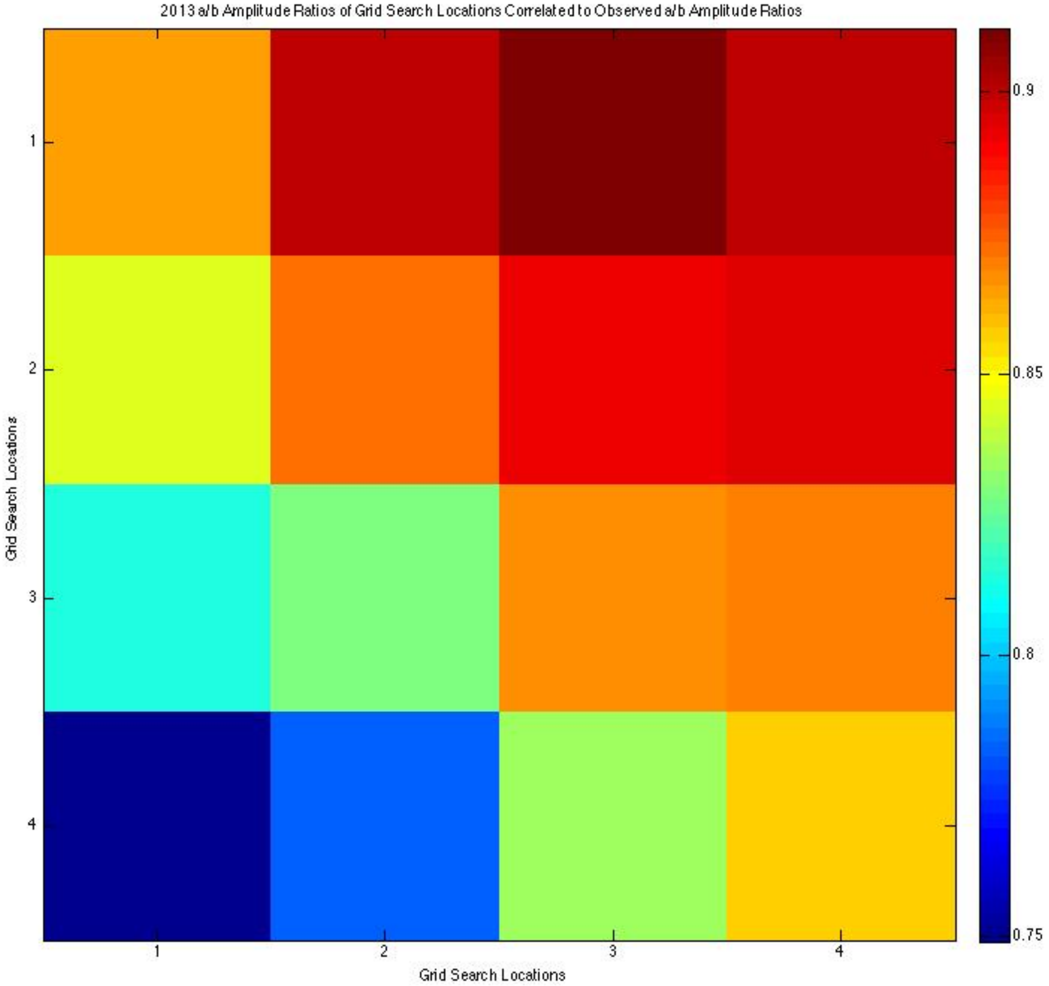

Figure 3.7 Correlation between different source grid locations and observed *a/b* amplitude ratios for the 02/12/2013 event. Locations shown correspond to those in the Figure 3.1 map.

3.5 Discussion and Conclusions

The most highly-correlated location (r1c3) to the 2006 event data is slightly northeast of the Wen and Long (2010) location (Figure 3.8). The colors in the map correspond to degree of correlation, as shown in Figure 3.5. The depth of the event is 478 m, based on our estimate of the tunnel entrance, and is much deeper than the 200 m (100 to 300 m) reported by Murphy et al. (2010), but our source depths are independent of yield estimates for these events. The very high average correlation of the grid locations to the observed event data is likely due to the small number of observation data available for this event, so results are probably dominated by the NVAR array stack, which matches the PGFs across the grid very well, compared to ASAR and WRA (Appendix A).

The four 2009 and 2013 source grid locations with the highest correlation to the observed data for each event are not distinguishable with any certainty. The locations with the highest correlation however, are different: r2c4 for 2009, and location r1c3 for 2013, corresponding to source depths 434 m and 641 m, respectively. The maps of the correlations for the 2009 and 2013 events (Figures 3.6-3.9) indicate that the 2013 event location might be less than ~560 m away from, and slightly to the northwest of the 2009 event. Since these locations fall on the edge of our source grid, it is possible that the 2009 event is located further eastward, and / or the 2013 event is located further to the north/northwest. As is, the relative location of the 2009 and 2013 events is generally consistent with the 2009 and 2013 locations reported by Zhang and Wen (2013).

Our likeliest source location depths (those with highest correlation to observed data) for the 2009 and 2013 events are consistent with those of Murphy et al. (2010) and Zhang and Wen (2013) (434-641 m, compared to published range of 350-750 m), although slightly to the east of the previous locations (Murphy et al., 2010; Wen and Long, 2010; Zhang and Wen, 2013). The average depth of the four grid locations with the highest correlation to the 2009 event is 566 m, which is the same average depth for the four grid locations with the highest correlation to the 2013 event, since both events have the same four highest correlated locations, but different single locations with highest correlation. Although the locations with the highest correlation are different between the 2009 and 2013 events, the locations with the lowest correlation are the same for both events, so unlikely source locations are apparent and consistent for both events (see Figures 3.6 and 3.7).

A basic question arises from these results. Is the *a/b* amplitude ratio more the result of source depth or topographic scattering? If we examine the depth range of the three highest-correlated source locations for the 2009 event (207 m) and compare it to that for the 2013 event (65 m), and consider the lowest-correlated locations as well (85 m for the 4 lowest-correlated locations for both events), it is evident first that there is a small range of source depths that correlate well with the observed data. Well-correlated locations have the deepest source depths in our location grid (434-641 m), and poorly-located locations have very shallow source depths (210-295 m). This seeming dependence of the results on source depth provides an argument for the sensitivity of the *a/b* results on source depth. On the other hand, scattering can be complex and difficult to predict, which is why we use realistic topography in the near-source region and focus on its potential effects for this study. However, all of the source depths we are considering in this study are very shallow, and we would expect the sensitivity of the upgoing wavefield to topography to increase with increasing source depth. The upgoing wavefield would sense a wider area of varying topography as the distance to the surface increases, so it is also possible that the deeper (and better correlated) source grid locations reflect a combined sensitivity to source depth and topographic scattering effects on *a/b* amplitude ratio.

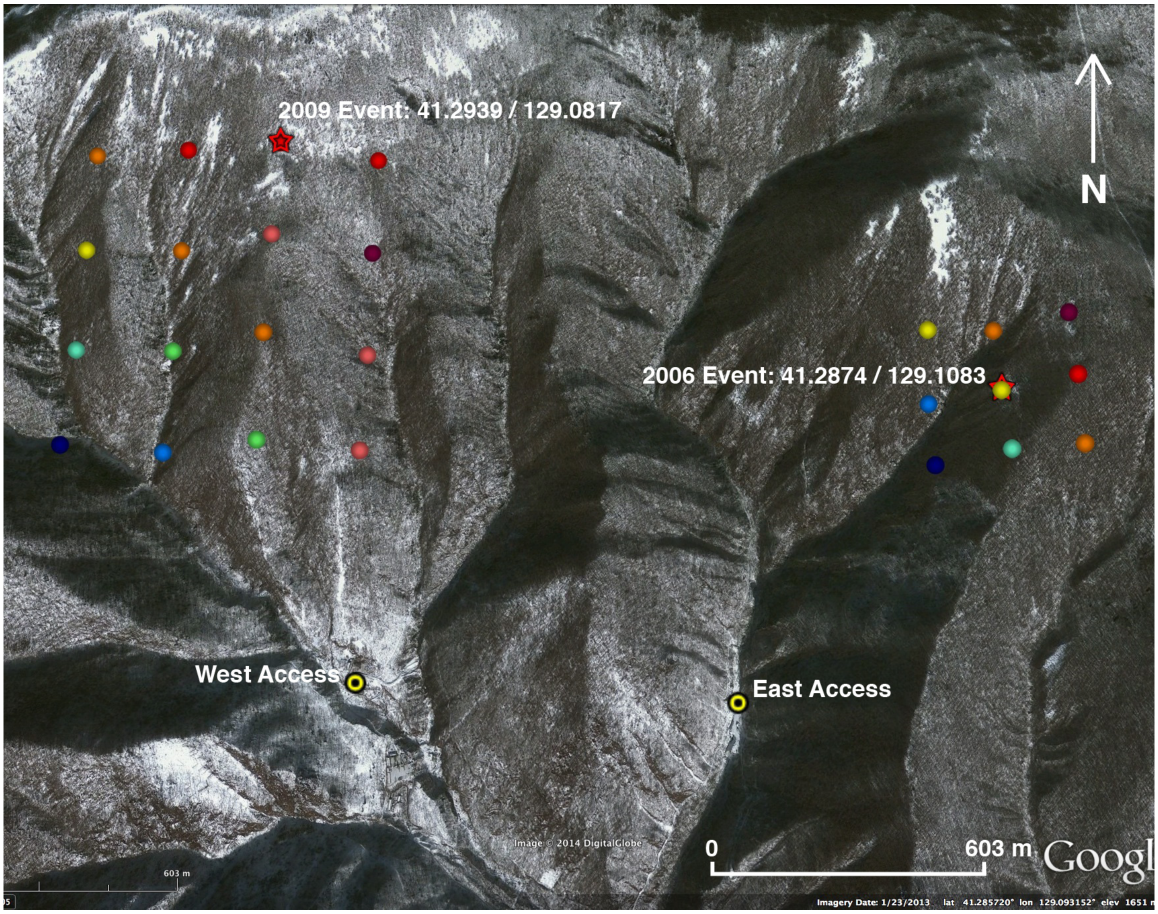

Figure 3.8 Google Earth image (image date: 01/23/2013) of North Korea nuclear test site with 2006 and 2009 source locations (red stars) from Wen and Long (2010) and grid search locations with colors corresponding to degree of correlation between observed *a/b* amplitude ratios and synthetic *a/b* ratios. Color scales for each event map correspond to those in Figures 3.5 and 3.6.

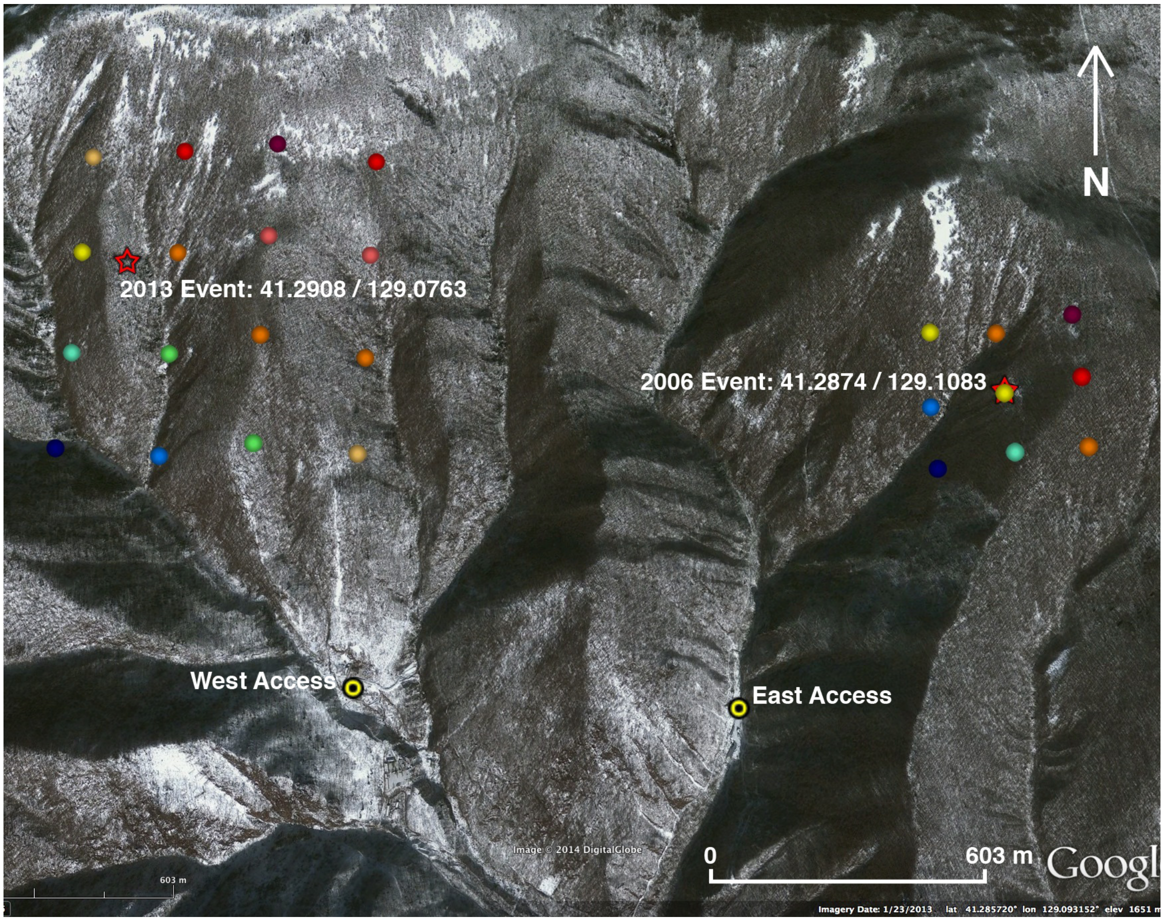

Figure 3.9 Google Earth image (image date: 01/23/2013) of North Korea nuclear test site with 2006 and 2013 source locations (red stars) from Wen and Long (2010) and Zhang and Long (2013) and grid search locations with colors corresponding to degree of correlation between observed *a/b* amplitude ratios and synthetic *a/b* ratios. Color scales for each event map correspond to those in Figures 3.5 and 3.7.

Correlation coefficients calculated for *a/*b amplitude ratios of a population of synthetic primitive Green's functions (PGFs) compared to a population of observed ratios result in a location for the 2006 North Korea nuclear test that is slightly northeast of the location of Wen and Long (2010), and has a depth greater than that estimated by Murphy et al. (2010). Differences between the correlation of locations on the grid between the 2009 and 2013 events indicate that the 2013 event is located slightly to the northwest of the 2009 event, but these differences are not well resolved by our grid geometry for the source location search. Extending the grid may help resolve a single best location for both events. Both the 2009 and 2013 event location depths in our study are consistent with previous estimates (Murphy et al., 2010; Zhang and Wen, 2013), but both event locations in our study are slightly east of the locations reported by Murphy et al. (2010), Wen and Long (2010), and Zhang and Wen (2013). The relative locations of the 2006, 2009, and 2013 events found by our process are quite compatible with the relative locations found from differential travel time relative locations by Wen and Long (2010) and Zhang and Wen (2013).

Uncertainties in these results do exist. Differences between the source time functions of the 2009 and 2013 events are likely, but unaddressed by our synthetic PGFs. The 2013 source time function is probably longer period due to its larger source yield, which could contribute to the difficulty in discerning distinctly different locations for these events. It is also possible that the difference in the event locations is smaller than the 200 m source location grid spacing, or more likely, the grid extent is not wide enough to resolve a single optimal result for each event. Possible uncertainties in the correlation could exist due to the possibility that the correlation may be magnifying very minor changes in relative *a/b* amplitude ratios, although the correlations seem stable across the grid search locations, relative to the degree of variation observed in the synthetic PGFs across the source location grids.

Using the representation theorem seems to be a promising strategy for constraining source depth for these explosive sources, as sensitivity of *a/b* ratio to source depth is evident. However, use of restricted seismic array data collected for international monitoring, and extension of the source location grids, could better constrain source depths and locations. Future studies will test the application of attenuation and geometric spreading corrections to calculate absolute amplitudes of teleseismic *P*-waves and may be used for earthquake sources rather than isotropic sources.

3.6 References

Avants, M., T. Lay, X-B. Xie, and X. Yang (2011), Effects of 2D random velocity heterogeneities in the mantle lid and Moho topography on *Pn* geometric spreading, *Bull. Seismol. Soc. Am.*, **101**, 126-140.

He. Y., X-B. Xie, and T. Lay (2008), Explosion-source energy partitioning and *Lg*-wave excitation: contributions of free-surface scattering, *Bull. Seismol. Soc. Am.*, **98**, 778-792.

Murphy, J.R., B.C. Kohl, J.L. Stevens, T.J. Bennett, and H.G. Israelsson (2010), Exploitation of the IMS and other data for a comprehensive, advanced analysis of the North Korean nuclear tests, paper presented at the 2010 Monitoring Research Review: Ground-Based Nuclear Explosion Monitoring Technologies, Natl. Nucl. Security Admin., Washington, D.C.

Murphy, J.R., J.L. Stevens, B.C. Kohl, T.J. Bennett, and B.W. Barker (2011), Supplemental analysis of the seismic characteristics of the 2006 and 2009 North Korean nuclear tests, paper presented at the 2011 Monitoring Research Review: Ground-Based Nuclear Explosion Monitoring Technologies, Natl. Nucl. Security Admin., Washington, D.C.

Petersson, N.A. and B. Sjögreen (2011), User's guide to WPP version 2.1.5, *Tech. Rep. LLNL-SM-487431*, Lawrence Livermore Natl. Lab. Livermore, California.

Rodgers, A.J., N.A. Peterson, and B.Sjögreen (2010), Simulation of topographic effects on seismic waves from shallow explosions near the North Korean nuclear test site with emphasis on shear wave generation, *J. Geophys. Res.*, **115**, B11309, doi: 10.1029/2010JB007707.

Stead, R.J., and D.V. Helmberger (1988), Numerical-analytical interfacing in two dimensions with applications to modeling NTS seismograms, *PAGEOPH*, **128**, 157-193.

Stephens, J.L. and H. Xu (2010), Wave propagation from complex 3D sources using the representation theorem, paper presented at the 2010 Monitoring Research Review: Ground-Based Nuclear Explosion Monitoring Technologies, Natl. Nucl. Security Admin., Washington, D.C.

Wen, L. and H. Long (2010), High-precision location of North Korea's 2009 nuclear test, *Seismol. Res. Lett.*, **81**, 26-29.

Zhang, M. and L. Wen (2013), High-precision location and yield of North Korea's 2013 nuclear test, *Geophys. Res. Lett.*, **40**, 2941-2946.

Chapter 4

Rupture model of the 2008 Wenchuan earthquake using 3D Green functions

Megan Avants and Thorne Lay

University of California Santa Cruz, Department of Earth and Planetary Sciences

4.1 Abstract

We present rupture models for the 2008 Wenchuan earthquake based on both 1D and 3D teleseismic *P*-wave Green functions, to determine how a model produced using 3D Green functions compares to one calculated using 1D Green functions. We calculate 3D Green functions for a half space with realistic surface topography on a fault divided into 3 segments with varying dip. The 1D Green functions are calculated for a half space with a flat surface, with the same fault geometry as for the 3D case. Results show our 1D and 3D fault rupture models are consistent with each other and with results of previous studies. The models both show two regions of peak slip 45 km and 180 km northeast of the epicenter, with a thrust mechanism in the southwest transitioning to dextral strike-slip to the northeast. We find the fault model produced using 3D Green functions is nearly indistinguishable from that based on 1D Green functions despite significant differences of the Green functions for certain azimuths. The finite fault model inversion is robust in this regard, with variations in the Green functions not projecting into the source model to a significant extent.

4.2 Introduction

The May 12, 2008 Wenchuan earthquake (M_w 7.9) occurred at the eastern margin of the Tibetan plateau, along the Sichuan Basin (Figure 4.1a; Yin, 2010), the result of

Figure 4.1 (next page) a) Regional map of Longmen Shan thrust belt, modified from Yin, 2010. Large arrows denote the relative motion of eastern Tibetan Plateau relative to the Sichuan Basin; b) Map focusing on fault area, showing Wenchuan aftershock locations with focal mechanisms from the Global Centroid-Moment Tensor (GCMT) catalog hinting at a complicated rupture process along the fault.

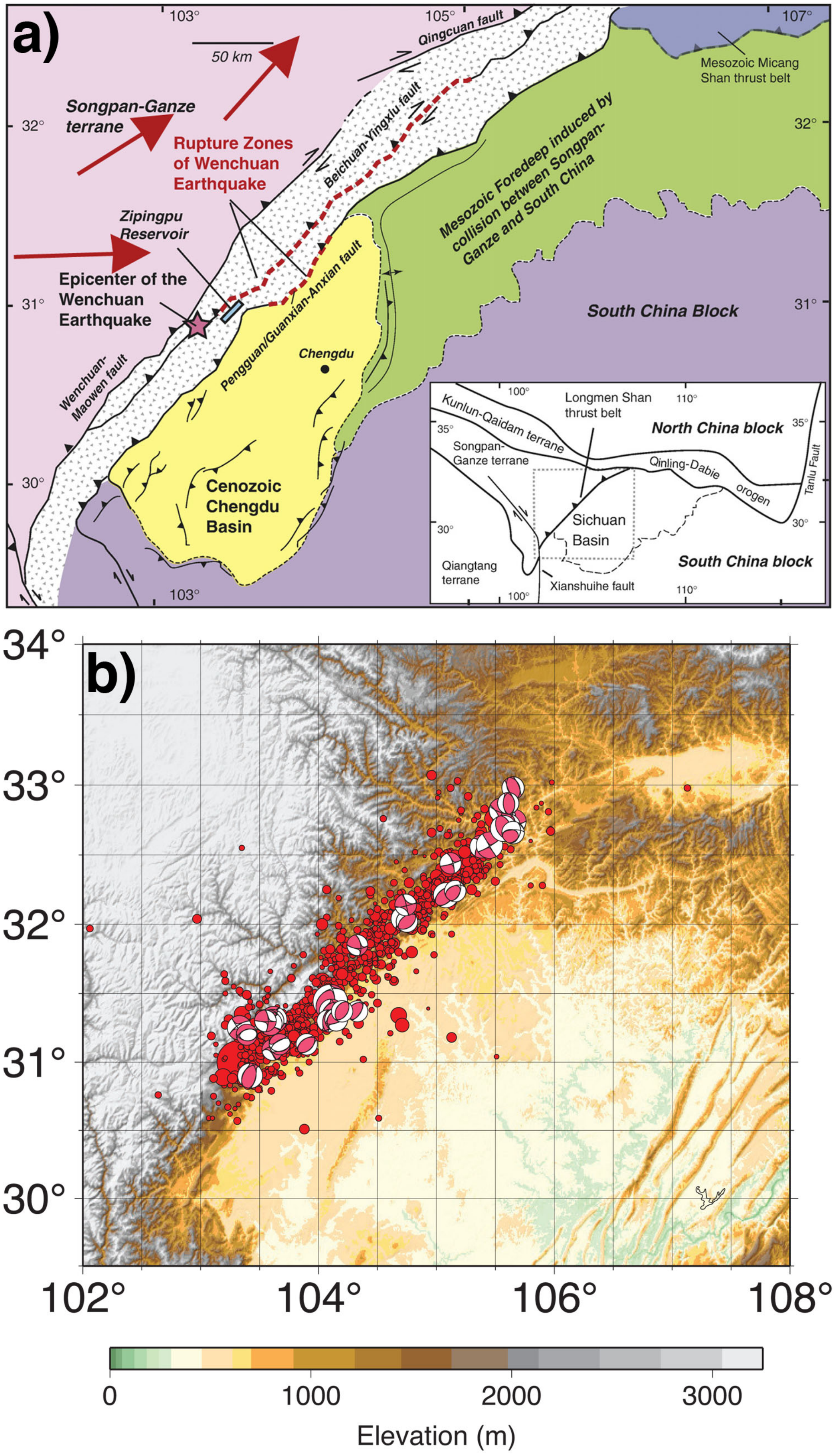
a)
103°
105°
107°
50 km
Qingcuan fault
Songpan-Ganze terrane
Rupture Zones of Wenchuan Earthquake
Beichuan-Yingxiu fault
Mesozoic Micang Shan thrust belt
Mesozoic Foredeep induced by collision between Songpan-Ganze and South China
Zipingpu Reservoir
Epicenter of the Wenchuan Earthquake
Pengguan/Guanxian-Anxian fault
Chengdu
South China Block
Wenchuan-Maowen fault
Cenozoic Chengdu Basin
32°
31°
30°
103°
100°
110°
Longmen Shan thrust belt
Kunlun-Qaidam terrane
North China block
35°
Songpan-Ganze terrane
Qinling-Dabie orogen
Tanlu Fault
Sichuan Basin
Qiangtang terrane
Xianshuihe fault
South China block
b)
34°
33°
32°
31°
30°
102°
104°
106°
108°
0
1000
2000
3000
Elevation (m)

convergent motion between these two tectonic provinces. Similar to the Sierra Nevada Mountains of North America, but on a more dramatic scale, the Longmen Shan and Min Shan ranges exhibit high relief on their eastern edge, sloping more gradually to the west (Burchfiel et al., 2008). This eastern margin, known as the Longmen Shan thrust belt, is comprised of a network of significant faults and is notable for a sharp topographic contrast of 3000-4000 m over a lateral distance of tens of kilometers, transitioning to a broader, topographically irregular boundary with a poorly defined mountain front toward the north (Burchfiel et al., 1995). The variable topographic character of this region is in agreement with rupture complexity (e.g., Hao et al., 2009; Shen et al., 2009; Hashimoto et al., 2010; Lin et al., 2009, Xu et al., 2009; Tong et al., 2010; Ji and Hayes, 2008; Zhang et al., 2009; Nakamura et al., 2009; Zhao et al., 2010, Zhang and Ge, 2010; and Wen et al., 2012) for this earthquake, as evidenced by global centroid-moment tensor focal mechanisms of significant aftershocks along the fault zone (Figure 4.1b).

Field observations trace a 240-290 km surface rupture (Hao et al., 2009; Lin et al., 2009; Xu et al., 2009), with a distinct transition from thrust-dominant faulting in the south to more right-lateral strike-slip in the north (Hao et al., 2009; Xu et al., 2009). They also find evidence of coseismic slip on multiple faults in the Longmen Shan thrust belt, with reports of rupture mainly on the Beichuan and Pengguan Faults (Figure 4.1a) (Hao et al., 2009; Lin et al., 2009; Xu et al., 2009, Tong et al., 2010). Remote sensing confirms these findings and further characterizes the rupture as segmented, with changes in rupture mechanism corresponding to changes in fault dip from southwest to northeast. Hao et al. (2009) concluded that the earthquake ruptured two coseismic fault zones based on analysis of InSAR data resolved a thrust mechanism in the southwest portion of the rupture, with coseismic slip on both the Beichuan and Pengguan Faults, and a right-lateral strike-slip mechanism to the northeast. Hashimoto et al. (2010) derived a best-fit model from the same InSAR data with 8 segments along the Beichuan Fault, dipping northwestward at 33 degrees in the southwestern segments and 70 degrees in the northeastern segments. Rupture mechanisms transition from thrust in the south to dextral in the north in their study as well. Shen et al. (2009) inverted GPS and InSAR data to determine a fault model with a 43-degree thrust fault geometry in the southwest transitioning to a 96-degree strike-slip fault geometry at the northeast end of the rupture extent, divided into 6 different fault dip segments on the Beichuan Fault. Their model also includes thrust slip on the adjacent Pengguan Fault, which dips much more shallowly at 28 degrees and is thought to have a common root with the Beichuan Fault at depth, but slip on this fault is relatively minor. Tong et al. (2010) concluded that the Wenchuan earthquake ruptured three segments along the Beichuan Fault, and a single 70-km segment along the adjacent Pengguan Fault, based on observations from InSAR, GPS, and field investigations. The three fault segments on the Beichuan Fault have dips of 35, 50, and 70 degrees from south to north, and the Pengguan Fault is modeled with a 25-degree dip. Slip on these segments, as in the other studies, transitions from thrust in the south to dextral slip in the north, in accordance with changes in fault dip.

Rupture models produced from teleseismic waveform data consistently show two or more peak slip areas along the fault surface, which differ in depth and rupture mechanism (e.g., Ji and Hayes, 2008; Zhang et al., 2009; Nakamura et al., 2010; Zhao et al., 2010; Zhang and Ge, 2010; Wen et al., 2012), from which fault segmentation is inferred. Many models were confined to a single fault geometry due to the limitations of teleseismic inversion methods. There is consistency between these models, with fault lengths of about 230 to 300 km (Ji and Hayes, 2008; Zhang and Ge, 2010; Zhao et al., 2010), dips from 32 to 42 degrees (Ji and Hayes, 2008; Zhang et al., 2009; Zhao et al., 2010), and slip transitioning from thrust to strike-slip from southwest to northeast (Ji and Hayes, 2008; Zhao et al., 2010). Other seismic rupture models did allow for changes in fault geometry along the length of the rupture. Of these, Nakamura et al. (2010) modeled a fault of length 290 km with two segments: one with thrust motion approximately 110 km long from the epicenter, with a dip of 33 degrees northwest, and the other segment dipping 60 degrees northwest with predominantly strike-slip motion. Wen et al. (2012) constructed a fault model using empirical Green functions (EGFs) from thrust and strike-slip events and divided the fault plane into 3 segments: the southernmost one only 25 km long, dipping at 33 degrees, the central segment 100 km long, dipping at 33 degrees, and the northern segment 155 km long, with a 50-degree dip. Wen et al. acknowledge slip on the parallel Pengguan Fault, but treat slip on that fault as slip on the Beichuan fault, since rupture on both faults is probably below the resolution threshold for teleseismic data inversion.

This study builds on these findings, presenting a finite fault model allowing for variable dip along a fault of constant strike, using 3-dimensional Green functions (3DGFs) which capture the effects of the dramatic topographic contrast across the fault on the teleseismic *P*-wave field. We compare finite fault inversion results from 1-D and 3-D Green functions.

4.3 Methods

Since our study focuses on capturing the topographic effects of the near-fault zone on the teleseismic *P*-wave field, we begin by examining the fault zone for segmentation based on topographic character. Figure 4.2 shows the mapped surface traces of the Wenchuan-Maowen Fault, the Beichuan Fault, and the Pengguan Fault, as well as a model fault of constant strike superimposed on the Beichuan Fault, and the epicenters determined by USGS NEIC and the China Earthquake Networks Center. The three segments of the fault are bounded by the red marks across the Beichuan Fault. These segments were determined by creating about 16 transects of the fault and comparing the topographic profiles across the fault in Google Earth. The three segments we decided on agree largely with the existing literature (e.g., Tong et al., 2010; Wen et al., 2012), as well as tectonic blocks outlined by Burchfiel et al. (2008). Our model fault is a single trace 285 km long with a 228-degree strike, based on the fault maps and strikes reported in published studies, which range from 220-230 degrees (e.g., Hashimoto et al., 2010; Ji and Hayes, 2008; Zhang et al., 2009; Nakamura et al., 2010; Zhao et al., 2010; Wen et al., 2012). Each segment has a different dip: the southernmost segment is 50 km long and dips at 35 degrees, the central segment is 110 km long and has a 50-degree dip, and the northernmost segment is 125 km in length and has a 70-degree dip (e.g., Hashimoto et al., 2010; Nakamura et al., 2010).

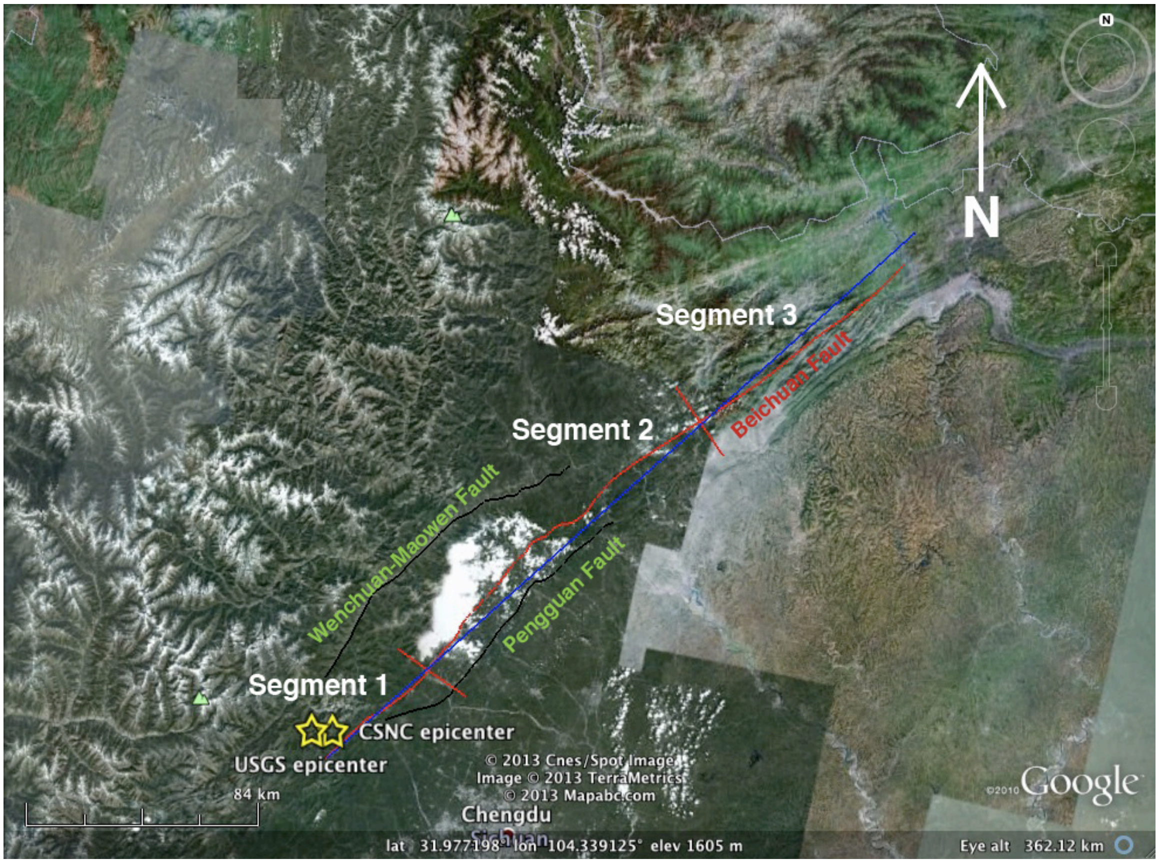

Figure 4.2 Google Earth Image (image date: 4/10/2013) with surface traces of Wenchuan-Maowen, Beichuan, and Pengguan Faults shown, as well as the simplified, segmented model fault used for this study in blue.

Rupture depth in the literature is highly variable, with most seismic studies resolving maximum rupture depths of 20-50 km (Ji and Hayes, 2008; Zhang et al., 2009; Nakamura et al., 2010; Zhao et al., 2010; Wen et al., 2012). The southwest thrust region generally has deeper rupture than the northeast region amongst these depth estimates. The GPS and InSAR studies estimate rupture depth to be 0-45 km, with most estimates falling in the 0-30 km range (Hao et al., 2009; Shen et al., 2009; Hashimoto et al., 2010; Tong et al., 2010). In most of these studies, both seismic and remote sensing, large slip is confined mostly to depths less than or equal to 15 km, so we resolve rupture on our fault to depths of 24 km. Shen et al. (2009) and Tong et al. (2010) have all significant slip (thrust and strike-slip) confined to the uppermost 10 km of the fault in their models.

Once the model fault geometry was determined, we started designing our strategy for creating synthetic 3DGFs to input into the finite fault inversion. We used a SRTM (Shuttle Radar Topography Mission) topographic model of the region with 90 m resolution (www.srtm.csi.cgiar.org/SELECTION/inputCoord.asp), where 5x5 degree tiles can be selected and downloaded (Figure 4.3). We then decided on three sets of fault locations at which to create 3DGFs at 3 depths along the fault plane: 6 km, 12 km, and 18 km. Each of these three sets of earthquakes are treated as a 2.5D model of the fault, being repeated along-strike within each fault segment. We used the 3D waveform propagation program, WPP, developed at Lawrence Livermore National Laboratory (Petersson and Sjögreen, 2011), to simulate 18 subfaults: one at each of the 9 locations with a rake of 90 degrees, and one at each location with a rake of 180 degrees, to allow for a solution in the fault model inversion having any rake between pure thrust and pure strike slip. WPP calculates 3D wave propagation in displacement on a Cartesian grid, allowing for realistic surface topography in simulations. The velocity model we use is a half space (Vp=5570 m/s; Vs=3360 m/s; density=2650 kg/m^3) because we want to isolate the effects of the locally dramatic topography on the Green functions, but also because the crust is known to be very thick in the fault region (Xu and Song, 2010). We determine 3DGFs from the output of the 3D earthquake simulations by implementing the representation theorem, as described in Chapter 2. The output from our implementation of the representation theorem are primitive Green functions (PGFs), meaning they are only the impulse respone from within the 3D model volume, with a 1-second wide Gaussian source time function. To calculate and apply amplitude corrections due to geometric spreading and attenuation through the rest of the teleseismic path to each of 40 station locations, we modify the function in Kikuchi and Kanamori (1982) that calculates

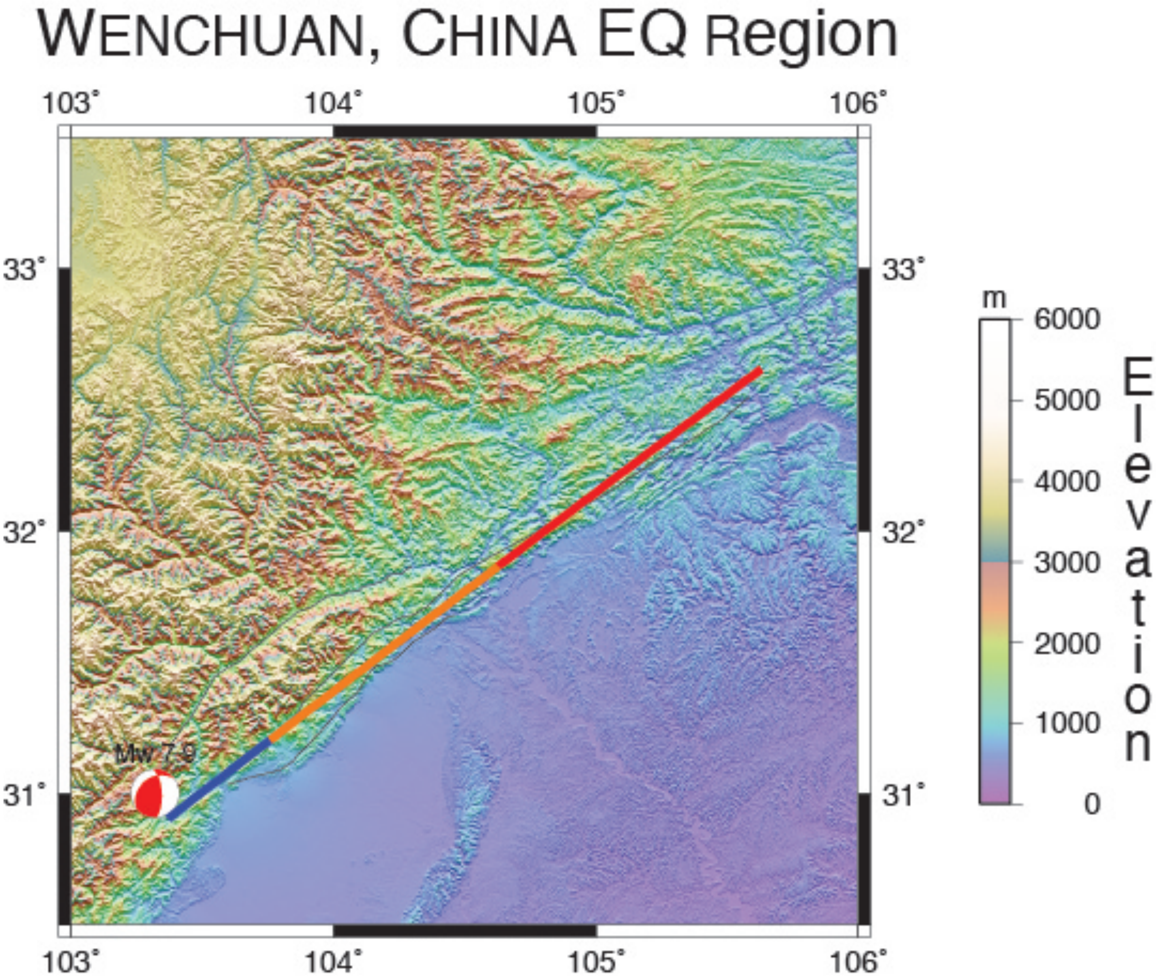

Figure 4.3 Map of earthquake region, with topography shown the same topographic model as used in calculation of 3DGFs. Simplified, segmented model Beichuan Fault superimposed. Blue segment has dip=35°, orange segment has dip=50°, and red segment has dip=70°.

Green functions for a user-specified 1D radially stratified near-source Earth to accept our 3D PGFs created from the representation theorem, convolve them with a function to make the resulting source time function equivalent to a 4-second wide triangle, and apply attenuation and geometric spreading amplitude corrections to the time series. This results in 3DGFs from each of the 18 sources to 40 teleseismic stations.

We then calculate the same set of Green functions with a 1D Earth model (1DGFs), which is also a half space, but with a flat surface, using the same 4-second wide trangle source time function. Representative examples of the similarites and differences between the 1D and 3D GFs are shown in Figure 4.4 for a single station. The Green functions primarily involve *P*, *pP*, and *sP* arrivals, with reflection from the rough topography complicating the surface reflections and in some cases leading to multiple surface arrivals from different regions of the surface. Layered crustal models were considered for the 1D structure, with minor impact on the finite-fault inversions, and we used a half-space for the 3D rough surface topography models due to the need to isolate down-going *P* wave energy from down-going *S* wave energy as much as possible. Thus, the overall duration of the Green functions is bounded to be less than the time between down-going *P* and down-going *S*. If layering below the subfault depth is used, the time duration is shortened to the time between down-going *P* and down-going *P*-to-*S* conversions, which is unacceptably short. This limitation is computational, as the 3D finite difference grid has to be located at a depth that provides good separation between *P* and *S* energy reaching the surface on which the representation theorem is applied.

The finite fault rupture model inversion developed by Kikuchi and Kanamori (1991) was modified to allow for fault segments of varying dip along the rupture plane. For the inversion, the hypocenter depth is 18 km. The fault is discretized into 3 depth bins, each 12 km wide, centered at 6 km, 12 km, and 18 km. Along strike, the fault is discretized into 15 km long sub-faults such that segment 1 (dip=35) has 4 subfaults along strike, segment 2 (dip=50) has 7 subfaults along strike, and segment 3 (dip=70) has 8 subfaults along strike. Each subfault has a source time function comprised of 5 2-second rise time, 2-second shifted symmetric triangles, so that the total sub-fault rupture duration lasts up to 12 seconds. Rupture velocity is assumed to be constant at 2.8 km/s (consistent with Nakamura et al., 2010). The 1DGFs and the 3DGFs are then input into the inversion to produce 1D and 3D finite fault rupture models, shown in Figure 4.5.

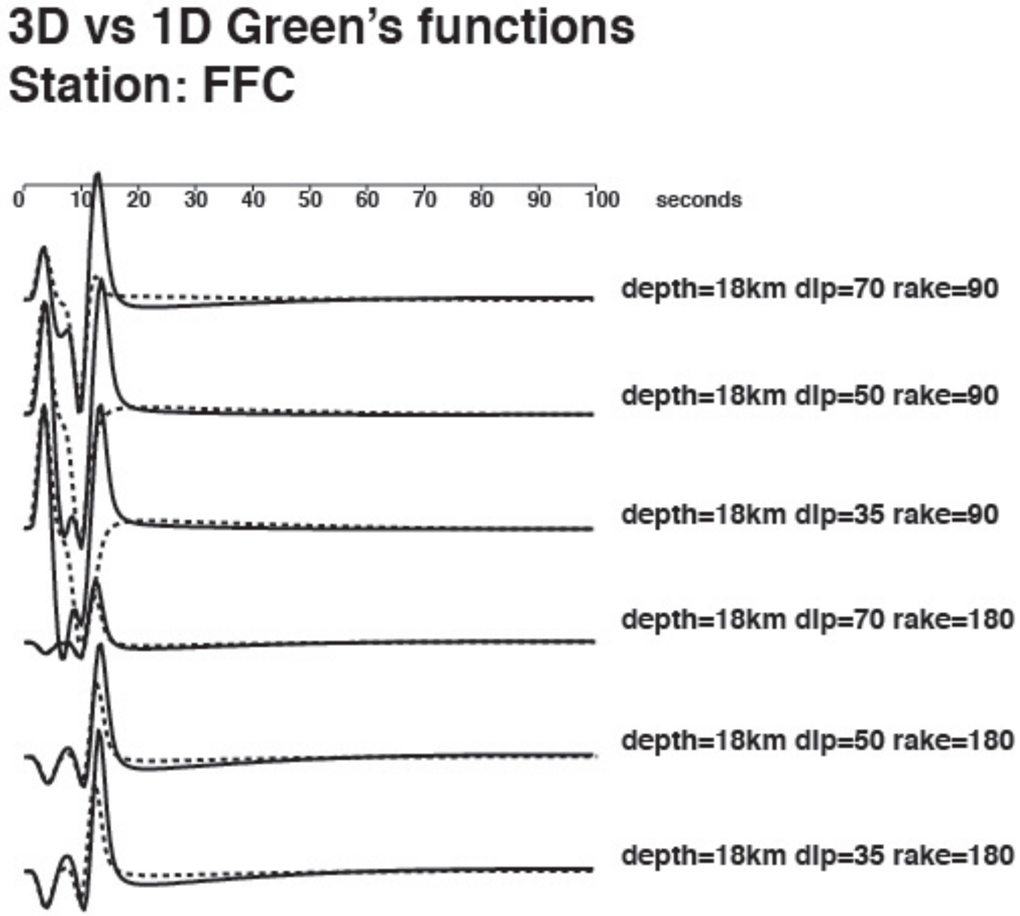

Figure 4.4 3DGFs (solid line) and 1DGFs (dashed line) calculated to station FFC (Azimuth = 14 degrees, distance = 92 degrees from epicenter). The most dramatic differences between the two types of Green functions were apparent in the deepest source locations, which are shown here. Shown are Green functions from 6 sources at 18 km depth in each fault segment, each with 90-degree rake and 180-degree rake.

4.4 Results

The slip distribution models resulting from use of 3D and 1D Green functions are shown in Figure 4.5. Both models assume the rupture plane is segmented into 3 parts, with dips of 35, 50, and 70 degrees from southwest to northeast. Results from both models show peaks in slip along the rupture plane at 45 km and 180 km northeast of the epicenter. Slip also transitions from a predominantly thrust mechanism to mostly strike-slip with distance along the rupture plane.

3D Green Functions

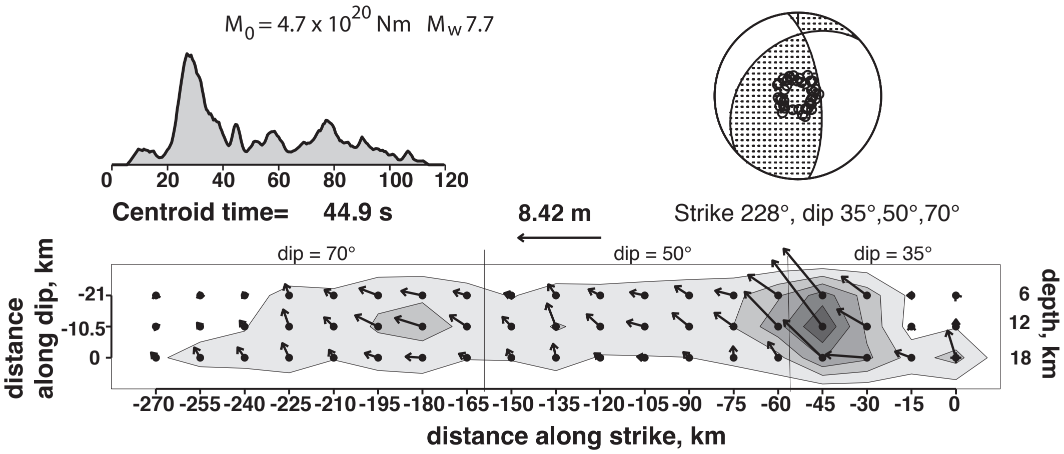

1D Green Functions

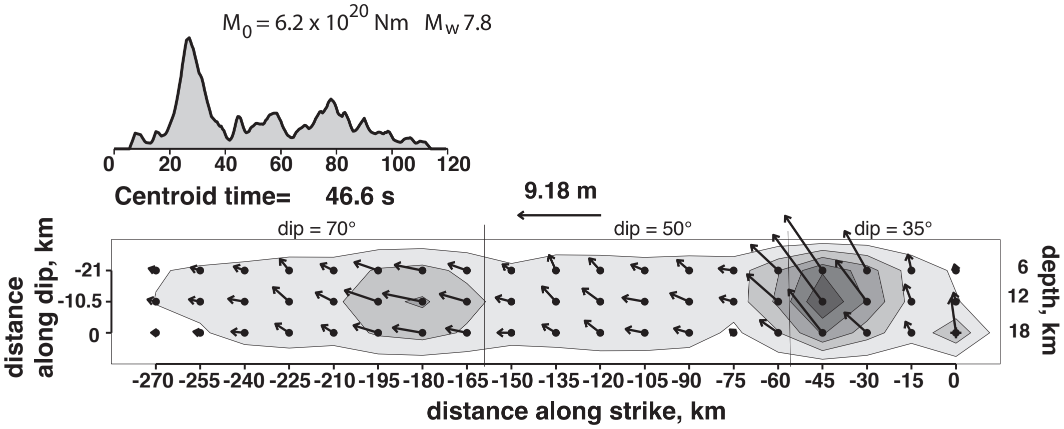

Figure 4.5 Rupture models obtained from 3D Green functions (top) and 1D Green functions (bottom).

The moment magnitude for the 3D fault model is slightly smaller than that for the 1D fault model (Mw=7.71 and Mw=7.79, respectively). The source time functions for the two models are quite similar, and the average focal mechanisms are nearly identical (strike=228, dip=35, rake=140 (3D), and rake=144 (1D)).

Figure 4.6 compares the 3D synthetic waveforms with the observed waveforms for each of the 40 stations. Figure 4.7 shows the same for the 1D waveforms. Both sets of synthetic waveforms agree well with the observations, as well as with each other, although subtle differences between the two model fits can be seen.

4.5 Discussion and Conclusions

Our rupture model inversion assumes a segmented fault, with dip across three sections varying from 35 degrees in the southwest, to 50 degrees in the center, steepening to 70 degrees at the northeast section of the fault. This assumption is in agreement with several other studies of the Wenchuan earthquake, which also present best-fit models with segmented faults (e.g., Hashimoto et al., 2010; Lin et al., 2009; Tong et al., 2010; Nakamura et al., 2010; Zhao et al., 2010; Zhang et al., 2011; Wen et al., 2012), with dips ranging from 30 to 70 degrees (Hashimoto et al., 2010; Tong et al., 2010; Nakamura et al., 2010; Wen et al., 2012).

The models produced in this study are very similar to each other, although there are sometimes significant differences between the 1DGFs and 3DGFs input into each inversion, especially for the deeper sub-sources. This makes sense since for the deeper synthetic sub-sources, the upgoing wave field senses a wider area of topography before reflecting off the surface as *pP* or *sP* phases (Figure 4.4 is a representative example of

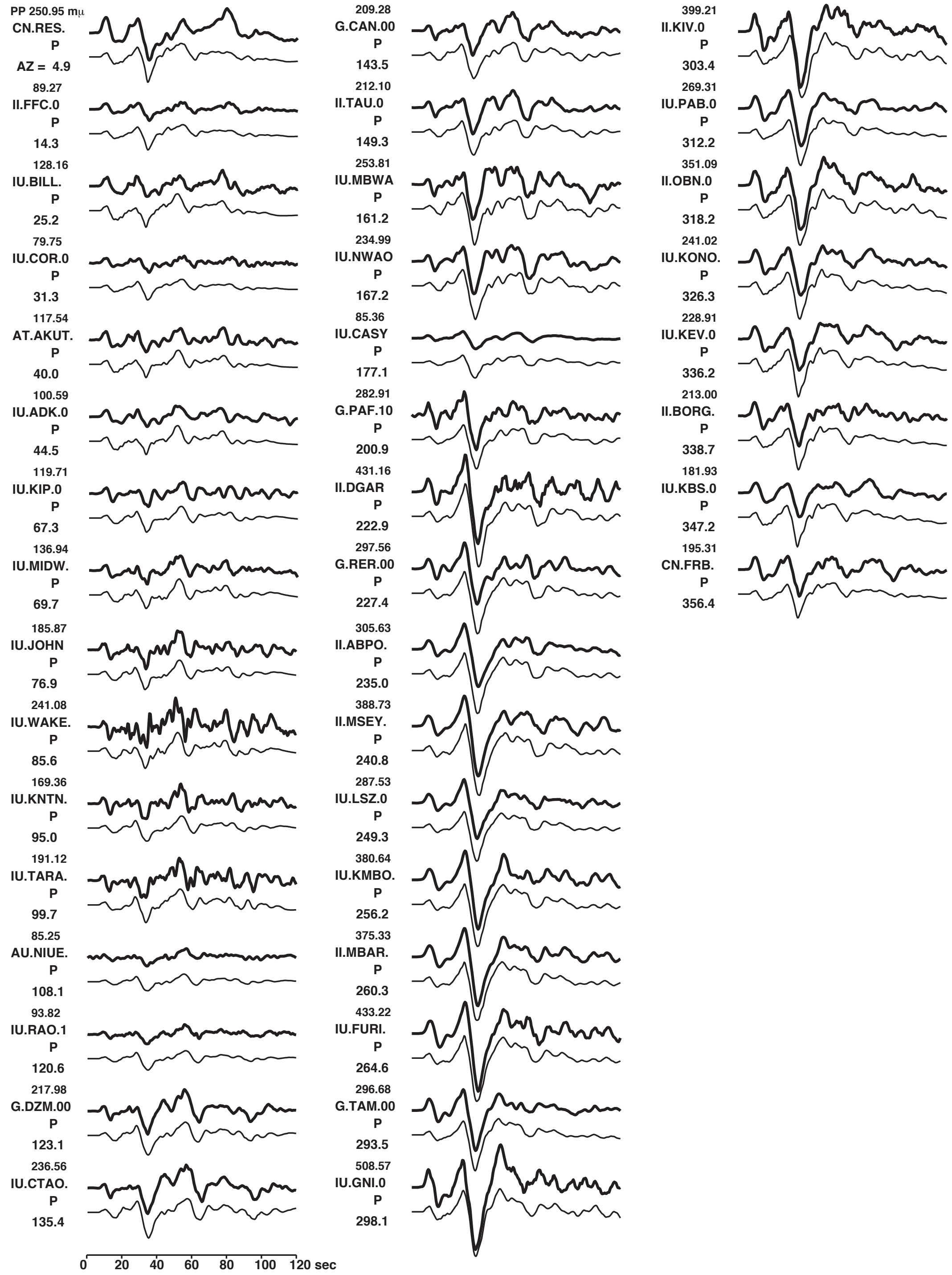

Figure 4.6 Waveforms obtained from 3DGFs (thin line) compared to observed waveforms (thick line) for each of the 40 teleseismic stations used in this study.

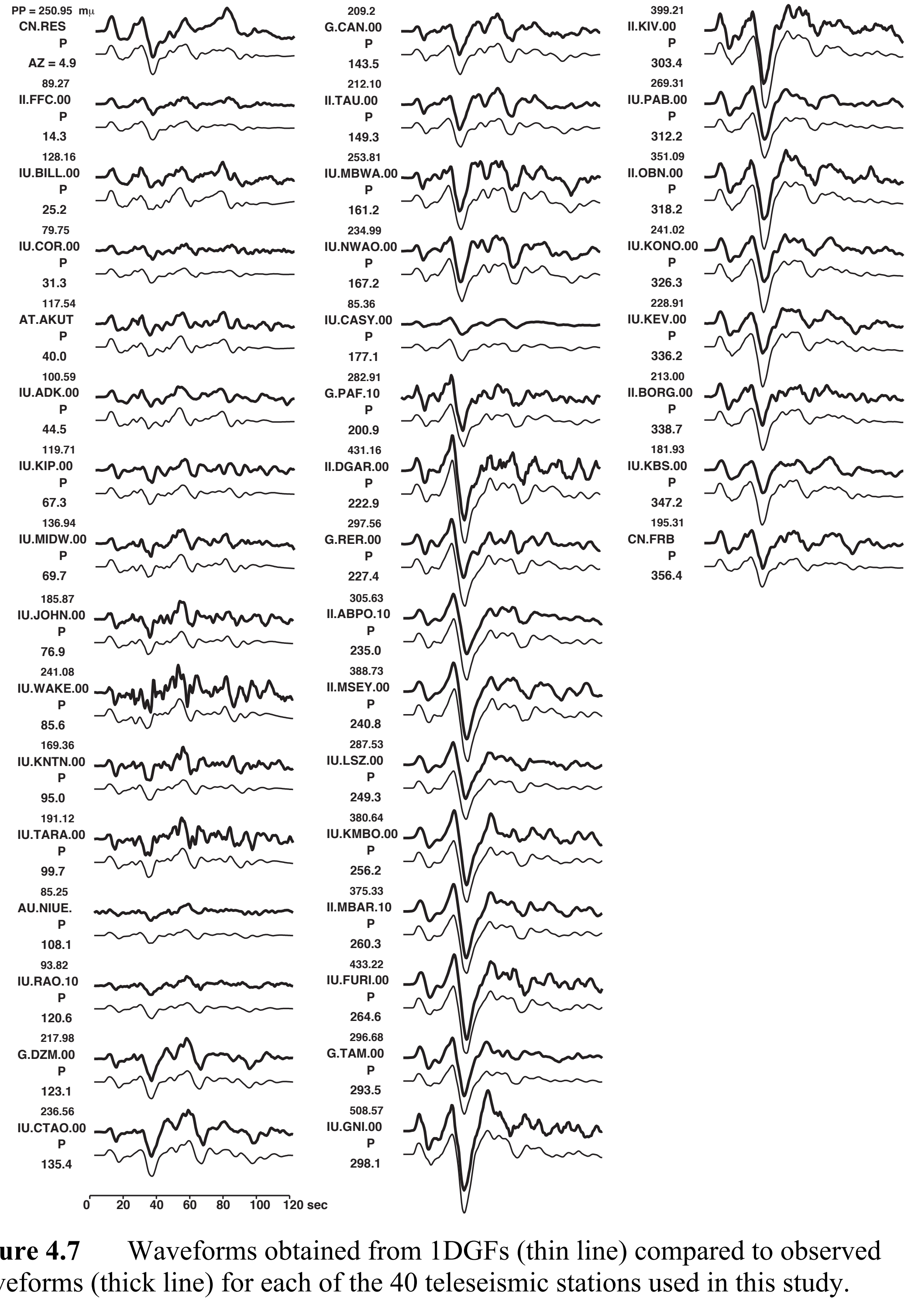

Figure 4.7 Waveforms obtained from 1DGFs (thin line) compared to observed waveforms (thick line) for each of the 40 teleseismic stations used in this study.

this). The 1D and 3D waveforms output from the inversion also show subtle differences, although both agree well with the observed waveforms (Figures 4.6 and 4.7).

Despite the differences in synthetic input and calculated waveforms, rupture models derived from 1D and 3D synthetic source regions are nearly indistinguishable from each other, but both largely agree with rupture models from other studies. Both feature a region of peak thrust slip (at about 12 km depth) approximately 45 km northeast of the epicenter, with a maximum slip of 8.42 m for the 3D model, and 9.18 m for the 1D model. There is also a secondary peak evident in both models about 180 km northeast of the epicenter. This is consistent with several models which show regions of peak slip at these approximate locations (Figure 4.8) (e.g., Ji and Hayes, 2008; Nakamura et al., 2010; Zhao et al., 2010), and at depths of 20 km or less. Zhao et al., (2010) and Zhang et al. (2011) determine maximum slips of 8.3 m and 9 m, respectively (Figure 4.8), which is similar to ours, but Nakamura et al. (2010) calculates maximum slip for their segmented fault model to be approximately 11 m. Slip modeled for the second region of peak slip is much smaller for all models examined. Rupture duration for both of our models lasted about 120 seconds, which is longer than the 105 seconds determined by Zhao et al. (2010), but shorter than the 150 seconds from Wen et al. (2012). The seismic moment produced by Nakamura et al. (2010) (Mo=1.2×10^{21} Nm; Mw=8.0) is also slightly larger than ours (3D: Mo=4.7×10^{20} Nm, Mw=7.7; 1D: Mo=6.2×10^{20} Nm, Mw=7.8), due in large part to the high slip amplitudes in their southwest fault segment (Figure 4.8).

Figure 4.8 (next page) Results of comparable fault rupture models by a) Nakamura et al., 2010, b) Zhao et al., 2010, and c) Zhang et al., 2011.

a) Nakamura et al., 2010: multiple fault model

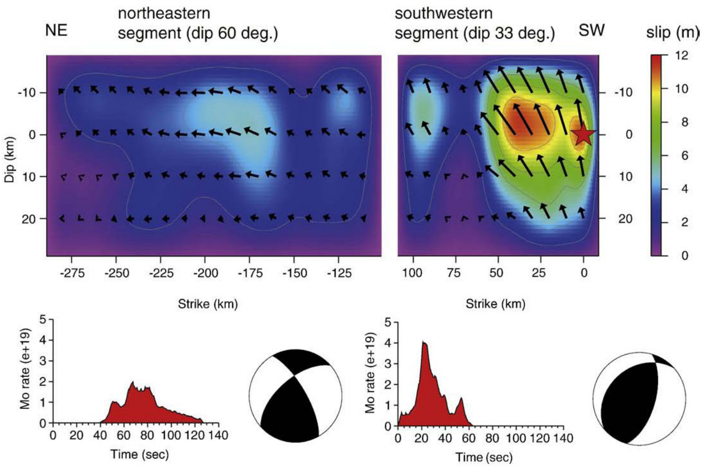

b) Zhao et al., 2010

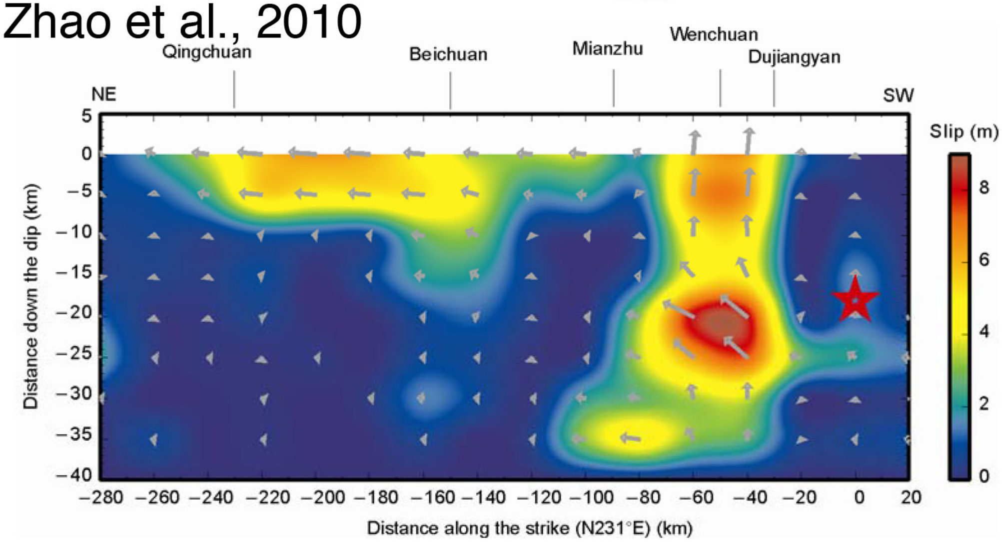

c) Zhang et al., 2011

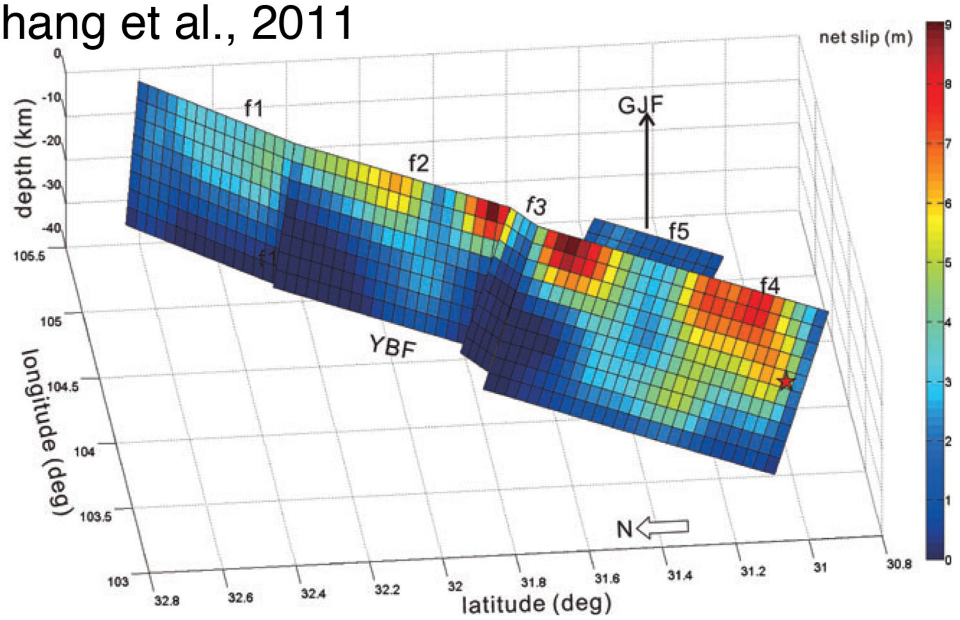

The slip mechanism for both the 3D and 1D rupture models transitions from oblique thrust near the epicenter to dextral strike-slip in the portion of the fault to the northeast with dip=70 degrees. The average focal mechanisms for both cases (3D: strike=228; dip=35, rake=140; 1D: strike=228; dip=35; rake=144) result from most of the slip occurring in the most shallowly dipping fault segment, and the average rake of the slip vectors on the rupture model reflecting nearly equal parts thrust and strike-slip. This is in contrast to the source mechanism determined by Nakamura et al. (2010) (Figure 4.8a: strike=229; dip =60; rake=159), which has steeper dip and rake reflecting more strike-slip motion due to a higher amount of the seismic moment resolved in the steeper (strike-slip) section of the 2-segment fault model than for our rupture models. This discrepancy also helps to illustrate the dependency of a rupture model on initial assumptions about fault geometry (segmentation, fault dip, length, width, etc.), and the uncertainty that can result (see different model results in Figures 4.5 and 4.8).

We attribute the similarity of the 1D and 3D rupture models, in spite of the differences observed in the Green functions, partly to our use of a half space velocity model. The lack of subsurface layering means that multiple reverberations off the complex topography do not occur, and differences between 1D and 3D Green functions, while apparent, are limited by the lack of geologic structure in our velocity model. Another reason why the Green function differences do not lead to major differences in the slip inversion is that we only produce one representative set of 3D Green functions for each of the 3 fault segments. This results in an effective 2.5D averaging of the topographic effects apparent in the 3D Green functions on the resulting rupture model. This phenomenon is also observed in the rupture model inversion produced by Okamoto and Takenaka (2009) for the 2006 Java earthquake. Finally, the similarity of our 1D and 3D rupture models is most likely due to the intrinsic nature of slip inversion, which looks for long-wavelength differences, controlled by radiation pattern, that allow model parameters to match observed data. Rapid variations in Green functions, whether incomplete, incorrect, or as in this case, due to complicated structure, are white noise for the inversion, as they do not project onto the source.

In conclusion, differences between rupture models of the 2008 Wenchuan earthquake produced from 3DGFs and 1DGFs with the same fault geometry are insignificant. Both models largely agree with those of other studies (e.g., Figure 4.8), which validates the use of 3DGFs as the basis for rupture model inversions, but there is no notable benefit gained from calculating a rupture model from 3DGFs with realistic surface topography over that produed from 1DGFs. Perhaps future rupture models can be determined from 3DGFs calculated with a velocity model which includes 3D geologic structure in and around the fault zone instead of a half space velocity model. We find that a rupture model calculated from 3DGFs is valid, but is not distinct from that calculated from 1DGFs with the same fault geometry.

4.6 References

Burchfiel, B.C., Chen, Z., Liu, Y., and Royden, L.H. (1995), Tectonics of the Longmen Shan and adjacent regions, *Int. Geology Rev.*, **37**, 661-738.

Burchfiel, B.C., Royden, L.H., van der Hilst, R.D., Hager, B.H. (2008), A geological and geophysical context for the Wenchuan earthquake of 12 May 2008, Sichuan, People's Republic of China, *GSA Today*, **18**, 4-11.

China Earthquake Networks Center, found at: http://www.csndmc.ac.cn (last accessed 2014 March 1).

Consortium for Spatial Information of the Consultative Group for International Agricultural Research (CGIAR-CSI) (2013), SRTM 90 m Digital Elevation Database v4.1, found at: http://www.srtm.csi.cgiar.org/SELECTION/inputCoord.asp (last accessed 2014 March 1).

Hao, K.X., Si, H., Fujiwara, H., Ozawa, T. (2009), Coseismic surface-ruptures and crustal deformations of the 2008 Wenchuan earthquake Mw7.9, China, *Geophys. Res. Lett.,* **36**, L11303, doi: 10.1029/2009GL037971.

Hashimoto, M., Enomoto, M., Fukushima, Y. (2009), Coseismic deformation from the 2008 Wenchuan, China, earthquake derived from ALOS/PALSAR images, *Tectonophysics*, **491**, 59-71.

Ji, C. and Hayes, G., 2008. Preliminary result of the May 12, 2008 Mw 7.9 eastern Sichuan, China earthquake, U.S. Geol. Surv., found at: http://earthquake.usgs.gov/earthquakes/eqinthenews/2008/us2008ryan/finite_fault.php (last accessed 2014 March 1).

Kikuchi, M. and Kanamori, H. (1982), Inversion of complex body waves, *Bull. Seismol. Soc. Am.,* **72**, 491-506.

Kikuchi, M., and Kanamori, H. (1991), Inversion of complex body waves – III, *Bull. Seismol. Soc. Am.*, **81**, 2335-2350.

Lin, A., Ren, Z., Jia, D., Wu, X. (2009), Co-seismic thrusting rupture and slip distribution produced by the 2008 Mw 7.9 Wenchuan earthquake, China, *Tectonophysics*, **471**, 203-215.

Nakamura, T., Tsuboi, S., Kaneda, Y., Yamanaka, Y. (2010), Rupture process of the 2008 Wenchuan, China earthquake inferred from teleseismic waveform inversion and forward modeling of broadband seismic waves, *Tectonophysics*, **491**, 72-84.

Okamoto, T. and H. Takenaka (2009), Waveform inversion for slip distribution of the 2006 Java tsunami earthquake by using 2.5D finite-difference Green's function, *Earth Planets Space*, **61**, e17-e20.

Petersson, N.A. and B. Sjögreen (2011), User's guide to WPP version 2.1.5, *Tech. Rep. LLNL-SM-487431*, Lawrence Livermore Natl. Lab. Livermore, California.

Shen, Z-K., Sun, J., Zhang, P., Wan, Y., Wang, M., Bürgmann, R., Zeng, Y., Gan, W., Liao, H., Wang, Q. (2009), Slip maxima at fault junctions and rupturing of barriers during the 2008 Wenchuan earthquake, *Nat. Geosci.*, **2**, 718-724.

Tong, X., Sandwell, D., Fialko, Y. (2010), Coseismic slip model of the 2008 Wenchuan earthquake derived from joint inversion of interferometric synthetic aperture radar, GPS, and field data, *J. Geophys. Res.*, **115**, B04314, doi: 10.1029/2009JB006625.

United States Geological Survey, National Earthquake Information Center (NEIC), Event catalog, found at: http://earthquake.usgs.gov/earthquakes/search (last accessed 2014 March 1).

Wen, Y-Y., Ma, K-F., Oglesby, D. (2012), Variations in rupture speed, slip amplitude and slip direction during the 2008 Mw 7.9 Wenchuan earthquake, *Geophys. J. Int.*, **190**, 379-390.

Xu, X., Wen, X., Yi, G., Chen, G., Klinger, Y., Hubbard, J., Shaw, J. (2010), Coseismic reverse- and oblique-slip surface faulting generated by the 2008 Mw 7.9 Wenchuan earthquake, China, *Geology*, **37**, 515-518.

Xu, Z., Song, X. (2010), Joint inversion for crustal and Pn velocities and Moho depth in eastern margin of the Tibetan Plateau, *Tectonophysics*, **491**, 185-193.

Yin, A. (2010), Preface: A special issue on the great 12 May 2008 Wenchuan earthquake (Mw7.9): Observations and unanswered questions, *Tectonophysics*, **491**, 1-9.

Zhang, H., Ge, Z. (2010), Tracking the rupture of the 2008 Wenchuan earthquake by using the relative back-projection method, *Bull. Seismol. Soc. Am.*, **100**, 2551-2560.

Zhang, Y., Feng, W., Xu, L., Zhou, C., Chen, Y. (2009), Spatio-temporal rupture process of the 2008 great Wenchuan earthquake, *Sci. China Ser. D: Earth Sci.*, **52**, 145-154.

Zhang, G., Qu, C., Shan, X., Song, X., Zhang, G., Wang, C., Hu, J-C., Wang, R. (2011), Slip distribution of the 2008 Wenchuan Ms 7.9 earthquake by joint inversion from GPS and InSAR measurements: a resolution test study, *Geophys. J. Int.*, **186**, 207-220.

Zhao, C., Chen, Z., Zhou, L., Li, Z., Kang, Y. (2010), Rupture process of the Wenchuan M8.0 earthquake of Sichuan, China: the segmentation feature, *Chi. Sci. Bull.*, **55**, 284-292.

Appendix A From Chapter 3: Synthetic PGFs for the 2006 and 2009/2013 grid regions

Red = array stacks (observed); Blue = 3D PGFs (synthetic)

2006 Locations

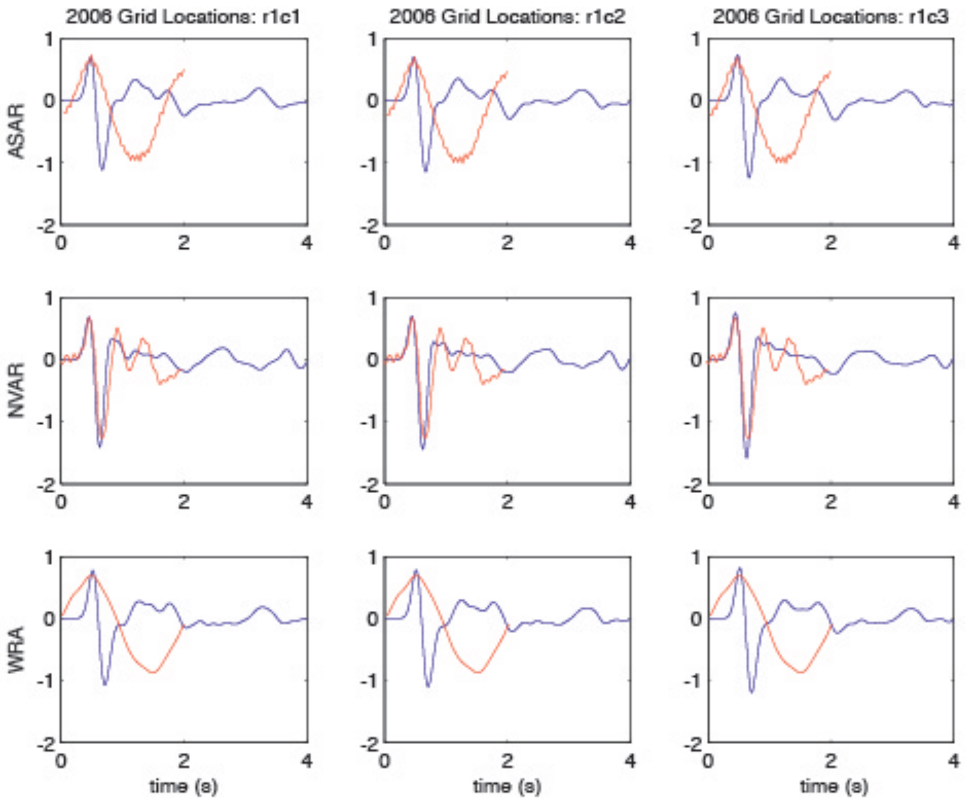

2006 Locations

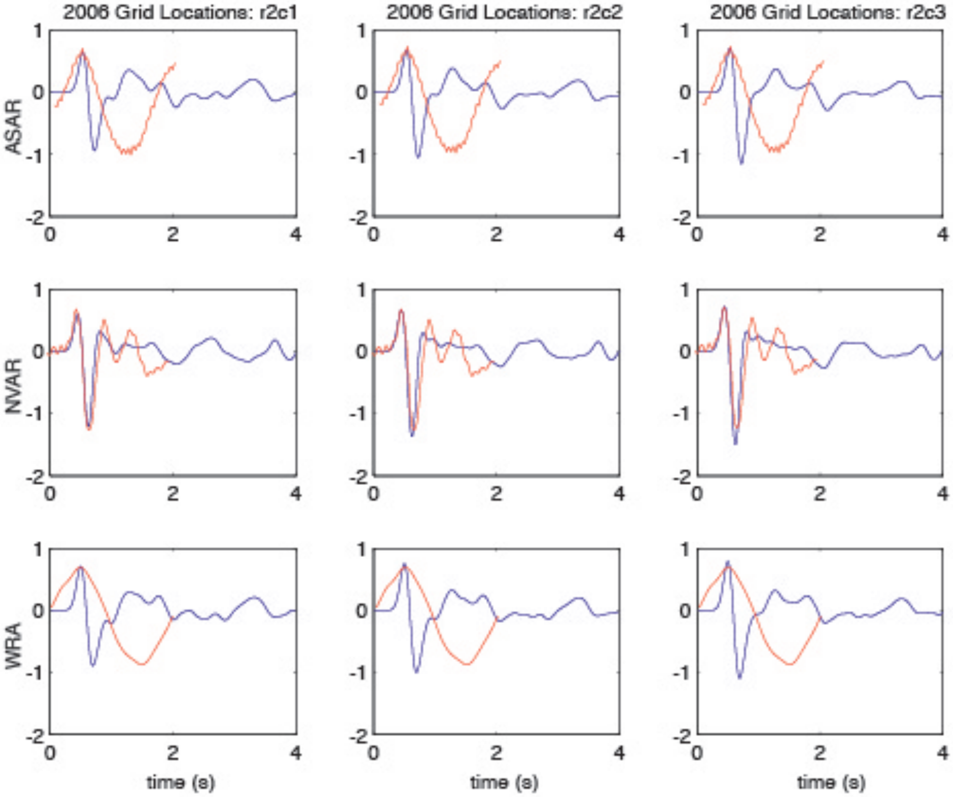

2006 Locations

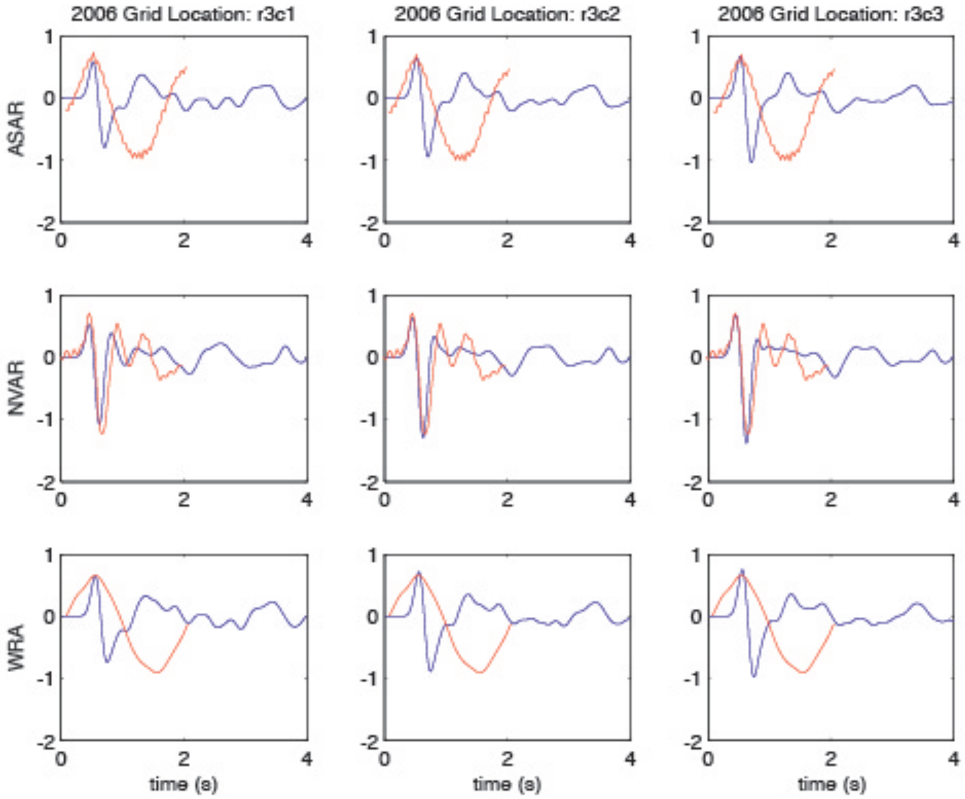

2009 Locations

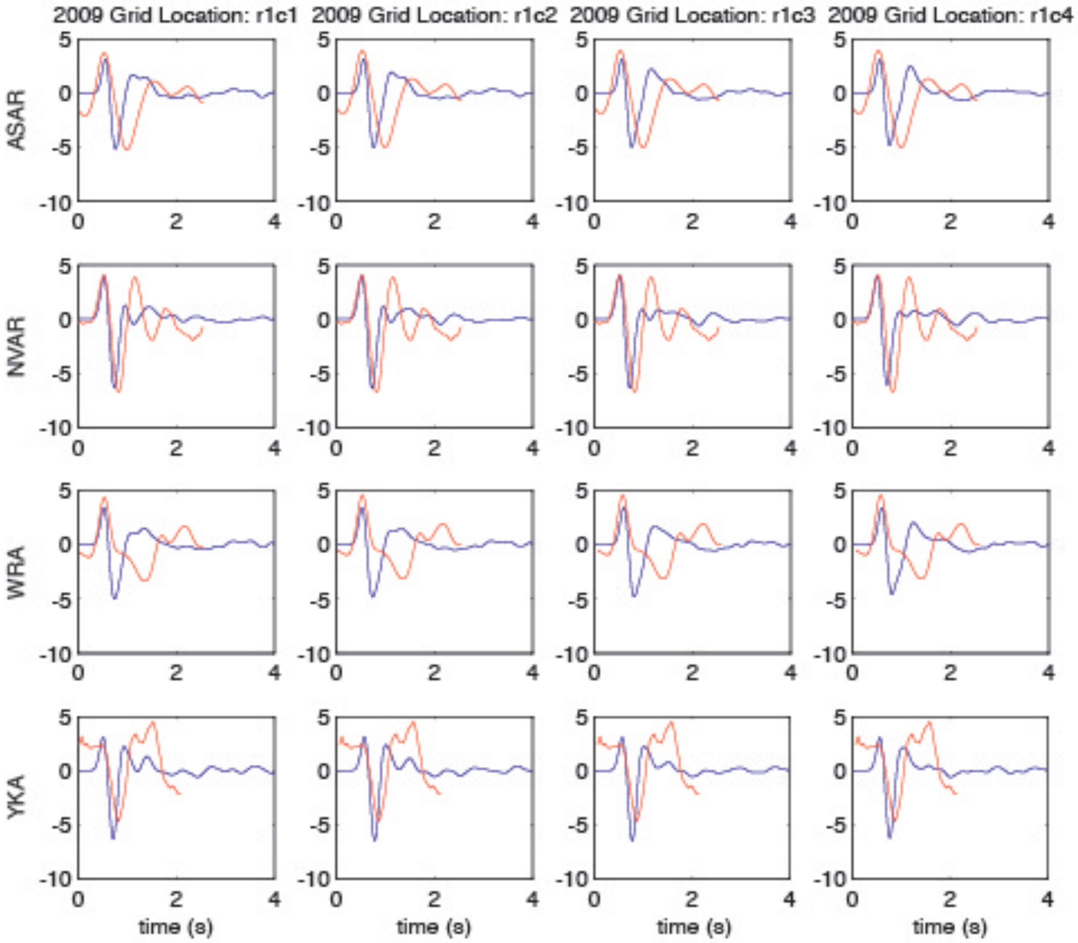

2009 Locations

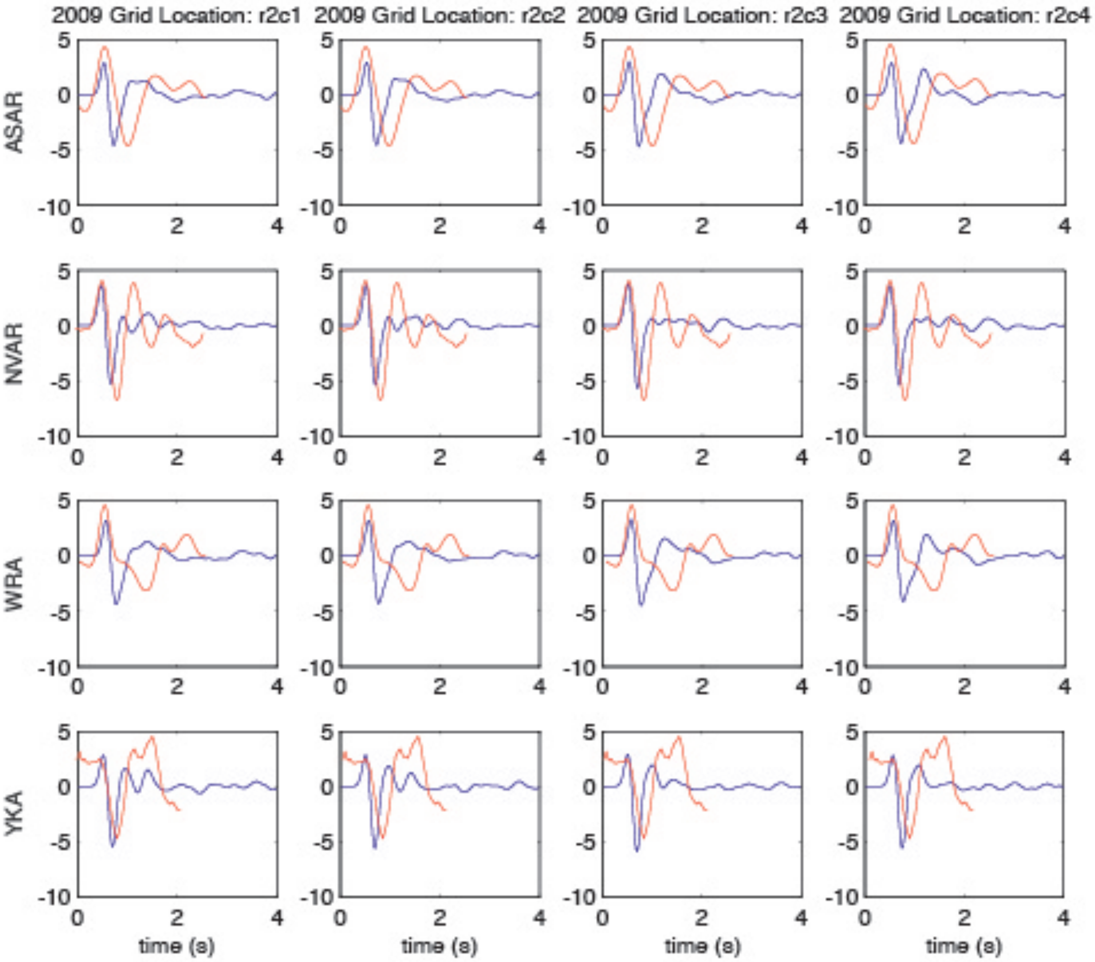

2009 Locations

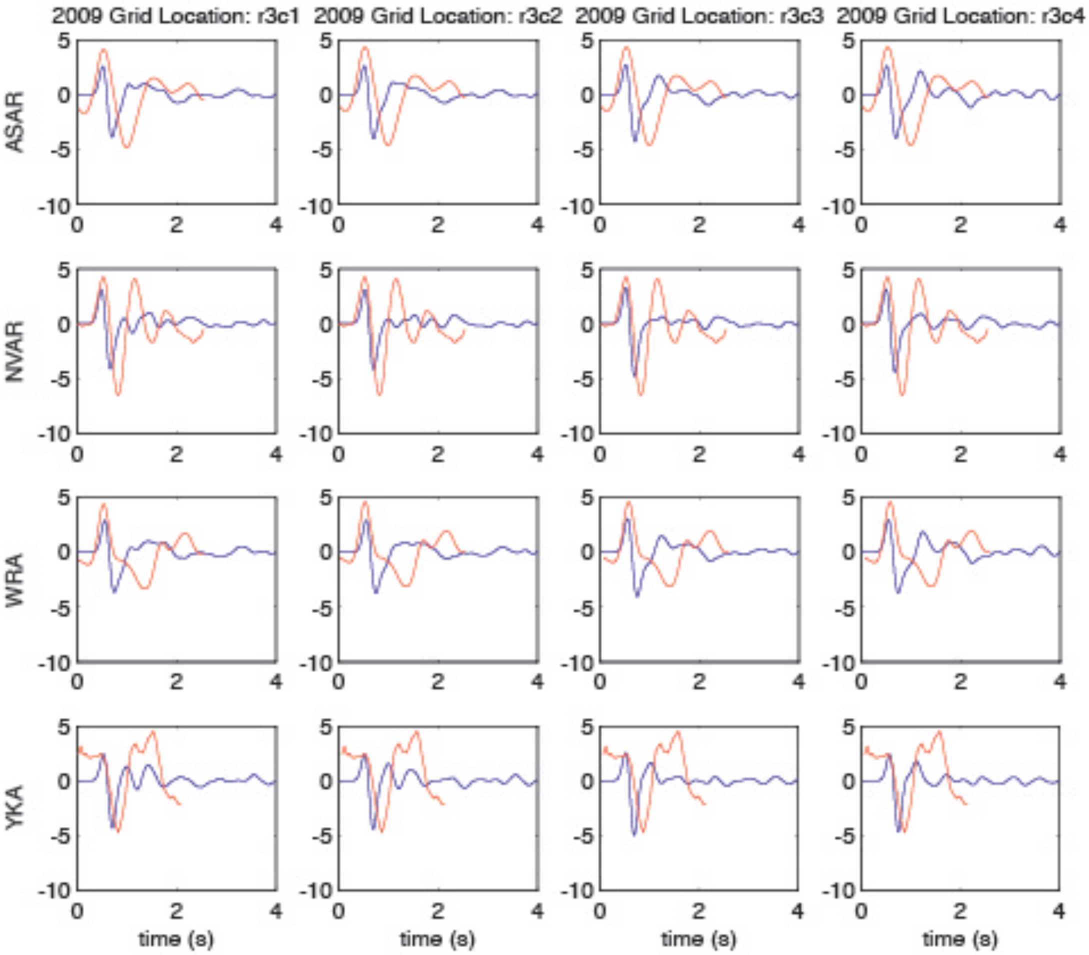

2009 Locations

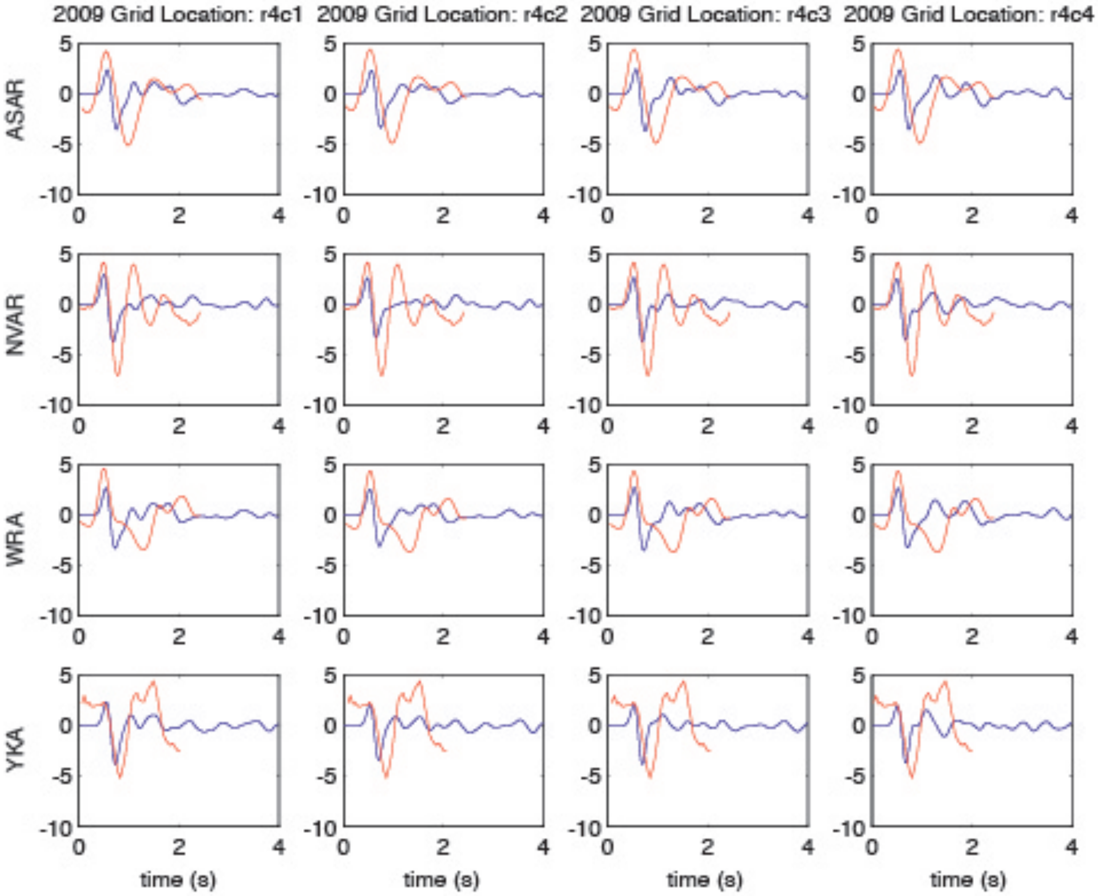

2013 Locations

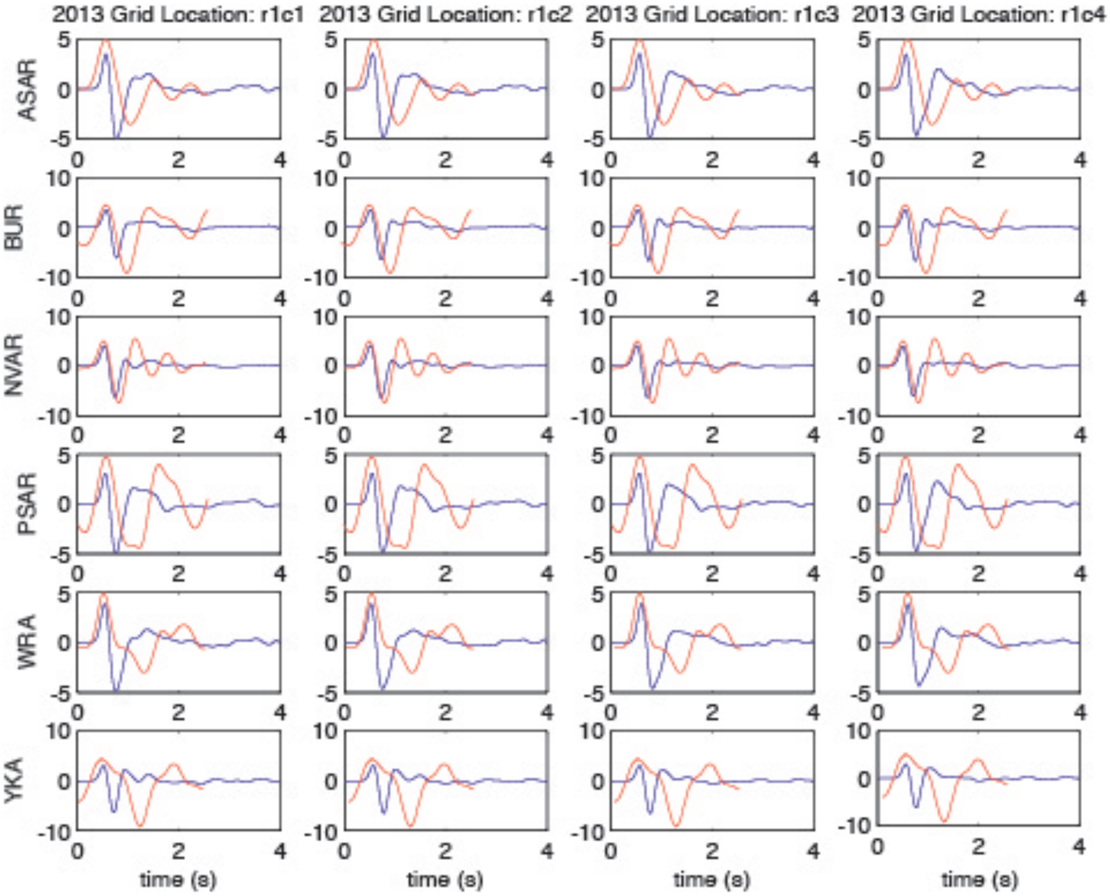

2013 Locations

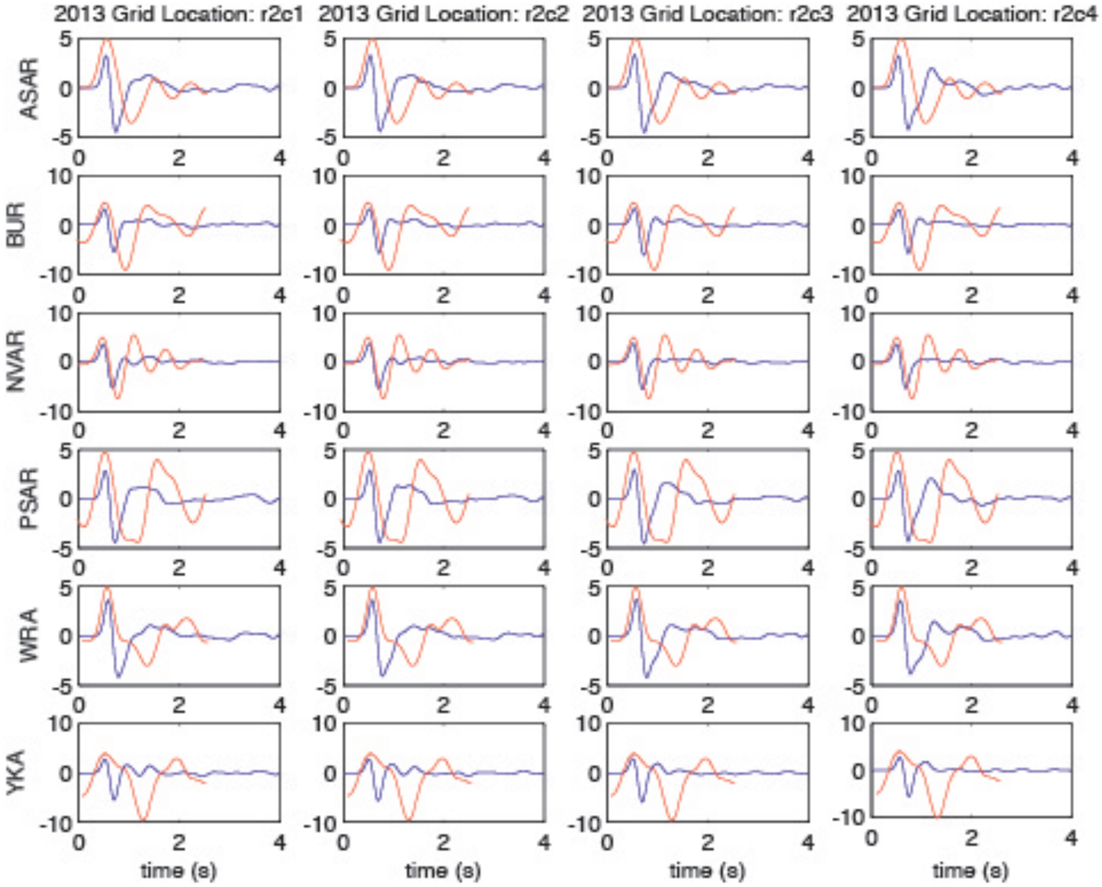

2013 Locations

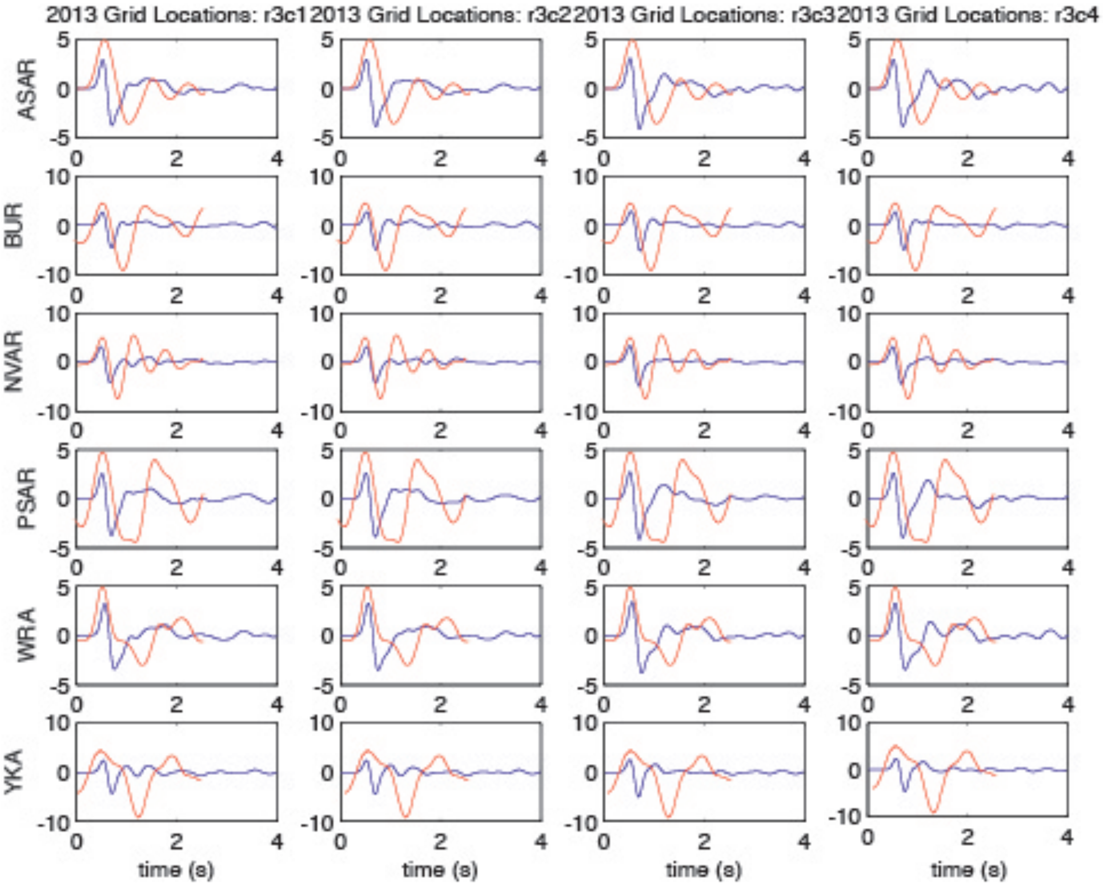

2009 & 2013 Locations

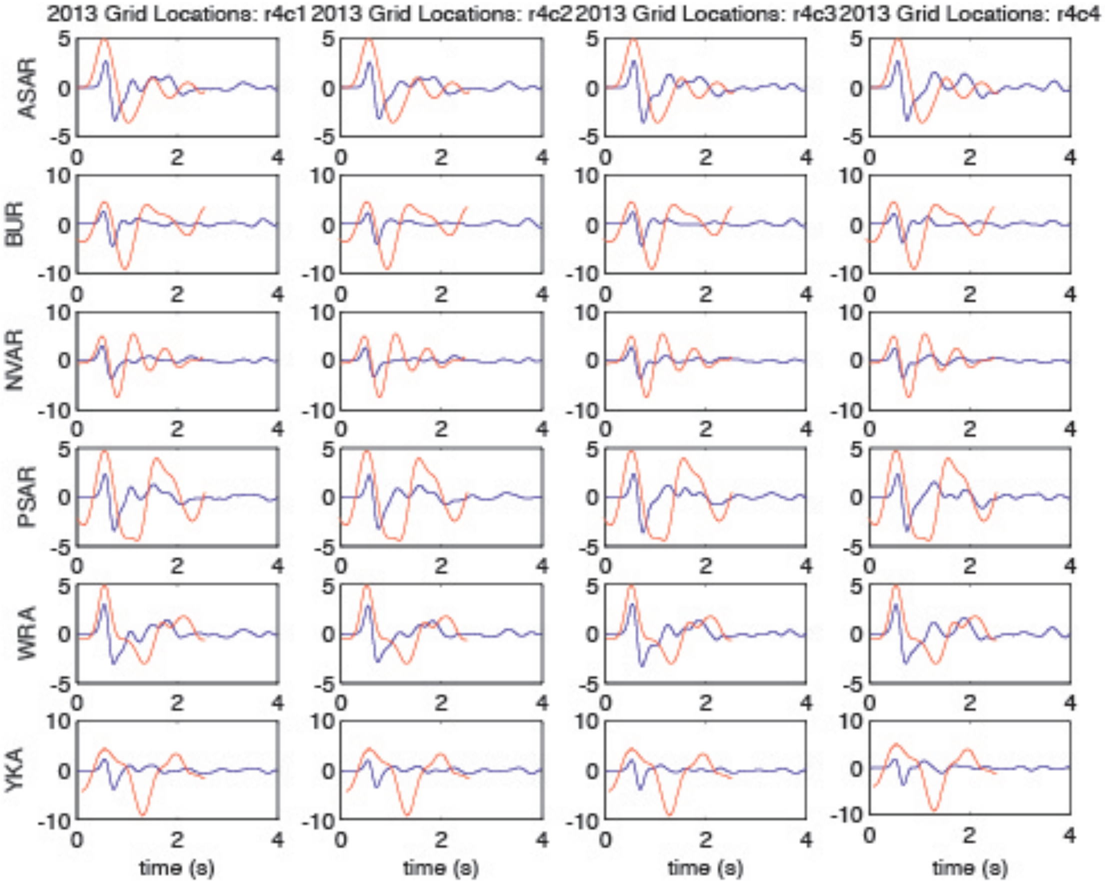

References

Aki, K. and P.G. Richards (2002), *Quantitative Seismology*, 2nd ed., Univ. Sci., Sausalito, California.

Appelo, D. and N.A. Petersson (2008), A stable finite difference method for the elastic wave equation on complex geomtries with free surfaces, *Commun. Comp. Phys.*, **5**, 84-107.

Avants, M., T. Lay, X-B. Xie, and X. Yang (2011), Effects of 2D random velocity heterogeneities in the mantle lid and Moho topography on *Pn* geometric spreading, *Bull. Seismol. Soc. Am.*, **101**, 126-140.

Bache, T.C. and D.G. Harkrider (1976), The body waves due to a general seismic source in a layered Earth model: 1. Formulation of the theory, *Bull. Seismol. Soc. Am.*, **66**, 1805-1819.

Buldyrev, V.S., and A.I. Lanin (1965). Interfering waves at the surface of an elastic inhomogeneous sphere, *Rev. Geophys.* **3,** 49-54.

Burchfiel, B.C., Chen, Z., Liu, Y., and Royden, L.H. (1995), Tectonics of the Longmen Shan and adjacent regions, *Int. Geology Rev.*, **37**, 661-738.

Burchfiel, B.C., Royden, L.H., van der Hilst, R.D., Hager, B.H. (2008), A geological and geophysical context for the Wenchuan earthquake of 12 May 2008, Sichuan, People’s Republic of China, *GSA Today*, **18**, 4-11.

Burridge, R. and L. Knopoff (1964), Body force equivalents for seismic dislocations, *Bull. Seismol. Soc. Am.*, **54**, 1875-1888.

Chapman, C.H. (1973). The Earth flattening transformation in body wave theory, *Geophys. J. R. Astr. Soc.* **35,** 55-70.

Chapman, C.H. (1974), Generalized ray theory for an inhomogeneous medium, *Geophys. J. R. Astr. Soc.*, **36**, 673-704.

Chapman, C.H. (1976), Exact and approximate generalized ray theory in vertically inhomogeneous media, *Geophys. J. R. Astr. Soc.*, **46**, 201-233.

China Earthquake Networks Center, found at: http://www.csndmc.ac.cn (last accessed 2014 March 1).

Consortium for Spatial Information of the Consultative Group for International Agricultural Research (CGIAR-CSI) (2013), SRTM 90 m Digital Elevation Database v4.1, found at:

http://www.srtm.csi.cgiar.org/SELECTION/inputCoord.asp (last accessed 2014 March 1).

Crotwell, H.P., T.J. Owens, and J. Ritsema (1999), The TauP Toolkit: Flexible seismic travel-time and ray-path utilities, *Seismol. Res. Lett.*, **70**, 154-160.

Fisk, M.D., S.R. Taylor, T. Lay, and X. Xie (2008). Analysis and modeling of regional seismic phases at nuclear test sites: Implications for *P/S* discrimination, *NNSA Report MRC/WDC-R-560*, 99 pp.

Fuchs, K. and G. Müller (1971), Computation of synthetic seismograms with the reflectivity method and comparison with observations, *Geophys. J. Int.*, **23**, 417-433.

Ge, Z., L-Y. Fu, and R-S. Wu (2005), *P-SV* Wave-field connection technique for regional wave propagation simulation, *Bull. Seismol. Soc. Am.*, **95**, 1375-1386.

Hao, K.X., Si, H., Fujiwara, H., Ozawa, T. (2009), Coseismic surface-ruptures and crustal deformations of the 2008 Wenchuan earthquake Mw7.9, China, *Geophys. Res. Lett.,* **36**, L11303, doi: 10.1029/2009GL037971.

Hartse, H.E., S.R. Taylor, W.S. Phillips, and G.E. Randall (1997). A preliminary study of regional seismic discrimination in central Asia with emphasis in western China, *Bull. Seismol. Soc. Am.* **87,** 551-568.

Hashimoto, M., Enomoto, M., Fukushima, Y. (2009), Coseismic deformation from the 2008 Wenchuan, China, earthquake derived from ALOS/PALSAR images, *Tectonophysics*, **491**, 59-71.

He, Y., X-B. Xie, and T. Lay (2008), Explosion-source energy partitioning and *Lg*-wave excitation: contributions of free-surface scattering, *Bull. Seismol. Soc. Am.*, **98**, 778-792.

Helmberger, D.V. (1968), The crust-mantle transition in the Bering Sea, *Bull. Seismol. Soc. Am.*, **58**, 179-214.

Hill, D.P. (1973). Critically refracted waves in a spherically symmetric radially heterogeneous Earth model, *Geophys. J. R. Astr. Soc.* **34,** 149-177.

Ji, C. and Hayes, G., 2008. Preliminary result of the May 12, 2008 Mw 7.9 eastern Sichuan, China earthquake, U.S. Geol. Surv., found at: http://earthquake.usgs.gov/earthquakes/eqinthenews/2008/us2008ryan/finite_fault.php (last accessed 2014 March 1).

Kasahara, K. (1981), *Earthquake Mechanics*, Cambridge University Press, New York, New York.

Kikuchi, M. and Kanamori, H. (1982), Inversion of complex body waves, *Bull. Seismol. Soc. Am.,* **72**, 491-506.

Kikuchi, M., and Kanamori, H. (1991), Inversion of complex body waves – III, *Bull. Seismol. Soc. Am.*, **81**, 2335-2350.

Kikuchi, M. and H. Kanamori (2003), Note on teleseismic body-wave inversion program, *Earthquake Research Institute, Tokyo University, Japan*, Online at http://www.eri.u-tokyo.ac.jp/ETAL/KIKUCHI

Lay, T. and T.C. Wallace (2005), *Modern Global Seismology*, Academic Press, San Diego, California.

Lin, A., Ren, Z., Jia, D., Wu, X. (2009), Co-seismic thrusting rupture and slip distribution produced by the 2008 Mw 7.9 Wenchuan earthquake, China, *Tectonophysics*, **471**, 203-215.

McLaughlin, K.L., T.G. Barker, S.M. Day, B. Shkoller, and J.L. Stevens (1992), Effects of subduction zone structure on explosion-generated Rayleigh waves: 3-D numerical simulations, *Geophys. J. Int.*, **111**, 291-308.

Menke, W.H., and P.G. Richards (1980). Crust-mantle whispering gallery phases: A deterministic model of teleseismic P_n wave propagation, *J. Geophys. Res.* **85,** 5416-5422.

Miksat, J. T.M. Müller, and F. Wenzel (2008), Simulating three-dimensional seismograms in 2.5-dimensional structures by combining two-dimensional finite difference modelling and ray tracing, *Geophys. J. Int.*, **174**, 309-315.

Morozov, I. (2010). On the causes of frequency-dependent apparent seismological Q, *Pure Appl. Geophys.* **167,** 1131-1146, doi 10.1007/s00024-010-0100-6.

Morozova, E.A., I.B. Morozov, and S.B. Smithson (1999). Heterogeneity of the uppermost mantle beneath Russian Eurasia from the ultra-long-range profile QUARTZ, *J. Geophys. Res.* **104,** 20,329-20,348.

Müller, G. (1977). Earth-flattening approximation for body waves derived from geometric ray theory - Improvements, corrections and range of applicability, *J. Geophys.* **42,** 429-436.

Murphy, J.R., B.C. Kohl, J.L. Stevens, T.J. Bennett, and H.G. Israelsson (2010), Exploitation of the IMS and other data for a comprehensive, advanced analysis of the North Korean nuclear tests, paper presented at the 2010 Monitoring Research Review: Ground-Based Nuclear Explosion Monitoring Technologies, Natl. Nucl. Security Admin., Washington, D.C.

Murphy, J.R., J.L. Stevens, B.C. Kohl, T.J. Bennett, and B.W. Barker (2011), Supplemental analysis of the seismic characteristics of the 2006 and 2009 North Korean nuclear tests, paper presented at the 2011 Monitoring Research Review: Ground-Based Nuclear Explosion Monitoring Technologies, Natl. Nucl. Security Admin., Washington, D.C.

Myers, S.C., M.L. Begnaud, S. Ballard, M.E. Pasyanos, W.S. Phillips, A.L. Ramirez, M.S. Antolik, K.D. Hutchenson, J.J. Dwyer, C.A. Rowe, and G.S. Wagner (2010). A crust and upper-mantle model of Eurasia and North Africa for P_n travel-time calculation, *Bull. Seismol. Soc. Am.* **100,** 640-656, doi 10.1785/0120090198.

Nakamura, T., Tsuboi, S., Kaneda, Y., Yamanaka, Y. (2010), Rupture process of the 2008 Wenchuan, China earthquake inferred from teleseismic waveform inversion and forward modeling of broadband seismic waves, *Tectonophysics*, **491**, 72-84.

Nilsson, S., N.A. Petersson, B. Sjögreen, and H-O. Kreiss (2007), Stable difference approximations for the elastic wave equation in second order formultion, *SIAM J. Numer. Anal.*, **45**, 1902-1936.

Okamoto, T. (1993), Effects of sedimentary structure and bathymetry near the source on teleseismic *P* waveforms from shallow subduction zone earthquakes, *Geophys. J. Int.*, **112**, 471-480.

Okamoto, T. (1994), Teleseismic synthetics obtained from 3-D calculations in 2-D media, *Geophys. J. Int.*, **118**, 613-622.

Okamoto, T. and H. Takenaka (2009), Waveform inversion for slip distribution of the 2006 Java tsunami earthquake by using 2.5D finite-difference Green's function, *Earth Planets Space*, **61**, e17-e20.

Pasyanos, M.E., W.R. Walter, and E.M. Matzel (2009). A simultaneous multiphase approach to determine *P*-wave and *S*-wave attenuation of the crust and upper mantle, *Bull. Seismol. Soc. Am.* **99,** 3314-3325, doi 10.1785/0120090061.

Petersson, N.A. and B. Sjögreen (2011), User's guide to WPP version 2.1.5, *Tech. Rep. LLNL-SM-487431*, Lawrence Livermore Natl. Lab. Livermore, California.

Pitarka, A., D.V. Helmberger, and S. Ni (2007), Analysis and simulation of three-dimensional scattering due to heterogeneous crustal structure and surface topography on regional phases; magnitude and discrimination, *Proceedings of the 29th Seismic Research Review: Ground-Based Nuclear Explosion Monitoring Technologies*, FA8718-07-C-0003, Vol. 1, 205-213.

Randall, E.G. (1994). Efficient calculations of complete differential seismograms for laterally homogeneous Earth models, *Geophys. J. Int.* **118,** 245-254.

Regan, J. and D.G. Harkrider (1989), Seismic representation theorem coupling: synthetic SH mode sum seismograms for non-homogeneous paths, *Geophys. J. Int.*, **98**, 429-446.

Regan, J. and D.G. Harkrider (1991), Seismic representation theorem coupling: P-SV mode sum seismograms for non-homogeneous paths, *Geophys. J. Int.*, **106**, 587-609.

Rodgers, A.J., N.A. Petersson, and B. Sjögreen (2010), Simulation of topographic effects on seismic waves from shallow explosions near the North Korean nuclear test site with emphasis on shear wave generation, *J. Geophys. Res.*, **115**, B11309, doi:10.1029/2010JB007707.

Sereno, T.J., and J.W. Given (1990). P_n attenuation for a spherically symmetric Earth model, *Geophys. Res. Lett.* **17,** 1141-1144.

Sereno, T.J., S.R. Bratt, and T.C. Bache (1988). Simultaneous inversion of regional wave spetra for attenuation and seismic moment in Scandinavia, *J. Geophys. Res.* **93,** 2019-2036.

Shen, Z-K., Sun, J., Zhang, P., Wan, Y., Wang, M., Bürgmann, R., Zeng, Y., Gan, W., Liao, H., Wang, Q. (2009), Slip maxima at fault junctions and rupturing of barriers during the 2008 Wenchuan earthquake, *Nat. Geosci.*, **2**, 718-724.

Shi, Z. and Y. Ben-Zion (2009), Seismic radiation from tensile and hear point dislocations between similar and dissimilar solids, *Geophys. J. Int.*, **179**, 444-458.

Stead, R.J. and D.V. Helmberger (1988), Numerical-analytical interfaceing in two-dimensions with applications to modeling NTS seismograms, *PAGEOPH*, **128**, 157-193.

Stevens, J.L. and H. Xu (2010), Wave propagation from complex 3D sources using the representation theorem, *2010 Monitoring Research Review: Ground-Based Nuclear Explosion Monitoring Technologies*, FA8718-08-C-0010, Vol. 1, 519-528.

Sun, W. L-Y. Fu, and R-S. Wu (2008), 2.5D *SH* wave propagation in heterogeneous crustal waveguides using the phase screen method, *Bull. Seismol. Soc. Am.*, **98**, 2391-2401.

Takenaka, H. and B.L.N. Kennett (1996), A 2.5-D time-domain elastodynamic equation for plane-wave incidence, *Geophys. J. Int.*, **125**, F5-F9.

Takenaka, H., B.L.N. Kennett, and H. Fujiwara (1996), Effect of 2-D topography on the 3-D seismic wavefield using a 2.5-D discrete wavenumber-boundary integral equation method, *Geophys. J. Int.*, **124**, 741-755.

Taylor, S.R. A.A. Velasco, H.E. Hartse, W.S. Phillips, W.R. Walter, and A.J. Rodgers (2002). Amplitude corrections for regional seismic discriminants, *Pure Appl. Geophys.* **159,** 623-650.

Taylor, S.R., and F.N. App (2010), Representation theorem coupling of numerical and wave propagation codes for the generation of synthetic seismograms, *Los Alamos National Laboratory, NM*, LAUR-94-2194.

Tong, X., Sandwell, D., Fialko, Y. (2010), Coseismic slip model of the 2008 Wenchuan earthquake derived from joint inversion of interferometric synthetic aperture radar, GPS, and field data, *J. Geophys. Res.*, **115**, B04314, doi: 10.1029/2009JB006625.

United States Geological Survey, National Earthquake Information Center (NEIC), Event catalog, found at: http://earthquake.usgs.gov/earthquakes/search (last accessed 2014 March 1).

Vasconcelos, I., R. Snieder, and H. Douma (2009), Representation theorems and Green's function retrieval for scattering in acoustic media, *Phys. Rev. E*, **80**, 036605.

Walter, W.R., and S.R. Taylor (2001). A revised magnitude and distance amplitude correction (MDAC2) procedure for regional seismic discriminants: Theory and testing at NTS, *Lawrence Livermore National Laboratory Report UCRL-ID-146882*, 13 pp.

Walter, W.R., K.M. Mayeda, and H. Patton (1995). Phase and spectral ratio discrimination between NTS earthquakes and explosions, Part I: Empirical observations, *Bull. Seismol. Soc. Am.* **85,** 1050-1067.

Wen, L. and D.V. Helmberger (1998), A two-dimensional *P-SV* hybrid method and its application to modeling localized structures near the core-mantle boundary, *J. Geophys. Res.*, **103**, 17901-17918.

Wen, L. and H. Long (2010), High-precision location of North Korea's 2009 nuclear test, *Seismol. Res. Lett.*, **81**, 26-29.

Wen, Y-Y., Ma, K-F., Oglesby, D. (2012), Variations in rupture speed, slip amplitude and slip direction during the 2008 Mw 7.9 Wenchuan earthquake, *Geophys. J. Int.*, **190**, 379-390.

Wu, R-S., S. Jin, and X-B. Xie (2000), Seismic wave propagation and scattering in heterogeneous crustal waveguides using screen propagators: I SH waves, *Bull. Seismol. Soc. Am.*, **90**, 401-413.

Xie, X., and T. Lay (1994). The excitation of L_g waves by explosions: A finite-difference investigation, *Bull. Seismol. Soc. Am.* **84,** 324-342.

Xu, X., Wen, X., Yi, G., Chen, G., Klinger, Y., Hubbard, J., Shaw, J. (2010), Coseismic reverse- and oblique-slip surface faulting generated by the 2008 Mw 7.9 Wenchuan earthquake, China, *Geology*, **37**, 515-518.

Xu, Z., Song, X. (2010), Joint inversion for crustal and Pn velocities and Moho depth in eastern margin of the Tibetan Plateau, *Tectonophysics*, **491**, 185-193.

Yang, X. (2002). A numerical investigation of L_g geometric spreading, *Bull. Seismol. Soc. Am.* **92,** 3067-3079.

Yang, X., T. Lay, X. Xie, M.S. Thorne (2007). Geometric spreading of P_n and S_n in a spherical Earth model, *Bull. Seismol. Soc. Am.* **97,** 2053-2065.

Yin, A. (2010), Preface: A special issue on the great 12 May 2008 Wenchuan earthquake (Mw7.9): Observations and unanswered questions, *Tectonophysics*, **491**, 1-9.

Zhang, Y., Feng, W., Xu, L., Zhou, C., Chen, Y. (2009), Spatio-temporal rupture process of the 2008 great Wenchuan earthquake, *Sci. China Ser. D: Earth Sci.*, **52**, 145-154.

Zhang, H., Ge, Z. (2010), Tracking the rupture of the 2008 Wenchuan earthquake by using the relative back-projection method, *Bull. Seismol. Soc. Am.*, **100**, 2551-2560.

Zhang, G., Qu, C., Shan, X., Song, X., Zhang, G., Wang, C., Hu, J-C., Wang, R. (2011), Slip distribution of the 2008 Wenchuan Ms 7.9 earthquake by joint inversion from GPS and InSAR measurements: a resolution test study, *Geophys. J. Int.*, **186**, 207-220.

Zhang, M. and L. Wen (2013), High-precision location and yield of North Korea's 2013 nuclear test, *Geophys. Res. Lett.*, **40**, 2941-2946.

Zhao, L.S., and J. Xie (1993). Lateral variations in compressional velocities beneath the Tibetan Plateau fom P_n travel time tomography, *Geophys. J. Int.* **115,** 1070-1084.

Zhao, C., Chen, Z., Zhou, L., Li, Z., Kang, Y. (2010), Rupture process of the Wenchuan M8.0 earthquake of Sichuan, China: the segmentation feature, *Chi. Sci. Bull.*, **55**, 284-292.